Investigation of High-Efficiency Radial and Tapered Brushless PM Machines

Solmaz Kahourzade

Thesis submitted for the degree of

Doctor of Philosophy

in

School of Electrical and Electronic Engineering

University of Adelaide, Australia

September 2017

To my husband Amin

Table of Contents

Abstract

In recent decades, factors such as the rising price of energy and the introduction of new electric machine efficiency standards have been the driving force for extensive research towards higher efficiency machines. To achieve this, both new materials and design modifications should be considered. Brushless permanent magnet (PM) machines are an excellent substitute to replace conventional machines in many applications as they offer higher efficiency, reliability and power density. Therefore, this thesis addresses the design challenges in two separate brushless PM machines (radial and tapered types) and investigates these challenges to achieve higher efficiency.

In the first part of the thesis, a 16-kW, 3-phase, 4-pole radial-flux spoke-type interior PM (IPM) machine with inherent voltage regulation capability has been presented. The machine topology was studied using analytical modelling, finite-element simulation and practical measurements. The measured parameters and performance of the machine were in close agreement with the calculated values. Since the target application was a portable AC generator, the results have been compared with the commonly used wound-field generator. It was found that this new radial IPM generator can offer 6% higher efficiency and 8.6% fuel saving. In addition, the generator presented low total harmonic distortion (THD) and good voltage regulation meeting the unity power-factor application requirements.

Furthermore, as it is a common practice for 3-phase generators to run under single-phase loading, the single-phase performance of the machine was also studied. Three winding configurations were investigated including 1-phase star, 1-phase delta and a proposed new connection named “open delta”. It was concluded that the proposed open-delta connection can operate under single-phase loading effectively. Finally, the machine performance was also studied in motoring when driven by an inverter in open-loop in volts-per-Hertz control mode, which showed a high power-factor over a wide loading range.

In the second part of the thesis, the primary goal was to study a new tapered brushless PM machine topology which used amorphous magnetic material (AMM) in the stator. A preliminary work was also presented in this part to compare the AMM material with the conventional lamination material (SiFe) and the soft magnetic

composite (SMC) material using identical stator sizes in a flat axial field machine topology. Next a tapered PM machine was studied due to its manufacturing advantages, it had the following specifications: 2-kW, 12-slot, 10-pole, 7000 rpm. A detailed and accurate loss study was conducted using 3D simulations (due to the unique shape of the machine) and practical tests to identify the major loss components for further efficiency improvements. An improved mechanical loss separation technique has been proposed and demonstrated using the open-circuit test results. In addition, a novel locked rotor test was introduced as a reliable method to separate the stator and rotor losses which is applicable to other electrical machines. After the loss separation study, a design optimisation was performed which considered three design elements: air-gap length, PM shape, and rotor yoke design. Then, a new rotor design was constructed considered the optimization of the yoke only which resulted in a substantial 3.5% improvement in efficiency.

Statement of Originality

I declare that the intellectual content of this thesis is the product of my own work. It contains no material which has been submitted for any other degree or diploma in any university or institution. To the best of my knowledge, all the assistance received in preparing this thesis and sources had been acknowledged and it contains no material previously published or written by another person, except where the reference has been made in the text.

I give consent to this copy of my thesis, when deposited in the University Library, being made available for loan and photocopying, subject to the provisions of the Copyright Act 1968.

I also give permission for the digital version of my thesis to be made available on the web, via the University's digital research repository, the Library catalogue, the Australasian Digital Theses Program (ADTP) and also through web search engines, unless permission has been granted by the University to restrict access for a period of time.

Signed: Solmaz Kahourzade

Date: 29/09/2017

Acknowledgments

I would like to express my greatest appreciation and thank my supervisors Associate Professor Wen L. Soong and Associate Professor Nesimi Ertugrul. Without their support, guidance and encouragement this research would not have been possible.

In addition, I would like to thank Glassy Metal Technologies Ltd. and the workshop staff of the School of Electrical and Electronic Engineering of The University of Adelaide for their support, in particular Ian Linke and Stephen Kloeden for their help in prototyping and testing of the AMM machines.

I also would like to acknowledge the support provided by Radial Flux Laboratories Pty. Ltd in providing the opportunity to use their machines and laboratory. I specially thank Paul Lillington for performing the tests and his help in the practical measurements during my visit to Sydney.

Publications

Published:

1. S. Kahourzade, N. Ertugrul, and W. L. Soong, "Loss Analysis and Efficiency Improvement of an Axial-Flux PM Amorphous Magnetic Material Machine", Early Access in IEEE Transaction on Industrial Electronics.

2. S. Kahourzade, W. L. Soong, and P. Lillington, "Single-Phase Loading Behavior of the Isolated 3ph Spoke Interior Permanent-Magnet Generator", IEEE Transactions on Industry Applications, Vol. 53, No. 3, May/June 2017.

3. W. L. Soong, S. Kahourzade, C.-Z. Liaw, and P. Lillington "Interior PM Generator for Portable AC Generator Sets", IEEE Transactions on Industry Applications, Vol. 52, No. 2, March/April 2016.

4. N. Ertugrul, R. Hasegawa, W. L. Soong, J. Gayler, S. Kloeden, and S. Kahourzade, "A Novel Tapered Rotating Electrical Machine Topology Utilizing Cut Amorphous Magnetic Material", IEEE Transaction on Magnetics, Vol. 51, No. 7, July 2015.

5. S. Kahourzade, N. Ertugrul, and W. L. Soong, "Investigation of Emerging Magnetic Materials for Application in Axial-Flux PM Machines", IEEE Energy Conversion Congress and Exposition (ECCE), Milwaukee, USA, September 2016.

6. S. Kahourzade, W. L. Soong, and P. Lillington, "Performance of Cage-Less Interior PM Motor with Open-Loop Inverter Drive", IEEE Energy Conversion Congress and Exposition (ECCE), Montreal, Canada, September 2015.

7. S. Kahourzade, W. L. Soong, and P. Lillington, "Unbalanced Loading Behavior of the Isolated Interior Permanent-Magnet Generator", IEEE Energy Conversion Congress and Exposition (ECCE), Montreal, Canada, September 2015.

8. W. L. Soong, S. Kahourzade, and C.-Z. Liaw, "Interior PM Generator for Portable AC Generator Sets", IEEE Energy Conversion Congress and Exposition (ECCE), Pittsburg, PA, USA, 14^{th} -18^{th} September 2014.

Under Review:

S. Kahourzade, N. Ertugrul, and W. L. Soong, "Investigation of Emerging Magnetic Materials for Application in Axial-Flux PM Machines", Submitted to IEEE Transactions on Industry Applications.

Nomenclature

θ	rotor angle	degree
μ_0	the permeability of air	N/A^2
μ	friction coefficient	
λ_{end}	end winding permeance factor	
σ	electrical conductivity	S/m
ω	angular velocity	
ξ	saliency	
ρ_{air}	air density at one atmosphere and 20°C	kg/m^3
η_{air}	dynamic viscosity of air at one atmosphere and 20°C	Pa.s
c_f	coefficient of drag	
C_M	torque coefficient	
D_r	rotor diameter	m
$D_{bearing}$	inner diameter of the bearing	m
E	back-emf voltages	V
f	frequency	Hz
F	bearing load	
k	air gap roughness coefficient	
I_d	*d*-axis current	A
I_q	*q*-axis current	A
l_{end}	average length of the end winding	m
L	self-inductance	H
l_r	rotor axial length	m
L_{end}	end-winding leakage inductance	H
L_0	dc components of self-inductance	H
L_1	fundamental harmonic of self-inductance	H
m	number of phases	
M	mutual inductance	H
M_0	dc components of mutual inductance	H
M_1	fundamental harmonic of mutual-inductance	H
N	number of winding turns	
P_{in}	input power	W
P_{out}	output power	
$P_{bearing}$	bearing frictional loss	W
P_{SFe}	stator iron loss	W
P_{RFe}	rotor iron loss	W
P_{PM}	magnet loss	W
P_{mech}	mechanical loss	W
P_{cu}	copper loss	W
$P_{Windage}$	windage loss	W
q	number of slots per pole per phase	
Q	number of slots	
Re	Reynolds number	
R_l	load resistance	Ω
R_s	stator resistance	Ω
R_{shaft}	radius of the shaft	m
R_{Rot}	radius of the rotor	m

X_L	load reactance	Ω
X_{sd}	*d*-axis stator reactance	Ω
X_{sq}	*q*-axis stator reactance	Ω

List of Figures

List of Tables

Chapter 1: Introduction

The world's total electrical energy consumption quadrupled from 1973 to 2014 [1], and electrical machines consume about 70% of the total electricity generated. In recent decades, factors like the rising price of energy and standards introduced by organizations such as the International Electro-technical Commission (IEC) were the driving force for extensive research toward high efficiency machines. In the last two decades permanent-magnet machines have been considered as an attractive replacement for conventional induction machines due to their high efficiency and high power density.

Based on the direction of the predominant magnetic flux pattern in the machine, permanent-magnet machines are categorized as radial flux and axial flux as illustrated in Fig. 1.1.

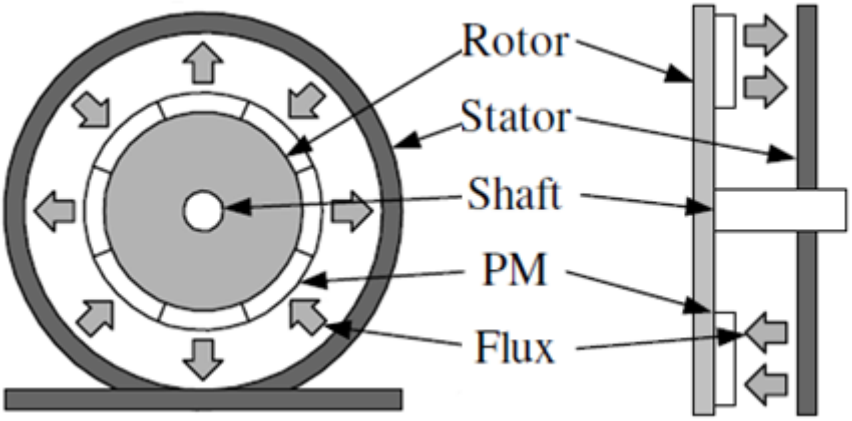

Figure 1.1 Radial (left) and axial flux (right) permanent-magnet machines

This thesis covers two substantially different permanent-magnet machines for two separate industrial applications. The first machine is a 16 kW, 4-pole, radial-flux spoke type interior permanent-magnet machine for a portable AC generator application. The second machine is a 2 kW, 10-pole axial-flux surface mounted permanent-magnet machine for use as a high-efficiency motor. Therefore, this thesis is separated in to two major parts.

1.1 Interior Permanent-Magnet Generators

1.1.1 Background

In the first part of this thesis, a radial-flux spoke type interior permanent-magnet machine for application in a portable AC generator is described. Portable AC generators are used in various applications, especially in areas where no other source of AC power is available.

The key electrical output requirements of small AC generators with ratings less than 25 kW are: a voltage regulation within ±5% of the rated value, capability of operating with low power-factor loads, low total harmonic distortion (THD), operation with unbalanced loads while maintaining acceptable voltage regulation, and high efficiency [2]. In addition, the three-phase voltages of portable generators should be well balanced. This is important when driving induction machines to minimize the negative sequence currents which can cause overheating and shorten their life. The other desired characteristics of the portable generators are as follows:

- short-circuit current of at least three times of the rated current to allow tripping of the fuses/circuit breakers;
- capability of direct-on-line starting of 1-ph and 3-phase induction motors;
- minimal over-voltage transients when large loads are suddenly removed;
- operation with unbalanced loads while maintaining an acceptable voltage regulation;
- operation with low power-factor loads without excessive voltage droop or waveform distortion, and
- parallel operation of multiple generators to obtain higher output powers.

Figure 1.2 shows the block diagrams for three AC generator topologies. This consists of a speed-regulated prime mover such as a diesel or petrol engine along with a generator. Traditionally wound-field synchronous generators are used in such applications and for these machines control of the rotor field current can be conveniently used to maintain a near constant generator output voltage (see Fig. 1.2(a)). With the development of permanent-magnet machines, the use of PM generators is attractive due to their potential for higher efficiency, reduced size and weight, no requirement for field excitation, higher reliability and lower maintenance. However,

voltage regulation is a concern with permanent-magnet generators due to their lack of excitation control (see Fig. 1.2(b)). The much lower synchronous inductance of permanent-magnet generators compared to wound-field generators makes it possible to consider operation without direct output voltage regulation. It is possible to use a power electronics unit to regulate the output voltage and frequency of the PM generator (see Fig. 1.2(c)) but this will result in a significant cost increase. From a cost perspective, it is important that a PM portable generator meets the above voltage regulation and THD requirements without the need for any power electronics control or output power processing. Thus the work in this thesis focuses on the topology in Fig. 1.2(b).

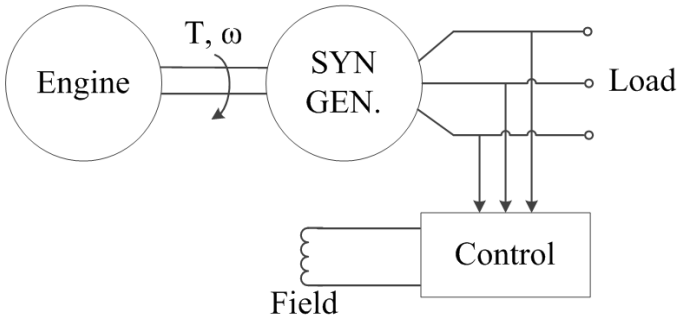

(a) Conventional wound-field synchronous generator.

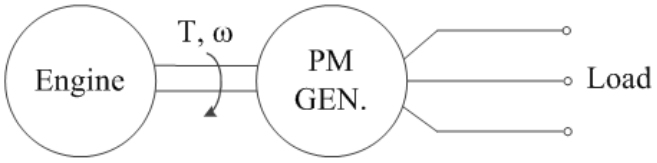

(b) Proposed PM generator.

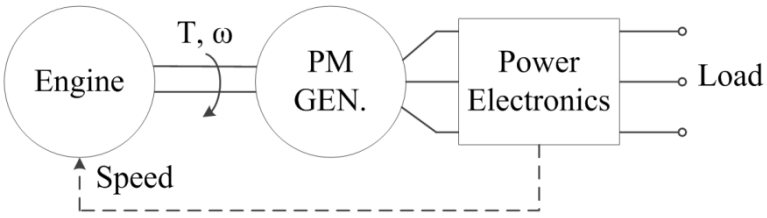

(c) Conventional PM generator with power electronics.

Figure 1.2 Block diagram for three AC generator topologies.

The limited published works on this topic do not fully address the characteristics, benefits and short-comings of PM machines for application as stand-alone portable generators. Wound-field generators still dominate the portable generator market and have not been substituted by PM generators yet.

1.1.2 Motivation and Aims

The aim of this study is to address a research gap in the application of permanent-magnet machines as a stand-alone portable generator, as this area has not been fully explored. The aims of this study can be summarized as follows:

- Analysis of the behaviour of permanent-magnet generators for application of stand-alone portable generators.
- Effect of various design factors like saliency, saturation and stator resistance on the voltage regulation, efficiency and THD.
- Behaviour of the machine under balanced three-phase loads as well as unbalanced, single phase loads.
- Effect of alternative single-phase winding connections on the performance of the machine.
- Performance of the studied PM generator as a motor.

1.1.3 Original Contributions

The original contributions include the following.

1. Effect of design parameters including saliency, stator resistance, and also saturation on the voltage regulation, THD, and efficiency.
2. Comparing the efficiency, fuel consumption, and transient response of the studied IPMG with a similar size wound-field generator with the same diesel prime mover.
3. Analyzing the performance of the three-phase IPMG under single-phase operation by proposing an analytical procedure and comparing voltage regulation, THD, and efficiency results.
4. Proposing a new connection method called open-delta for single-phase operation and also considering a delta connection (which has not used commonly for single-phase operation) and comparing the results with 1-ph and 3-phase star connections. The results for these connections can be generalized for all permanent-magnet machines for the application of 3-ph generators for 1-ph operation.
5. Studying the steady-state and dynamic performance of the machine when run as a motor under open-loop operation as well as its overload capability.

6. Detailed finite-element analysis for demagnetization withstand capacity of the machine as a motor.

1.2 Axial-Flux Permanent Magnet Machines

1.2.1 Background

Electrical machines with high rotational speeds have an extended range of applications including: electric vehicles, blowers, compressors, grinding machines, mixers, pumps, textile machines, drills, aerospace and flywheel energy storage etc. In recent decades, factors like the rising price of energy and standards introduced by organizations such as the International Electro-technical Commission (IEC) were the driving force for extensive research towards high efficiency machines. To achieve this goal both the machine materials and its design should be considered.

Amorphous magnetic material (AMM) has high magnetic permeability (one or two orders of magnitude higher compared to the conventional silicon-iron), and low eddy current and hysteresis losses which has the potential to substantially improve the machine efficiency specifically at high speeds. However, AMM laminations are very thin compared to conventional SI and also have high tensile strength and hardness. Thus the process of stamping, cutting, shaping, and manufacturing of an AMM machine is challenging. AMM application has been mainly limited to transformers [3] or electrical machines with a toroidal shape which do not require any cutting [4-6]. However with the development of improved AMM cutting technology [7-9], the application of AMM in electric machines requiring slotting of the core is now feasible.

From the design point of view, an axial-flux permanent-magnet (AFPM) design is considered as this topology is suitable for AMM designs as it can be more easily manufactured in mass production than the equivalent radial-flux design. In addition, the axial design can also achieve high torque density while offering the potential for lower acoustic noise and vibration compared to the traditional radial-flux permanent-magnet machine designs. The previous studies have not yet shown a practical topology to offer economical and reliable production of high-speed AMM machines at high efficiency.

In this study a novel brushless synchronous 12-slot 10-pole tapered axial-flux permanent-magnet machine utilizing amorphous magnetic material in the stator core has been introduced. The machine is suitable for waterjet cutting and has a rigid structure

suitable for high speed operation. The main benefit of the proposed tapered machine design is to allow convenient manufacturing to utilize the low stator iron loss at high frequencies potential of AMM.

1.2.2 Motivation and Aims

To obtain a high efficiency machine it is essential that the loss components have been identified first. Therefore, suitable loss separation techniques are necessary. The aims and motivation for this research work are summarized as follows:

- Examining an AMM machine design suitable for manufacturing and capable of providing high efficiency at high speed operation.
- Developing accurate methods to calculate and empirically measure the loss components using a combination of finite-element analysis and experimental measurements. These techniques can also be used for other machine types.
- Optimising the efficiency of the studied machine to use the full potential of the low loss characteristics of the AMM material.

1.2.3 Orginal Contributions

The major research contributions developed in the 12-slot 10-pole amorphous magnetic material machines can be summarized as follows:

1. Developing a method to accurately estimate the mechanical loss using a combination of measurements and FE simulation.
2. Detailed loss breakdown under no load and full load conditions.
3. Design modification and successfully achieving an efficiency improvement to 93.5% from 90%.
4. Introducing a novel locked-rotor test method to confirm the loss analysis and accuracy of FE results by removing the uncertainty associated with mechanical losses. This method can be used in verifying the loss breakdown of any synchronous machine.

1.3 Outline of the Thesis

This thesis is developed as followings. Chapters 2 to 4 cover the radial-flux PM machine for the portable AC generator application, and chapters 5 to 6 cover axial-flux PM machines for the high efficiency motor application.

Chapter 2 describes a 16 kW, 4-pole, 3-phase spoke-type interior radial-flux permanent-magnet generator focused on the portable AC generator application without the use of any power electronics. It includes the effect of design factors such as saliency, inverse saliency, stator resistance and saturation on the output voltage versus current characteristics of interior PM generators when operated at a constant speed into a three-phase passive load. The machine parameters and performance were estimated using finite-element analysis and are compared with the measured results. The performance is compared against a baseline wound-field commercial generator showing its higher efficiency and better performance.

In chapter 3, the performance of the studied interior permanent-magnet generator when driving single-phase (1-ph) loads is considered. It examines the effect of three different 1-ph winding configurations: the standard star-connection, the delta connection and also a proposed open-delta connection which has a significantly higher output power. This chapter explains an analytical procedure to estimate the machine performance under 1-phase operation. The simulated results of the voltage regulation, total harmonic distortion, and efficiency are compared with the measured results for the above winding configurations. The results of this study can be used as a guideline for the application of 3-ph generators for 1-ph applications.

Chapter 4 addresses the performance of the IPM machine developed for the portable generator application when run as a motor under open-loop volts-per-hertz control from an inverter. The equivalent circuit and the d-q equations are used to predict the motor performance. The good correspondence between the analytical and measured results, particularly at higher power levels, gives confidence in the modelling approach. Finite-element simulations are used to study the possibility of demagnetizing of the permanent magnets under higher magnet operating temperatures and negative d-axis stator currents.

Chapter 5 compares the performance of three alternative magnetic materials: silicon iron, soft magnetic composite (SMC) and amorphous magnetic material, as the stator of an axial-flux permanent-magnet machine. Three stators of identical dimensions, one of each material, are built and tested with the same rotor. The detailed measurement steps including correcting the torque meter offset and the mechanical loss estimation are presented. The process of separating the losses of each of the machines using a combination of 3D finite-element analysis and experimental testing under open-circuit and loaded conditions is described.

In chapter 6 a novel tapered AMM electrical machine suitable for a range of high-efficiency, high-power density and high-speed machine applications is introduced. It uses a 12-slot 10-pole tapered design utilizing amorphous magnetic material in the stator core. The mechanical loss separation technique described in Chapter 5 as well as a novel locked-rotor test is used to determine the loss breakdown. A significant rotor loss is showed. The rotor design was optimised and a significant improvement in efficiency was demonstrated.

Chapter 7 summarizes the research contributions and includes suggestions for future work.

Chapter 2 : Interior PM Generator for Portable AC Generator Sets

For portable AC electric generator sets, it is desired to maintain a constant output voltage under load. With wound-field synchronous generators, this is done using field current (excitation) control. This type of control is not possible with PM machines; however, theoretical analysis is used to show that an acceptable output voltage regulation can be obtained by two alternative design approaches for the interior PM machines. The design of a 4 pole, 16 kW machine is described and experimental results are provided which demonstrated sinusoidal output waveforms, good voltage regulation and high efficiency.

2.1 Introduction

Portable AC generators are used to provide electricity for isolated loads. A portable AC power set typically consists of a speed-regulated prime mover such as a diesel or petrol engine and a voltage-regulated synchronous generator. According to the Australian Standards, portable generators with ratings less than 25 kW, should have the a voltage regulation within ±5% of the rated value. Portable generators also should be capable of running loads with power-factors between 0.8 lagging and unity [2].

In addition, the three-phase voltages of portable generators should be well balanced. This is important when driving induction machines to minimize the negative sequence currents which can cause overheating and shorten their life. The total harmonic distortion (THD) of the voltage waveform should be less than about 5%. The other desired characteristics of the portable generators are as follows:

- short-circuit current of at least three times of the rated current to allow tripping of the fuses/circuit breakers;
- capability of direct-on-line starting of 1-ph and 3-phase induction motors;
- minimal over-voltage transients when large loads are suddenly removed;
- operation with unbalanced loads while maintaining an acceptable voltage regulation;
- operation with low power-factor loads without excessive voltage droop or waveform distortion, and
- parallel operation of multiple generators to obtain higher output powers.

For the conventional wound-field synchronous generators, control of the rotor field current can be conveniently used to maintain a near constant generator output voltage (see Fig. 2.1(a)).

In the last two decades permanent-magnet (PM) machines have been considered as an excellent substitute for the traditional wound-field electrical machines in various applications due to their distinct advantages. Some of these advantages are: lower size and weight, higher efficiency, no requirement for field excitation, higher reliability and lower maintenance (see Fig. 2.1b) [10-12]. So, PM generators also can be used as a good replacement for the wound-field portable generators. For wound-field DC generators, a cumulative compound series field winding is used to regulate the output

voltage with the load variations. However, voltage regulation is a concern with PM generators due to their lack of excitation control. From a cost perspective, it is important that a PM portable generator meets the above voltage regulation and THD requirements without the need for any power electronics control or output power processing.

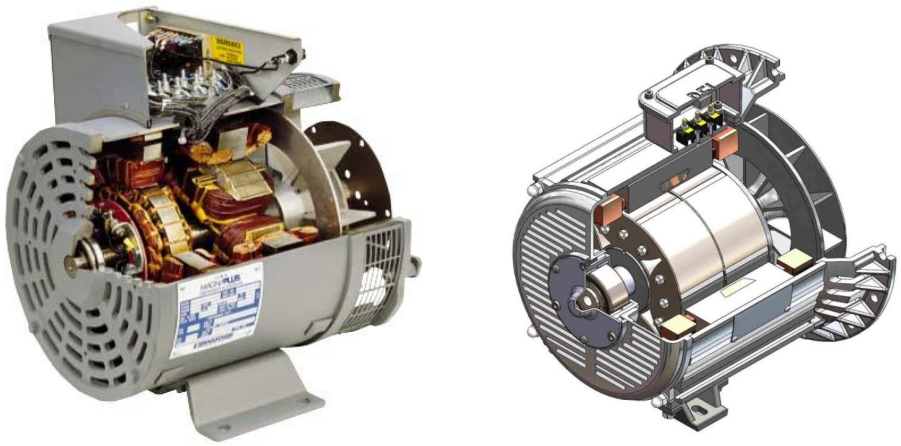

(a) wound-field generator (b) interior PM generator

Figure 2.1 Wound-field and interior PM generator designs.

There are a number of ways which voltage regulation of AC permanent-magnet generators when driving isolated AC loads can be improved. These include: oversizing the machine [11], using series/shunt capacitors [10, 11, 13, 14], using a high-saliency design [15-18] and saturating the stator [19].

The use of series/shunt capacitors were reported in [10, 11]. It has been shown that the output voltage of a 3-ph PM generator can be controlled by adding series or shunt capacitors to generate reactive power. However using fixed capacitor values does not generally produce acceptable voltage regulation over a full range of load currents and power-factors. In [13], Rahman described the control of reactive power using a 3-ph fixed capacitor/thyristor controlled reactor. This concept was extended by Niwas to use for a 3-ph generator while driving a 1-ph load. A 3-ph shunt-connected voltage-source inverter was applied to produce more balanced generator currents [14]. While these approaches can give good performance, their disadvantages including additional cost and control complexity are not negligible.

In [15], Chalmers considered the effect of saliency on the voltage regulation of a 3-phase, 4-pole isolate interior permanent-magnet (IPM) generator. The rotor had open “V shape” PMs and cage bars to guide the flux lines. Therefore, the *d*-axis synchronous reactance was less than the *q*-axis synchronous reactance. The results showed that the

inverse saliency increases the output voltage under load. In [17, 18], Chan applied the same principle to improve the effect of inverse saliency of an inset PM for the isolated generator application. For two current values, zero voltage regulation was achieved.

In [19], Wu presented the effect of stator saturation on the voltage regulation of a double-sided axial-flux PM machine using a heavily saturated stator under the no-load condition. The stator was saturated by reducing its thickness. The armature reaction MMF reduced the degree of saturation under load. Therefore, the stator windings link the same rotating flux without considering the drawn current level and the terminal voltage is not greatly affected by the armature reaction.

There are a few more published works considering the effect of design parameters on the performance of PM AC portable generators [16, 20, 21]. In [16], Kurihara presented a successful design of a "V type" fixed-speed IPM generator for a pico-hydro application without clearly mentioning how the voltage regulation is minimized. To improve the THD, the stator is skewed and the excellent voltage regulation of 0.3% was achieved. However, there is large gap between the simulation and measured results.

In [20], the effect of adding damper bars to the rotor of a small salient pole wound rotor generator was investigated. The results show that damper bars improve the voltage waveform quality under unbalanced load conditions and also the transient performance. However, the impact of damper bars on the voltage regulation and THD was not discussed.

In [21], Kurihara studied the effect of damper bars on the transient stability of the spoke-type IPM generator when subjected to sudden load changes. It was shown that damper bars increase the stability effectively but voltage regulation was not affected. The THD of the output voltage was increased.

The limited published works do not fully address the characteristics, benefits and short-comings of PM machines for the application as stand-alone portable generators. The wound-field generators still dominate the portable generator market and have not been substituted by PM generators yet.

The present chapter focuses on a PM generator for the portable AC generator application to provide a good suitable substitute for wound-field ones. Firstly it analyses the effects of design parameters such as saliency, stator resistance and saturation on the

output voltage versus current characteristics of interior PM generators when operated at a constant speed into a three-phase passive load. Secondly, a spoke-type IPM generator design for a portable generator application is described. The finite-element parameters and performance are compared with the experimental results. Finally, its performance is compared against a base line commercial generator showing it has higher efficiency and better performance.

2.2 Study Procedure

2.2.1 Analysis Approach

IPM generators operating under a balanced resistive-inductive load can be represented with the per-phase equivalent circuit and the phasor diagram as presented in Fig. 2.2 which is identical to that of a salient-pole synchronous generator. The phasor diagram assumes that the magnet flux-linkage is in the *d*-axis.

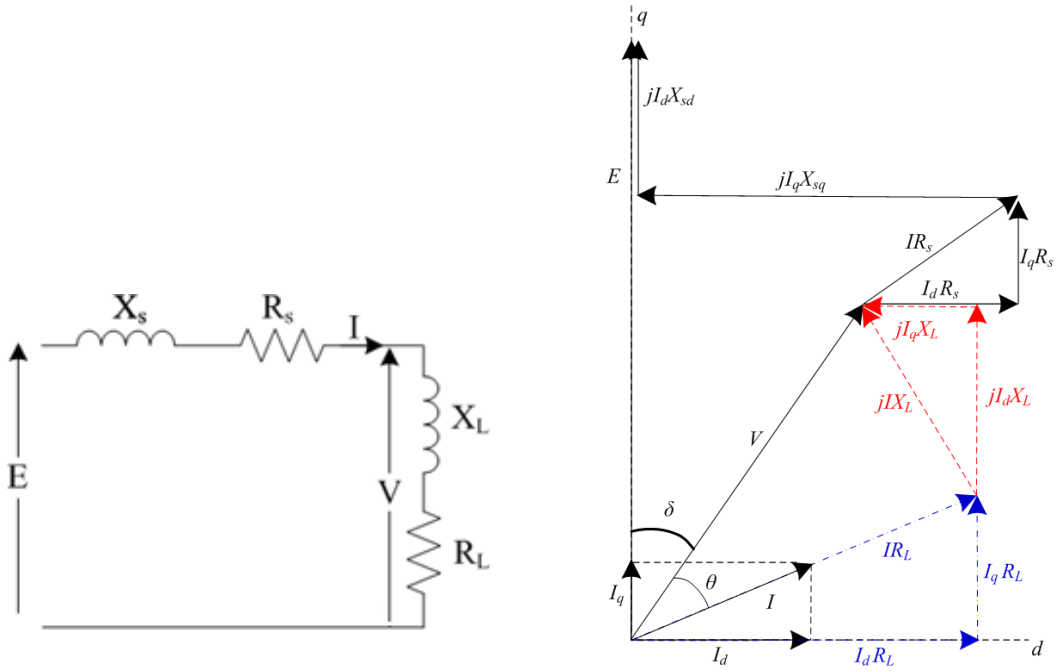

Figure 2.2 Equivalent circuit and phasor diagram of the IPMG when operating with a resistive/reactive load.

The direct and quadrature-axis voltage equations are as:

$$V\cos\delta = E - I_d X_{sd} - I_q R_s$$
$$V\sin\delta = I_q X_{sq} - I_d R_s \qquad (2.1)$$

where I_d, I_q, X_{sd}, X_{sq}, R_s, and E represent the *d*-*q* axis values of the output current and stator reactance, and the stator resistance and induced voltage. The relationship between the load voltage and current can be calculated using the load resistance and reactance as well:

$$\begin{aligned} V\cos\delta &= I_q R_L + I_d X_L \\ V\sin\delta &= I_d R_L - I_q X_L \end{aligned} \tag{2.2}$$

where R_L and X_L represent the load resistance and reactance. Therefore, from these four equations the value of I_d, I_q and the angle δ between *E* and *V* can be determined as:

$$\begin{aligned} I_d &= \frac{E\left(X_{sq} + X_L\right)}{(R_L + R_s)^2 + (X_{sd} + X_L)\left(X_{sq} + X_L\right)} \\ I_q &= \frac{E(R_L + R_s)}{(R_L + R_s)^2 + (X_{sd} + X_L)(X_{sq} + X_L)} \end{aligned} \tag{2.3}$$

$$\delta = \tan^{-1}\left[\frac{I_d R_L - I_q X_L}{I_q R_L + I_d X_L}\right] \tag{2.4}$$

For purely resistive load operation, X_L = 0. Therefore, the machine output voltage *V* corresponding to the resistive load is:

$$V = I(R_S + R_L) \tag{2.5}$$

Magnetic saturation (if present) can be accounted by numerically iterating equations (2.3)-(2.4) using the *d*-axis inductance $X_{sd}(I_d)$ and the *q*-axis inductance $X_{sq}(I_q)$ by updating the value of X_d and X_q until the values of inductance converge.

2.2.2 Finite Element Simulation

For the finite-element analysis, a time-stepping transient 2D FE simulation in JMAG with a coupled electric circuit was used to predict the machine performance when operating under open-circuit and load conditions [22].

The stator 10° mechanical skew, corresponding to one stator slot pitch, has been approximated by averaging the 2D FE voltage and inductance results over this angle. This skew has a significant effect on the shape of the voltage waveforms.

2.2.3 Experimental Testing

For the experimental testing, the test set-up shown in Fig. 2.3 was used. This generator only has a single bearing as it is designed for direct connection to the flywheel of the prime mover. Thus, a special dynamometer arrangement was used to simulate the

engine bearing. The stator of the generator was also mounted on bearings and its input torque was measured from the stator reaction torque using a linear load cell. A Hioki PW3198 power analyzer and a Picoscope 3425 digital oscilloscope with Hall-effect current probes have been employed for testing.

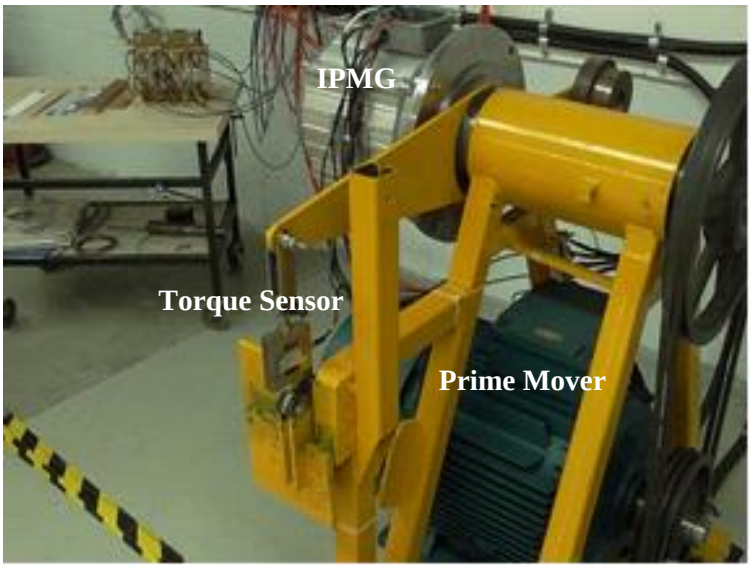

Figure 2.3 Dynamometer test set-up showing IPMG generator (top) connected to prime mover (bottom) using a drive belt. The generator input torque is measured using a reaction torque sensor on its stator.

2.3 Saliency Ratio Effect on Voltage Regulation

To explain the effect of saliency on the voltage regulation, Fig. 2.4 is presented [23]. It includes the voltage-current locus for conventional IPM machines obtained by solving the equations (2.1)-(2.5) for varying the load resistance R_L from 0 to infinity assuming zero stator resistance. The results are normalized to the open-circuit voltage and short-circuit current and are plotted as a function of saliency ratio,

$$\xi = \frac{I_q}{I_d} \tag{2.6}$$

For SPM machines, the rated current is typically about 20% of the short-circuit current while for IPM machines designed for field-weakening operation, the rated current is close to the short-circuit current. As will be mentioned in Section 2.5, although this machine is an IPM machine, it has a high short-circuit current which has a similar ratio to the rated current as SPM machines.

Fig. 2.4 shows that for a non-salient machine ($\xi=1$), the voltage remains relatively constant up to 10% of the short circuit current. This value was increased to 30% for the

saliency ratio of 2. For higher saliency ratios, the output voltage initially increases from no-load and reaches 1.2 and 1.5 pu with the saliency ratio of 4 and 8, respectively.

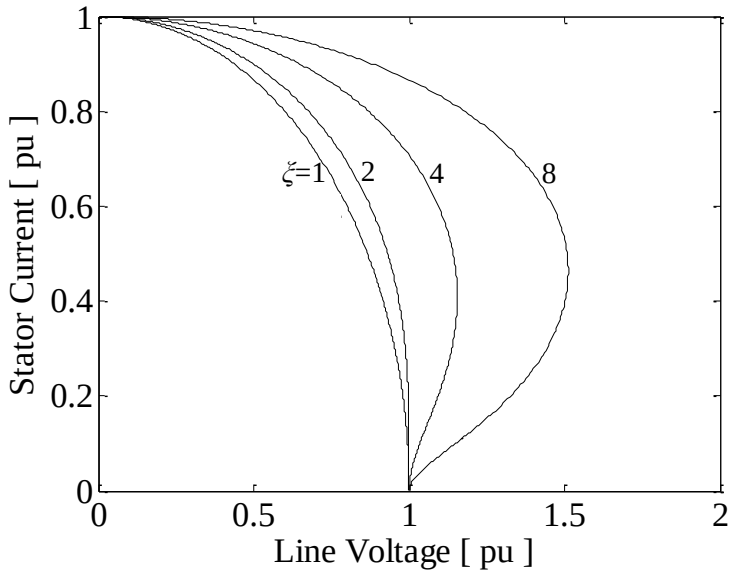

Figure 2.4 Conventional IPM machines with $\xi \geq 1$. Output current versus voltage loci for an ideal machine operated into a three-phase resistive load as a function of saliency ratio.

Fig. 2.5 illustrates the behaviour of IPM machines with an inverse saliency. It is shown that for the machines with inverse saliency, the load current can exceed the short circuit current. For the machines with inverse saliency of 1/4 and 1/8 the load current reaches its maximum value when the terminal voltage drops to 50%. For the machine with inverse saliency, smaller voltage regulation is achievable with the lower saliency ratio.

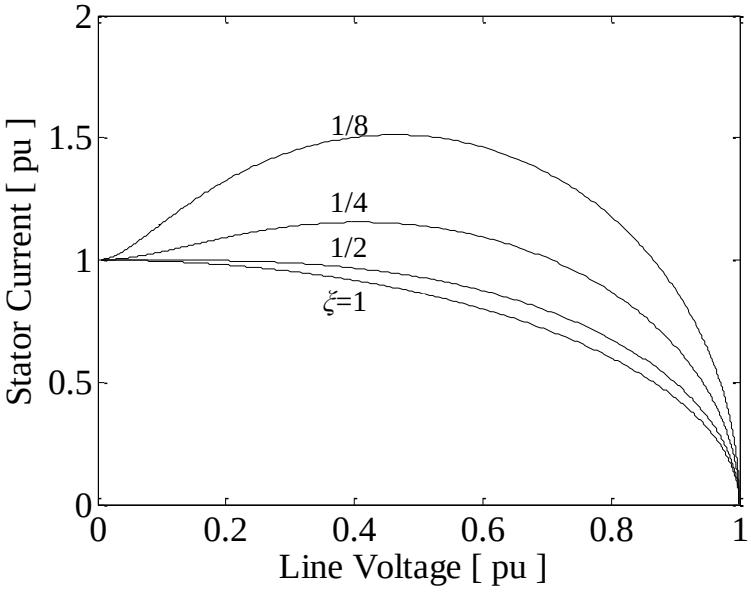

Figure 2.5 Inverse-saliency IPM machines with $\xi \leq 1$. Output current versus voltage loci for an ideal machine operated into a three-phase resistive load as a function of saliency ratio.

2.4 Spoke-Magnet IPM Generator Design and FE Analysis

This section describes the 16 kW 4-pole generator designed by RFL. This has a similar rotor cross-section to that presented in Fig. 2.6(a) but it has a 36 slot stator rather than the 24 slot stator shown. A spoke-type IPM design was selected as it provides good voltage regulation, low total harmonic distortion and high demagnetization withstand capability while requiring minimum PM weight which reduces the total cost of the machine [24]. Fig. 2.6(b) illustrates the machine. The rotor includes barriers and a triangular void to guide the magnet flux. The holes in the rotor are for the bolts used in the assembly of the rotor. These bolts join the two endplates which are used to retain the magnets axially. The stator windings have been short-pitched and the stator is skewed by one slot pitch to improve the back-emf waveform shape. Table 2.1 and Fig. 2.7 show the design information and the BH curve of the stator and rotor material, respectively.

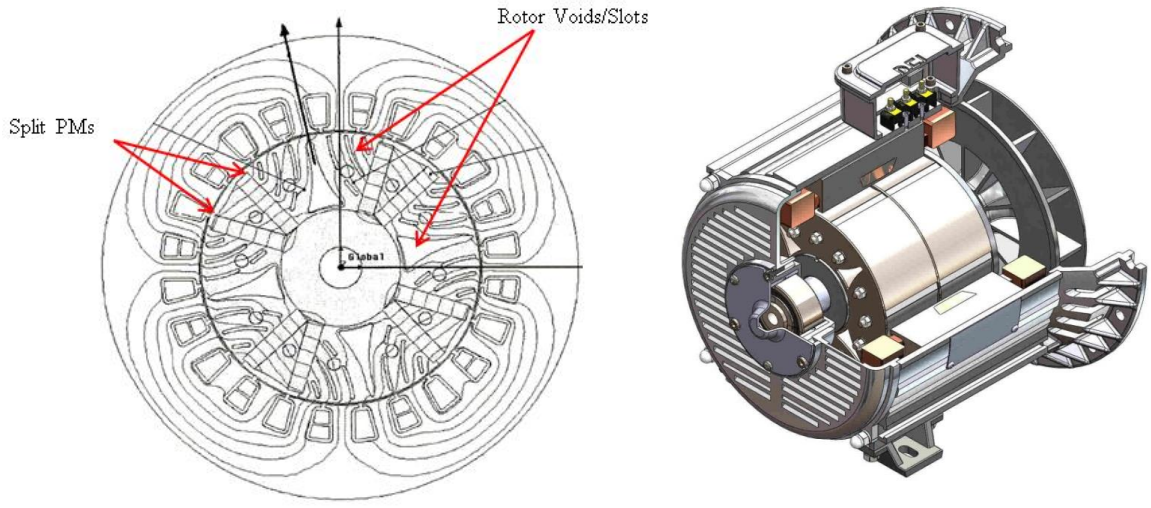

(a) (b)

Figure 2.6 The 16-kW spoke-type IPM generator, (a) example of calculated flux under the loaded condition, (b) picture of the assembled machine [24].

Table 2.1 16 kW Generator Design Information

Parameter	***Value***
Performance	
- output power (kVA/kW)	20 kVA/16 kW
- output voltage: line/phase	400V / 230V
- rated current	24.3 A
- poles / frequency	4 poles / 50 Hz
- rated speed	1500 rpm
Key dimensions	
- stator outer/inner diameters	254 / 172 mm
- airgap length	1 mm
- stack length	130 mm

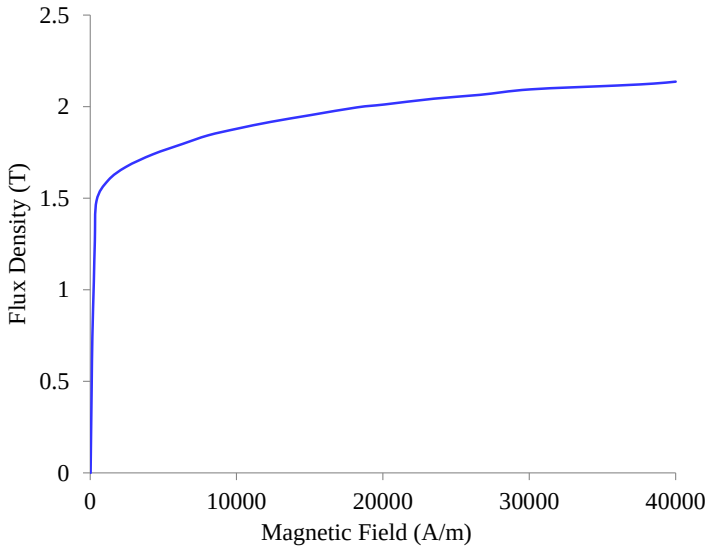

Figure 2.7 The BH curve of the stator and rotor material.

2.5 Calculated and Measured Machine Parameters

Fig. 2.8 shows contour plots of the magnetic flux density distribution and flux lines of the stator under open-circuit and full load conditions. Considering the BH curve of the stator material presented in Fig. 2.7, the stator has a high level of saturation even under open-circuit conditions which improves the voltage regulation. The machine has a stator yoke flux density of about 2.1 T under both open-circuit and full-load conditions. The stator teeth also show high flux densities, about 1.8 T under open circuit that is increased to about 2.2 T at full load. The rotor shows much less saturation than the stator with maximum flux densities of about 1.8 T in the rotor barriers.

Saturating the stator of the machine can significantly improve its output voltage regulation because the flux-linkage (and hence output voltage) becomes less sensitive to the stator currents. However, in the case of rotor saturation, the saliency ratio reduces and hence the voltage regulation worsens.

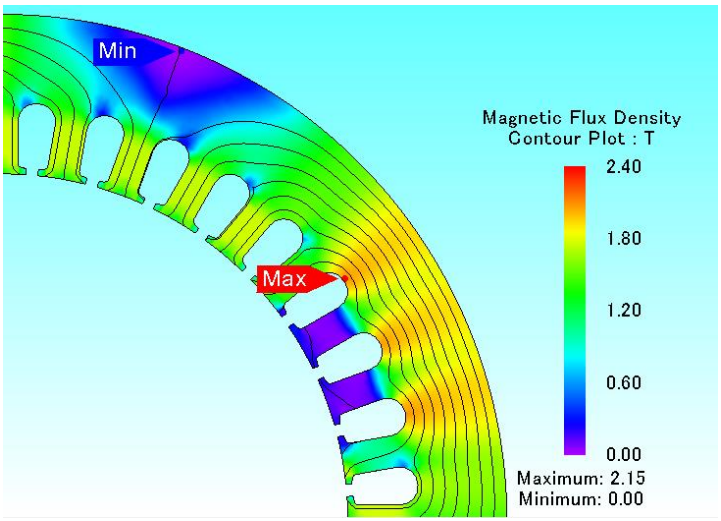

(a) open circuit

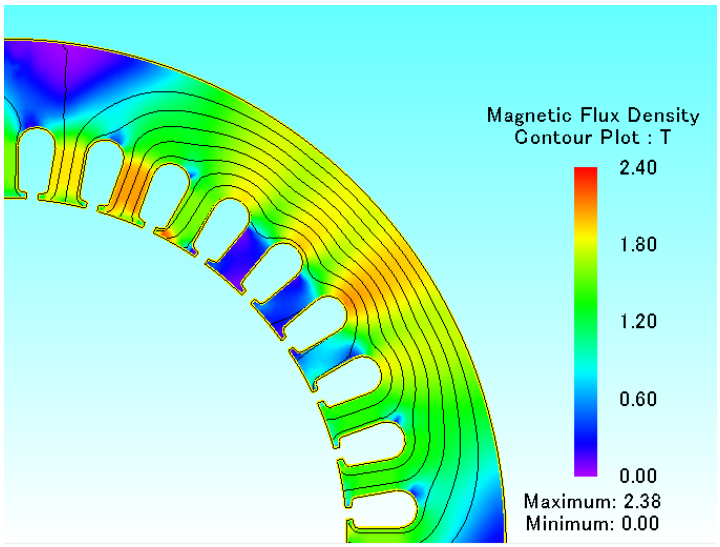

(b) full load

Figure 2.8 Calculated magnetic flux density of the stator in open circuit and full load conditions showing the maximum flux density value.

Fig. 2.9 shows the FE calculated *d*-axis and *q*-axis flux-linkages. The black dashed vertical line shows the rated current. For SPM machines, the rated current is usually about 20% of the short-circuit current. The dashed lines indicate the linearised flux-linkage versus current approximation. For positive *d*-axis currents, the stator mmf aids the magnet mmf and saturates the machine. However, for the negative *d*-axis current, the stator mmf opposes the magnet mmf and reduces the total flux. This figure shows the typical near straight line result between the open-circuit flux-linkage (about 0.7 V.s) and the so called 'characteristic current' of about 110 A corresponding to zero flux-linkage or high-speed short-circuit operation.

Fig. 2.10 depicts the calculated inductances. The dashed lines shows the constant values used in analytical calculation in the case of modeling the machine without saturation. The high *q*-axis inductance due to the rotor bridges reduces with high degree of saturation and results in a low saliency machine. At the rated load, the saliency ratio of this machine is about 1.5.

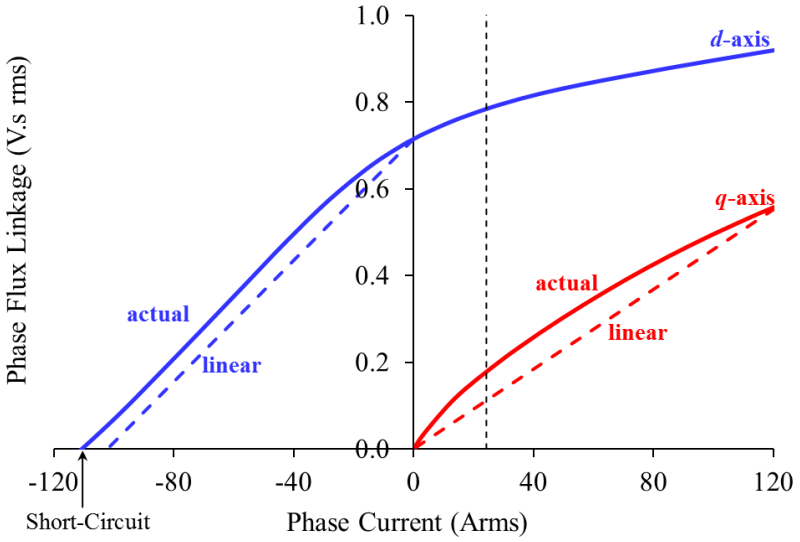

Figure 2.9 Calculated *d*- and *q*-axis flux-linkage results showing actual curves and linear approximations. Rated current shown using a dashed vertical line.

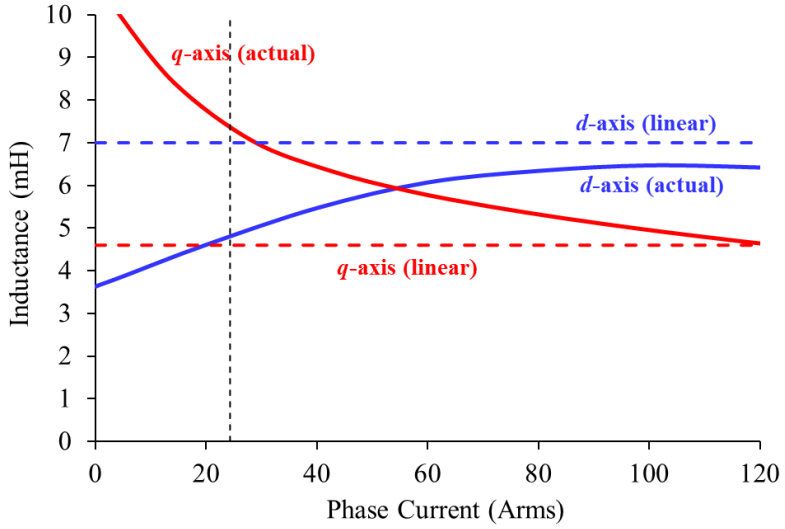

Figure 2.10 Calculated *d*- and *q*-axis inductance characteristics showing actual curves and inductances from linearly approximating the flux-linkage curves. The *d*-axis inductance corresponds to negative values of *d*-axis current.

Fig. 2.11 shows the calculated *d*- and *q*-axis flux-linkage curves previously shown in Fig. 2.9 with additional cross-saturation curves corresponding to the rated output condition (I_d = -5 A, I_q = 24 A). Given the high degree of saturation in the machine, it is not surprising that cross-saturation is significant. For the *d*-axis, when increasing I_q the

d-axis flux-linkage stays almost constant for low currents. At higher positive *d*-axis currents, I_q causes the stator iron to saturate and the *d*-axis flux linkage to decrease. The results of the *q*-axis flux-linkage were similar to the *d*-axis. For high negative *d*-axis currents, the *d*-axis flux-linkage increases with I_q. The cross-saturation results for 50% and 100% of rated axis current are similar.

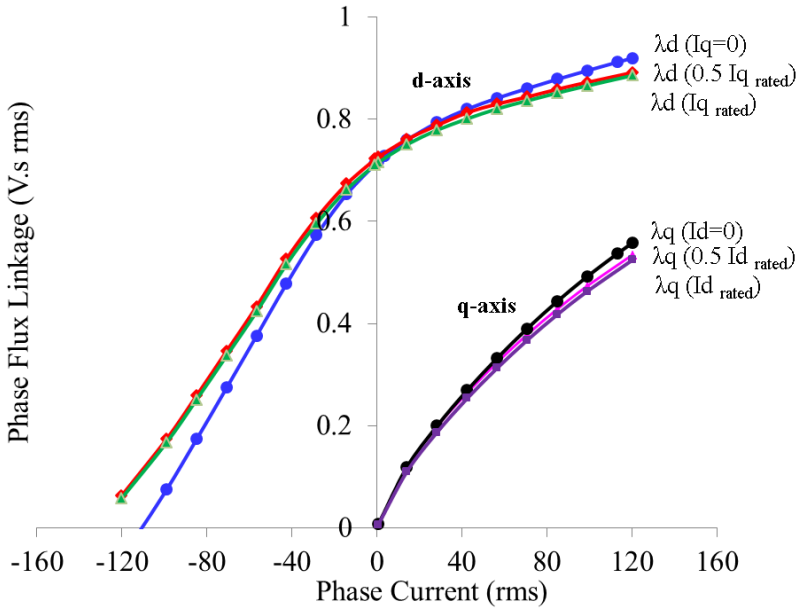

Figure 2.11 Calculated *d*- and *q*-axis flux-linkage curves showing the effect of cross saturation.

2.6 Calculated and Measured Machine Performance

2.6.1 Voltage Regulation

In this section, the effect of inductance and stator winding resistance on the behaviour of the studied machine has been presented. To clarify the difference between the effects of these parameters, four different assumptions are considered:

- ideal model: linear inductances, $R_s = 0\Omega$
- with R_s: linear inductances, $R_s = 0.272\Omega$ (the measured stator winding resistance of each phase)
- with saturation: actual inductances, $R_s = 0\Omega$
- with R_s and saturation: actual inductances, $R_s = 0.272\Omega$

Fig. 2.12 compares the analytically calculated, FE simulation, and measured voltage regulation of the studied IPM generator. Although the ideal model (including constant inductance and zero resistance) is not a real condition it still provides a useful reference point. First, consider the "with R_s" graph. It is shown that voltage regulation increases

by considering the effect of resistance. This result was expected due to the voltage drop across the resistance. Second, including the effect of saturation (particularly the *d*-axis saturation) improves the voltage regulation compared to the ideal model. Saturation reduces the effect of stator current on the flux linkage and hence induced voltage. Third, considering the resistance and saturation together improves the voltage regulation compared to the stator resistance condition. So, it can be concluded that saturation and stator resistance have opposite effects. Therefore, designing a PM machine with low saliency and significant degree of stator saturation will improve the voltage regulation (however, saturation may increase the iron loss). This figure also indicates that for lighter loads, the voltage regulation is more sensitive to resistance, while the voltage regulation of heavier loads is more sensitive to saturation.

The FE results are in excellent agreement with the measured voltage regulation and showing about 5% voltage regulation under 16 kW rated load.

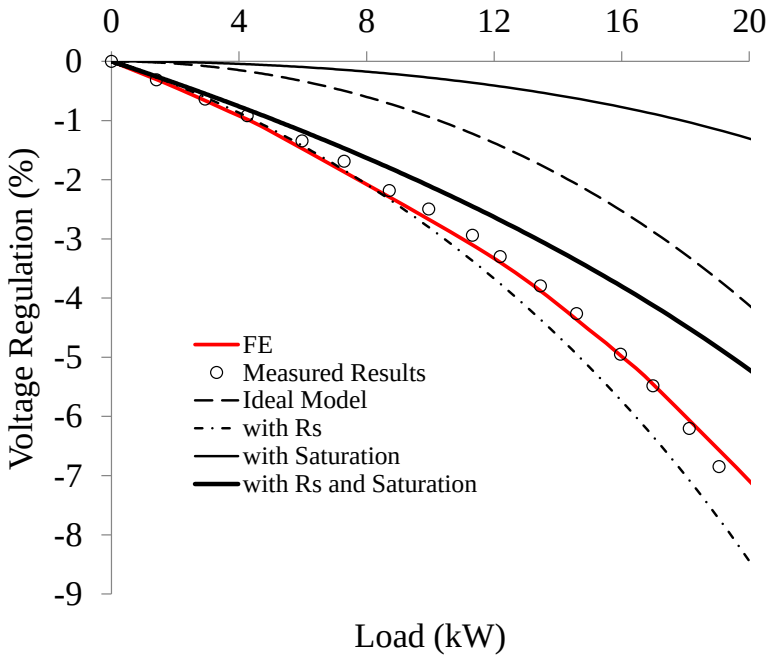

Figure 2.12 FE, measured and calculated voltage regulation for four different model assumptions.

Fig. 2.13 shows the voltage-current diagrams. The measured and analytically calculated characteristics have acceptable agreement. However, the measured results are closer to the "with R_s" graph rather than the "with R_s and saturation" ones. This can be explained considering the value of inductances in these curves. The inductance of the "with R_s" graph is close to the saturated inductance however, the "with R_s and saturation" curve uses the $L_d(I_d)$ and $L_q(I_q)$ saturation curves. It seems that this machine

has cross saturation which is reasonable considering the high degree of saturation in this machine. Cross saturation means that L_d and L_q are not only functions of their respective axis currents but that they are functions of both I_d and I_q. In addition, during test, the machine temperature increased which affects the accuracy of the results. By comparing the measured voltage-current values with the presented results in Fig. 2.4, the low saliency ratio of this machine is confirmed.

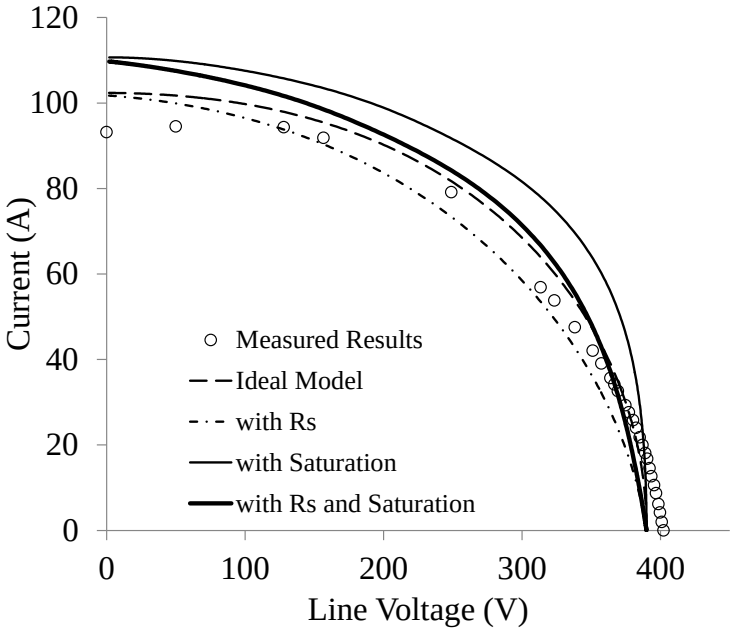

Figure 2.13 Calculated and measured current versus voltage characteristics showing calculated results with four different model assumptions.

2.6.2 THD

Fig. 2.14 compares the FE calculated and measured line and phase voltage waveforms for the open-circuit and the full-load conditions. To compensate for the stator one pitch skew, the FE results are averaged over 10° mechanical. There is a good correspondence between the results.

Fig. 2.15(a) shows the FE calculated and measured THD of the line and phase voltages. Fig. 2.15(b) shows the corresponding harmonic content of the line and phase voltage under open-circuit and full-load conditions as a percentage of the fundamental component. The large triplen harmonic component in the phase voltage increases with load, leads to a small increase of the phase voltage THD from 4.9% at open circuit to 5.8% at full load. In the line voltage, the triplen harmonics are not present and the amplitude of most of the other odd harmonics and hence the THD reduces with load

resulting in the excellent THD of 1% in the rated condition. The measured THD of the line voltage shows a good correspondence with the FE results. Tables 2.2 and 2.3 summarize these results.

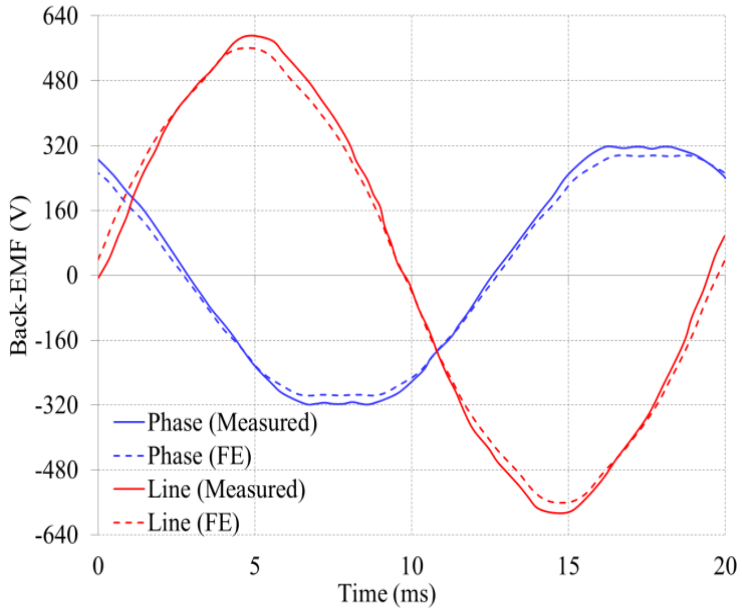

(a) open circuit

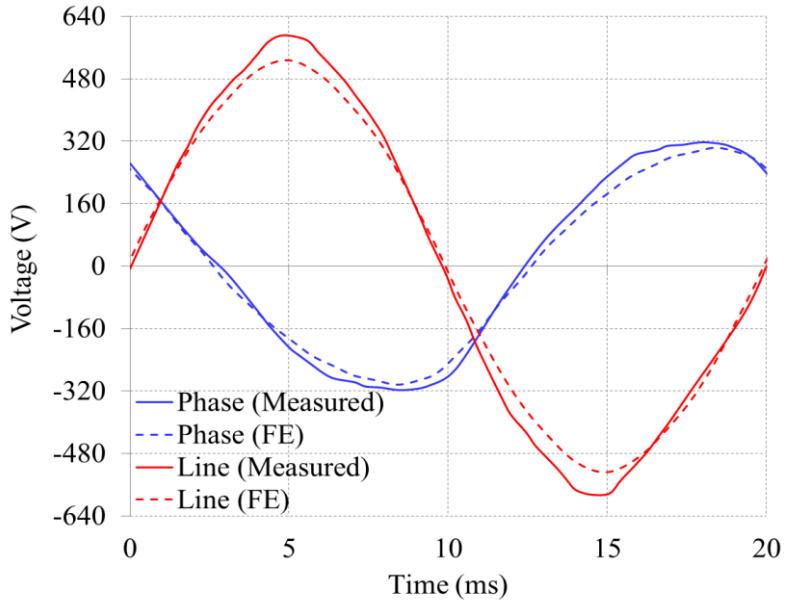

(b) full-load

Figure 2.14 Comparison of FE and measured phase and line voltages waveforms at 1,500 rpm, (a) open circuit, and (b) full load.

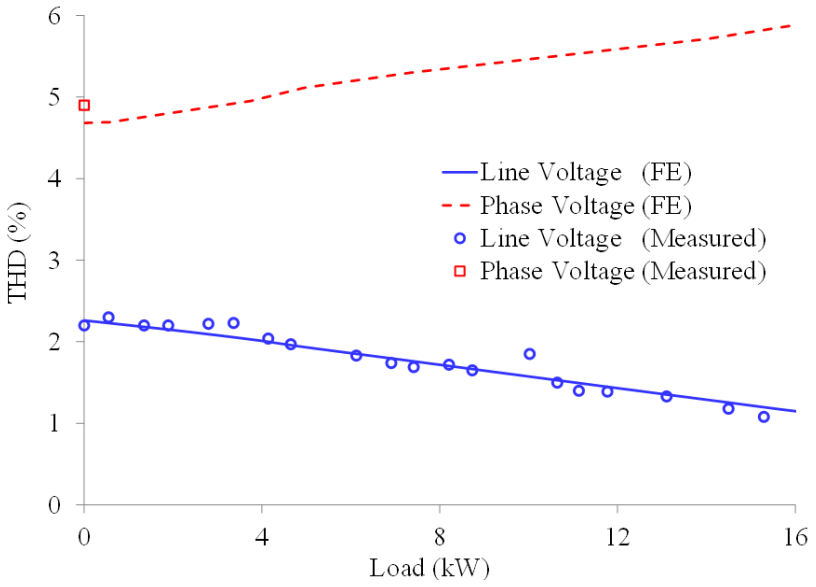

(a)

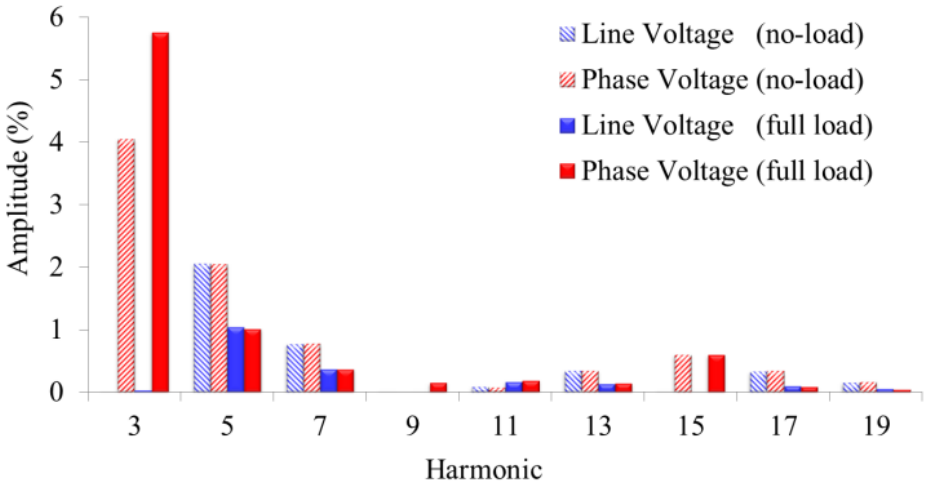

(b)

Figure 2.15 THD and harmonic content of line and phase voltage with three-phase resistive load in open-circuit and full-load conditions, (a) THD, (b) calculated harmonic content.

Table 2.2 Calculated THD of Phase and Line Voltages with Resistive Load

THD	Open-circuit		Full load	
	Phase	Line	Phase	Line
FE	4.7%	2.3%	5.9%	1.2%
Measured	4.9%	2.2%	-	1.1%

Table 2.3 Calculated Harmonic Content of Phase and Line Voltages with Resistive Load

Harmonic number	Open-circuit		Full load	
	Phase	Line	Phase	Line
3	4.05%	0.02%	5.76%	0.04%
5	2.05%	2.06%	1.02%	1.04%
7	0.78%	0.77%	0.37%	0.37%
9	0.02%	0.02%	0.16%	0.02%

2.6.3 Loss and Efficiency

The time stepping FE model is applied to calculate the iron loss as a post processing operation. To calculate the iron loss, the magnetic flux density variations in each element of the machine are calculated as a function of time. Then, the results are analyzed to determine the amplitudes of the harmonics of the magnetic flux density in each element under different frequencies. The iron loss model is used to predict the resultant iron loss in each element including the separated values for hysteresis loss and eddy-current loss. The losses in the elements are then added to estimate the loss in the entire machine. It should be noted that the iron loss due to two-dimensional rotating magnetic fields are modelled by separately considering the orthogonal field components. This is only a rough approximation but is widely used in finite-element analysis.

The open-circuit loss is measured by rotating the machine over a range of speeds and recording the input power when the output terminals are open-circuited and hence the output power is zero. This loss contains the iron loss and mechanical loss including the windage and bearing losses.

Fig. 2.16 compares the FE calculated open-circuit loss with the measured loss up to 2500 rpm. The results were in good agreement. It should be noted that the calculated loss only includes the iron loss and does not consider the mechanical loss. This explains the slightly higher than measured open-circuit loss in the graph.

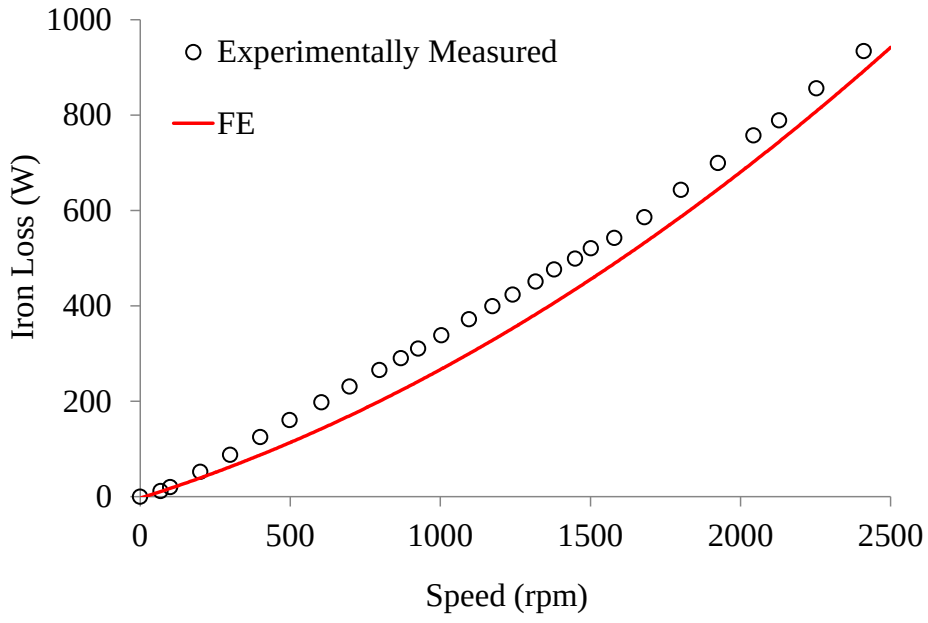

Figure 2.16 Calculated iron loss and measured open-circuit loss versus speed.

Fig. 2.17 compares the measured, FE and analytically calculated efficiencies at 1500 rpm for loads up to 20 kW. The measured open circuit loss from Fig. 2.16 is included in the analytical results. Adding the resistance to the ideal model provides a better estimation of the efficiency compared to the ideal condition. This shows the importance of copper loss especially at larger loads. Saturation has a negligible effect on efficiency. The graph also shows that FE overestimates the efficiency and provides less accurate results compared to the analytical results using equivalent circuit and the measured parameters and open-circuit loss. This is due to neglecting the effect of mechanical loss in the FE where the analytical results include the measured open-circuit loss which contains the mechanical loss. In general, a good agreement between the results is achieved.

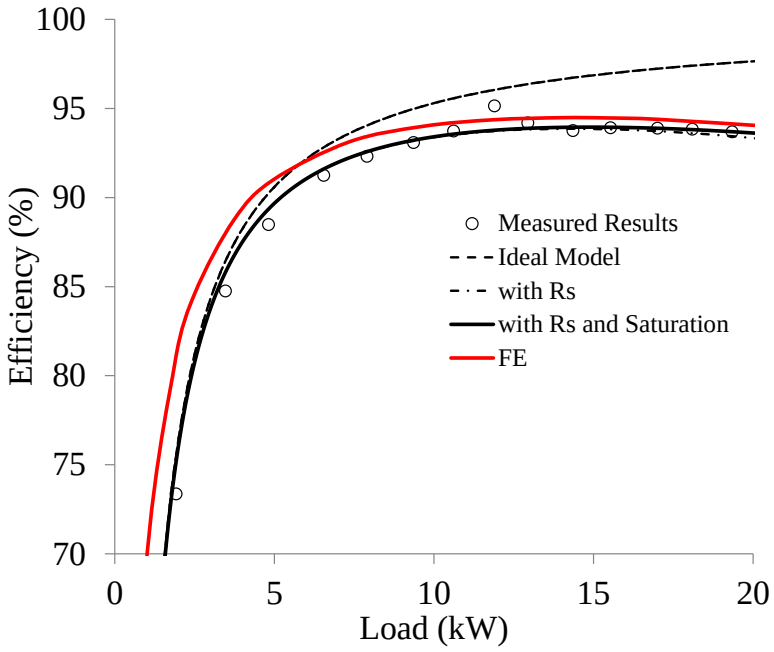

Figure 2.17 Calculated and measured efficiency for two different model assumptions.

2.6.4 Torque and Cogging Torque

Fig. 2.18(a) compares the FE calculated cogging torque waveform and the measured peak static cogging torque values. The cogging torque was measured as the reaction torque on the stator using a torque arm and force transducer. The peak cogging torque was measured by rotating the shaft at very low speeds and recording the peak torque variation where the output of the force transducer was calibrated to read the torque directly. The calculated cogging torque has a good correspondence with the peak measured value.

Fig. 2.18(b) shows the FE calculated instantaneous input torque at the rated output power loading. It has been shown that the input torque is relatively smooth and only has 6^{th} harmonic variation with an average input torque of 108 Nm.

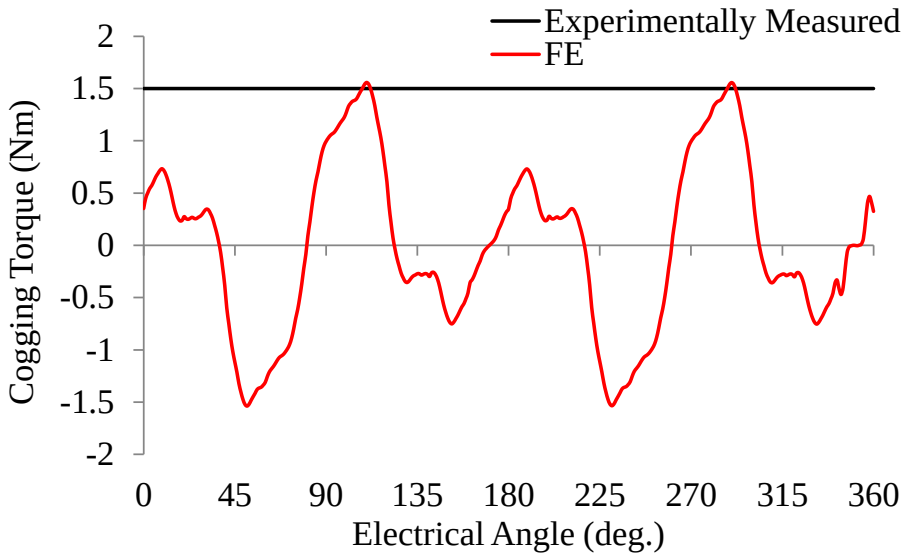

(a)

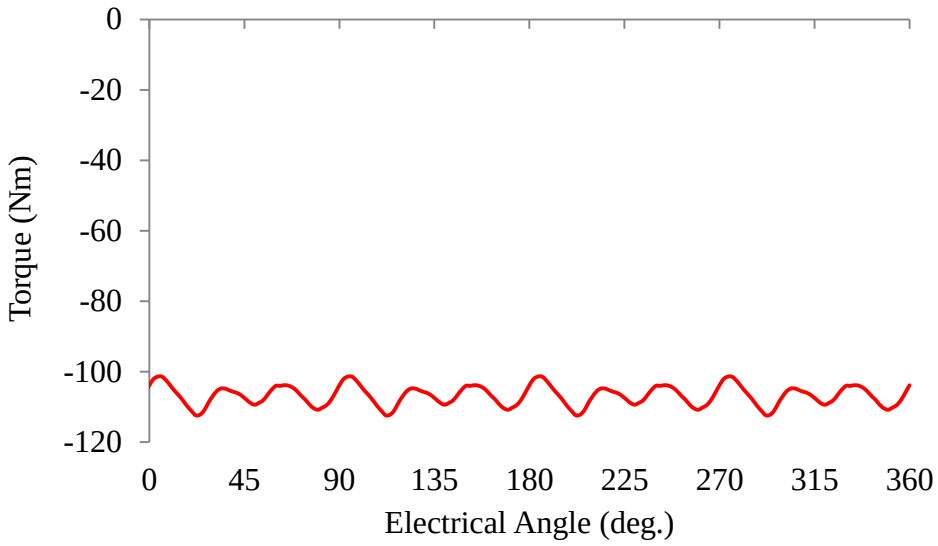

(b)

Figure 2.18 (a) Calculated cogging torque waveform versus rotor position along with the measured peak cogging torque value (horizontal line), (b) calculated input torque.

2.7 Comparison with Conventional Wound-Field Baseline Generator

The measured performance of the studied IPM generator has been compared with a high quality wound-field generator (the tests are conducted by the industry partner). Fig. 2.19 shows these two generators and the same prime mover used for the measurements.

It is noted that the IPM generator has 54% shorter axial length and is 41% lighter compared to the wound field one.

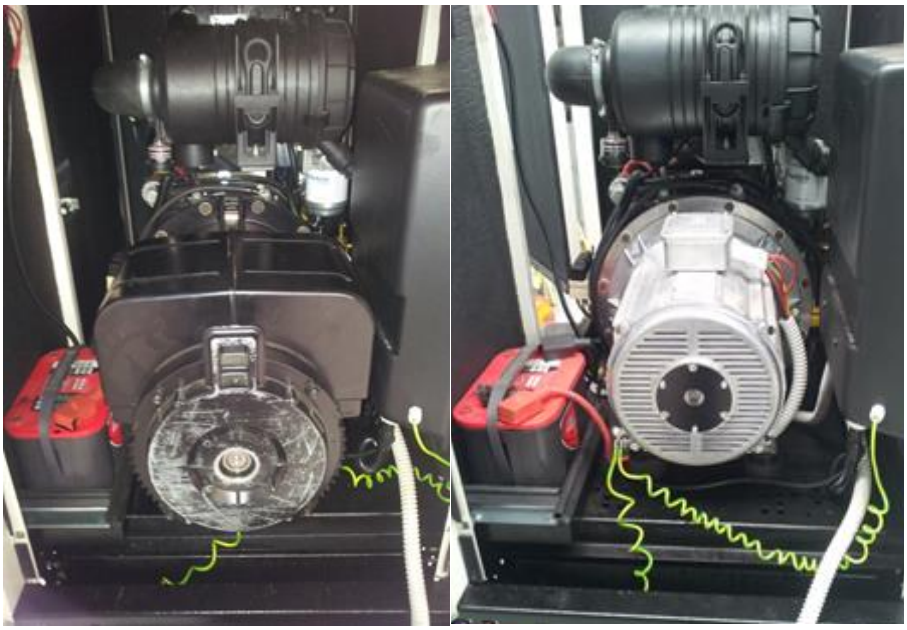

Figure 2.19 Conventional wound-field baseline unit (left) and IPM generator (right) connected to the same prime mover.

Table 2.4 compares the performance of the studied IPM generator and the baseline wound field one. The results indicate the rated efficiency of 94% for the IPM generator which is 6% higher compared to the wound field one.

Table 2.4 Measured Performance Comparison of 20 kVA, Four-Pole Generator Units

Model	Baseline Wound-Field Generator	IPM Generator
Phases / Frequency	3 ph / 50 Hz	3 ph / 50 Hz
Speed	1500 rpm	1500 rpm
kVA Rating	20 kVA	20 kVA
Generator Efficiency	88 %	94 %
Fuel Consumption @ 16.2 kW - litres per hour - grams / kW.hr	 5.19 lph 267 g/kWh	 4.75 lph 244 g/kWh
Running Cost @ 16.2 kW	AUD $7.64 / hr	AUD $6.98 / hr
Axial Length	555 mm	300 mm
Total Weight	102 kg	60 kg

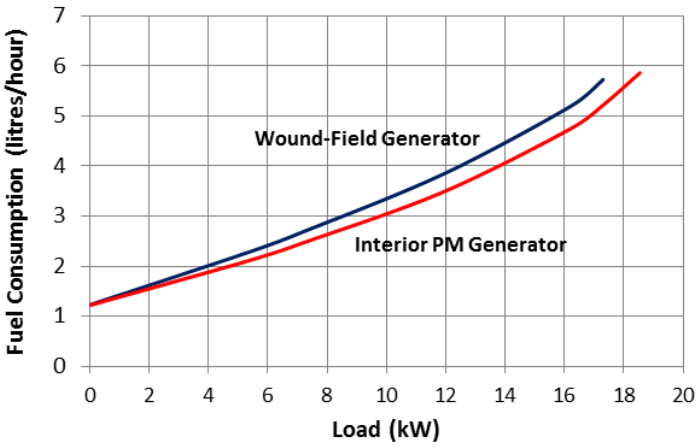

(a)

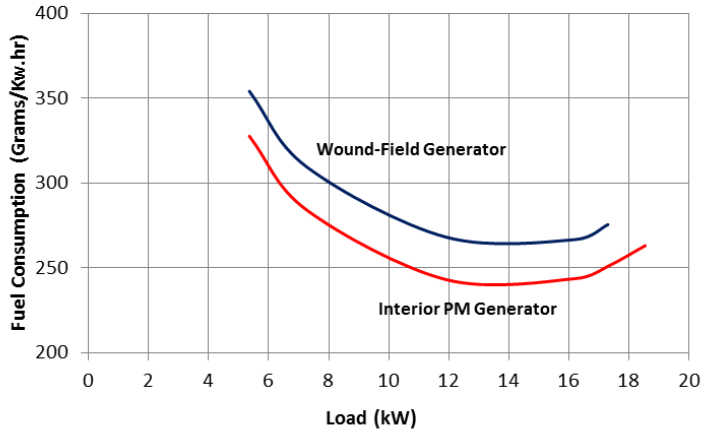

(b)

Figure 2.20 Measured prime mover fuel consumption versus output power for wound-field and IPM generator in (a) litres/hour, (b) grams/kW.hr.

Fig. 2.20(a) depicts the fuel consumption of the prime mover for different loads in litres per hour. The fuel consumption of these two generators was similar for the light loads but it is reduced for heavier loads using the IPM generator. The measured grams per kW hour fuel consumption of these two generators (see Fig. 2.20(b)) indicate a near constant 25 grams per kW.hr lower fuel consumption for the IPM generator. In general, the IPM generator reduced the fuel consumption of the prime mover by 8.6%.

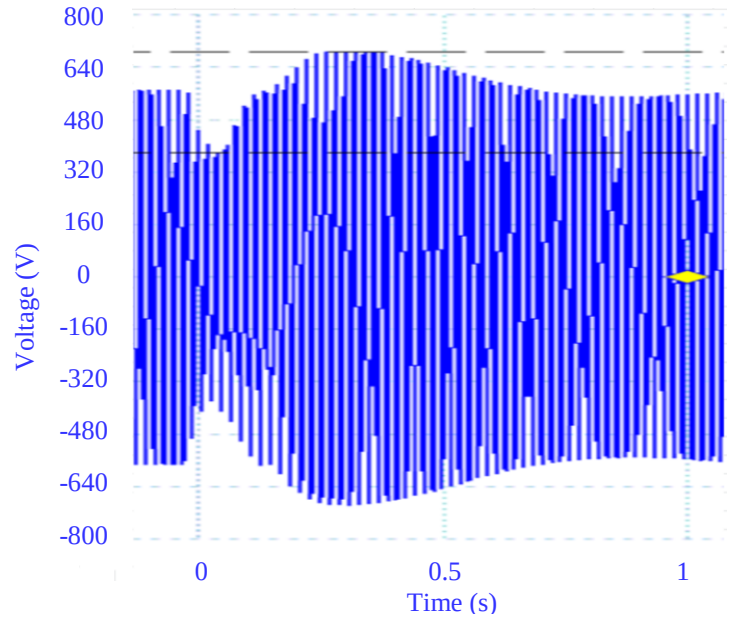

(a)

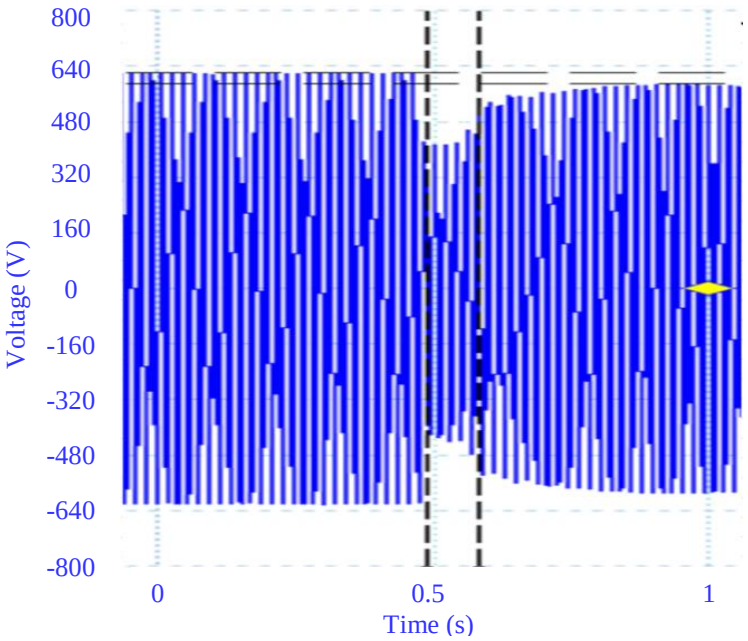

(b)

Figure 2.21 Measured output voltage versus time transient waveforms when starting an induction motor, (a) wound-field, (b) IPM generator. Scaling is 160 V/div.

The transient behavior of the output voltage of the IPM generator has also been measured and compared with the baseline wound field generator. Figs. 2.21(a) and (b) compares the output voltages when starting a 5.5 kW, 3-phase induction machine. A short voltage dip was noticed for both generators due to the high starting current however, only the baseline generator showed a 15% voltage overshoot. In general, using the IPM generator improved the transient response where using an automatic voltage

regulator (AVR) of the wound field generator causes considerable output voltage transients.

2.8 Conclusion

This chapter describes the analysis and testing of a novel 16 kW, four-pole spoke-type IPM generator for portable generator applications with a tight output voltage regulation, sinusoidal output voltage waveforms, high efficiency and good transient performance. The rotor of the machine has voids and slots to guide the magnet flux and the stator has short-pitched windings with one stator slot skew to produce a sinusoidal back-emf waveform under both no-load and loaded conditions. The key results are as follows.

There are two methods to improve the voltage regulation of the IPM generators: designing the machine to have high saliency or designing the stator to be saturated under no-load. The inductance test showed that this machine does not have a high saliency ratio. However, the magnetic flux density contour plot of the stator showed a significant degree of saturation even under the no-load.

The machine performance including the voltage regulation, total harmonic distortion, loss, efficiency, and cogging torque have been measured and compared with the calculated results. The calculated and measured results are in good agreement in general. In addition, under the rated condition, the machine meets the 5% voltage regulation and THD requirements.

An experimental comparison was performed against a high-quality commercial wound-field synchronous generator with the same inner/outer diameter using the same prime mover. The IPM generator has 54% shorter axial length and is 41% lighter compared to the wound field one. The IPM generator is 94% efficient which is 6% higher than the efficiency of the wound field generator. The results showed 8.6% reduction of fuel consumption for the IPM generator. The studied machine also has considerably better output voltage transient response.

Chapter 3 : Single-Phase Loading Behavior of the Isolated 3ph Interior PM Generator

This chapter examines the performance of a 3ph interior permanent-magnet generator used in a portable AC generator when directly driving isolated single-phase (1-ph) AC loads. The performance of the generator was compared under three alternative connections: 1-ph star, 1-ph delta and a proposed “open delta” connection. The voltage regulation, total harmonic distortion and efficiency as three main performance criteria of the portable generators were examined using analytical calculation, finite element simulation and experimental measurements.

3.1 Introduction

In the previous chapter, the design, analysis, simulation and testing of a 16 kW, three-phase (3-ph), spoke interior permanent-magnet generator (IPMG) was described. The analysis was based on the *d/q*-axis equivalent circuit model and measured parameters. It was shown that the use of a high degree of stator saturation significantly improved the voltage regulation. Measured performance (voltage regulation, THD and efficiency) results under 3-ph loading operation were used to validate the analytical and time-stepping finite-element results.

The key requirements for a 3-ph generator when driving isolated AC loads are to maintain tight voltage regulation, good voltage waveform quality and high efficiency over a wide range of load conditions including unbalanced operation such as running single-phase loads. As it is a common practice for three-phase generators to run single-phase loads, it is important to study their behavior in this condition.

Earlier work [10, 11] has shown that the output voltage of a 3-ph PM generator can be controlled by adding series or shunt capacitors to generate reactive power. However using fixed capacitor values does not generally produce acceptable voltage regulation over a full range of load currents and power-factors. Control of reactive power using a 3-ph fixed capacitor, thyristor controlled reactor was described in [13]. This concept was also applied to a 3-ph generator driving a 1-ph load by using a 3-ph shunt-connected voltage-source inverter to produce more balanced generator currents [14]. However, the additional cost and control complexity need to be considered.

This chapter extends the earlier work by examining the performance of the same 3-ph generator when driving single-phase (1-ph) loads without the use of any power electronics [25, 26]. It examines the effect of three different 1-ph winding configurations: the standard star-connection, a delta connection to given better THD and also a proposed open-delta connection with higher output power. The results for these connections can be generalized for all permanent-magnet machines as the studied machine is a case study. The enclosed chapter can be used as a guideline for application of any 3-ph generators for 1-ph applications.

3.2 Winding Connections

Four winding connections are examined as shown in Fig. 3.1. It is assumed that the key factor limiting the output power is that the phase currents should not exceed the rated value.

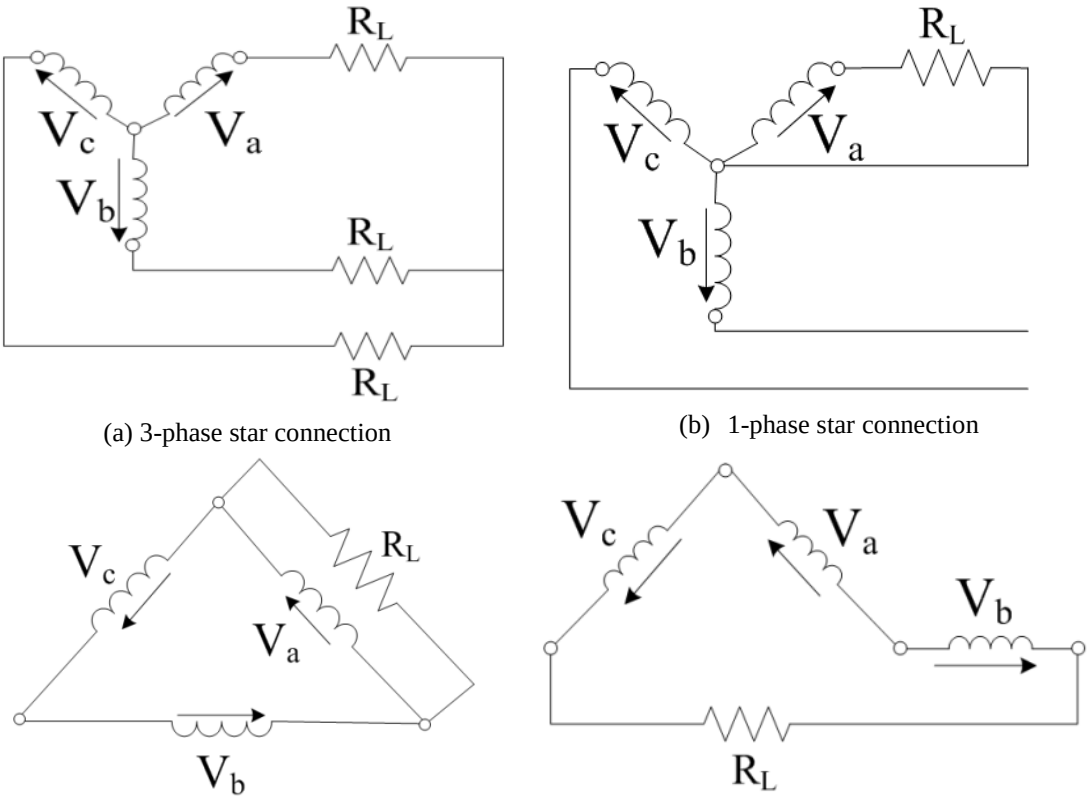

Figure 3.1 The four generator winding configurations examined.

The first two winding arrangements are a star-connected generator with a balanced 3-ph resistive load, Fig. 3.1(a), and a single-phase resistive load, Fig. 3.1(b). With a single-phase star connection, the output power is one-third of the rated 3-ph output power. The advantage of the star-connection is that it can be used to drive both 3-ph 400 V loads and 1-ph 230 V loads simultaneously.

The third configuration is a delta-connected generator with the single-phase load connected across the *a* phase, Fig. 3.1(c). Here the load is supplied by all three phases of the machine where phases *b* and *c* are in series and are in parallel with phase *a*. This configuration allows producing an output power of about 50% of the rated 3-ph output power. This connection can be used to drive both 3-ph 230 V loads and 1-ph 230 V

loads simultaneously. It would be expected that there will be some triplen circulating currents in this configuration which will increase the copper loss.

The fourth configuration is referred to as "open-delta" which produces a single-phase output by placing all three phases in series with phase *b* having an opposite polarity to the other phases, Fig. 3.1(d). It is theoretically capable of producing two-thirds of the rated 3-ph output power of the machine. In this configuration, the output power and voltage are approximately twice compared to the 1-ph star connection. Producing the nominal output voltage with this configuration would require halving the number of stator turns.

3.3 Analytical Model

To analytically calculate the voltages of the three phases under unbalanced conditions it is necessary to find the self and mutual inductances. These can be calculated using finite-element analysis or experimental testing. One phase (phase *a*) of the machine is connected to an AC current source and the other two phases (*b* and *c*) are open-circuited while the machine is stationary. If the rotor *d*- or *q*-axis is aligned with the phase *a* axis, then the other two phases have the same voltage as the machine is symmetrical. The self (*L*) and mutual (*M*) inductances can be calculated [27] as:

$$L(\theta) = \frac{1}{2\pi f}\sqrt{\left(\frac{V_a(\theta)}{I_a(\theta)}\right)^2 - R_s^2}$$
$$M_{ab}(\theta) = \frac{V_b(\theta)}{2\pi f I_a(\theta)} \tag{3.1}$$

where I_a is the *a*-phase current, V_a and V_b are the *a*- and *b*- phase voltages, f is the frequency of the applied AC current, and θ is the rotor angle. Then the rotor is rotated gradually and the entire process is repeated again for the new angle until the self and mutual inductances for one period are obtained. In the simulation, 2° (mechanical) steps are used and the results are averaged over 10° (mechanical) to take into account the 10° stator skewing.

In general, the self and mutual inductance waveforms can be formulated as:

$$L(\theta) = L_0 + L_1\cos 2\theta \tag{3.2}$$

$$M(\theta) = M_0 + M_1\cos\left(2\theta - \frac{2\pi}{3}\right) \tag{3.3}$$

where θ is the rotor angle, L_0 and M_0 are the dc components and L_1, M_1 are the amplitudes of the lowest harmonic of the inductance variation. The voltages of the three phases can be calculated as follows:

$$\begin{bmatrix} v_a(t) \\ v_b(t) \\ v_c(t) \end{bmatrix} = \begin{bmatrix} e_a(t) \\ e_b(t) \\ e_c(t) \end{bmatrix} - \frac{d}{dt}\left\{ \boldsymbol{L}(\theta) \begin{bmatrix} i_a(t) \\ i_b(t) \\ i_c(t) \end{bmatrix} \right\} - R_s \begin{bmatrix} i_a(t) \\ i_b(t) \\ i_c(t) \end{bmatrix} \tag{3.4}$$

where the inductance matrix L is a function of rotor angle and hence time and is given by:

$$\begin{bmatrix} L_0 + L_1\cos(2\theta) & -M_0 - M_1\cos(2\theta - 2\pi/3) & -M_0 - M_1\cos(2\theta + 2\pi/3) \\ -M_0 - M_1\cos(2\theta - 2\pi/3) & L_0 + L_1\cos(2\theta + 2\pi/3) & -M_0 - M_1\cos(2\theta) \\ -M_0 - M_1\cos(2\theta + 2\pi/3) & -M_0 - M_1\cos(2\theta) & L_0 + L_1\cos(2\theta - 2\pi/3) \end{bmatrix} \tag{3.5}$$

Transforming (3.4) and (3.5) to the *d-q* reference frame allows the *d-q* inductances to be found as:

$$\begin{aligned} L_q &= L_0 + M_0 + (0.5L_1 + M_1) \\ L_d &= L_0 + M_0 - (0.5L_1 + M_1) \end{aligned} \tag{3.6}$$

This result is useful for analyzing balanced 3-ph operation of the generator but less useful for unbalanced operation such a single-phase operation where the *d-q* currents and voltages are not constant with time.

For simplicity and to gain insights from the analytical results, the inductance variation with rotor position will be neglected. Thus the machine is effectively analyzed as a non-salient surface PM machine. The validity of this assumption will be demonstrated later by close correspondence between the analytical results against the FE simulation results. The small effect of the saliency is not surprising given the presence of large amounts of rare-earth magnets in the machine.

With the above assumption, the inductance matrix is no longer a function of rotor position, and so (3.4) and (3.5) can be written in phasor notation as:

$$\begin{bmatrix} \mathbf{V_a} \\ \mathbf{V_b} \\ \mathbf{V_c} \end{bmatrix} = \begin{bmatrix} \mathbf{E_a} \\ \mathbf{E_b} \\ \mathbf{E_c} \end{bmatrix} - j\omega \begin{bmatrix} L_0 & -M_0 & -M_0 \\ -M_0 & L_0 & -M_0 \\ -M_0 & -M_0 & L_0 \end{bmatrix} \begin{bmatrix} \mathbf{I_a} \\ \mathbf{I_b} \\ \mathbf{I_c} \end{bmatrix} - R_s \begin{bmatrix} \mathbf{I_a} \\ \mathbf{I_b} \\ \mathbf{I_c} \end{bmatrix} \tag{3.7}$$

From (3.7) it can be shown for balanced 3ph current phasors $\mathbf{I_a}$, $\mathbf{I_b}$ and $\mathbf{I_c}$ that:

$$\begin{bmatrix}\mathbf{V_a}\\ \mathbf{V_b}\\ \mathbf{V_c}\end{bmatrix} = \begin{bmatrix}\mathbf{E_a}\\ \mathbf{E_b}\\ \mathbf{E_c}\end{bmatrix} - j\omega \begin{bmatrix}(L_0 + M_0)\mathbf{I_a}\\ (L_0 + M_0)\mathbf{I_b}\\ (L_0 + M_0)\mathbf{I_c}\end{bmatrix} - R_s \begin{bmatrix}\mathbf{I_a}\\ \mathbf{I_b}\\ \mathbf{I_c}\end{bmatrix} \tag{3.8}$$

which results in the expected balanced output voltages. For the single-phase star-connected operation with $I_b = I_c = 0$, equation (3.7) simplifies to

$$\begin{bmatrix}\mathbf{V_a}\\ \mathbf{V_b}\\ \mathbf{V_c}\end{bmatrix} = \begin{bmatrix}\mathbf{E_a}\\ \mathbf{E_b}\\ \mathbf{E_c}\end{bmatrix} - j\omega \begin{bmatrix}(L_0)\mathbf{I_a}\\ (-M_0)\mathbf{I_a}\\ (-M_0)\mathbf{I_a}\end{bmatrix} - R_s \begin{bmatrix}\mathbf{I_a}\\ 0\\ 0\end{bmatrix} \tag{3.9}$$

where the reactance seen by the *a*-phase current is reduced from ($L_0 + M_0$) to (L_0). It also shows that while the *b*- and *c*-phase currents are zero, the *b*- and *c*-phase voltages are affected by the *a*-phase current through the mutual inductance term M_0. The load current $I_L = I_a$.

Table 3.1 summarizes the constraints set by the connection arrangement and the output voltage and current for the three 1-ph connections. The analytical results use the FE calculated values of inductances.

Table 3.1 Arrangement Constraints and Outputs

Connection	Constraints	Output	
		Voltage	Current
1ph star	$\mathbf{I_b} = 0;\ \mathbf{I_c} = 0$	$\mathbf{V_a}$	$\mathbf{I_a}$
1ph delta	$\mathbf{I_b} = \mathbf{I_c};$ $\mathbf{V_a} = -\mathbf{V_b} - \mathbf{V_c}$	$\mathbf{V_a}$	$\mathbf{I_a} - \mathbf{I_b}$
1ph open delta	$\mathbf{I_a} = -\mathbf{I_b} = \mathbf{I_c}$	$\mathbf{V_a} - \mathbf{V_b} + \mathbf{V_c}$	$\mathbf{I_a}$

The results from equations (3.8) and (3.9) are illustrated in Fig. 3.2. This compares the 3-phase phasor diagram under balanced 3-ph resistive load operation (black lines) with an unbalanced condition with a single-phase resistive load connected to the *a*-phase and the other phases open-circuited (red lines). The 3-ph back-emf voltages E_{abc} are balanced. With a balanced 3-ph load, the currents I_{abc} and hence the terminal voltages V_{abc} are also balanced. With the single-phase load, the voltage drop of the loaded phase is less than that in the 3-ph case. For the two open-circuited phases, the *b* phase has a voltage which falls with increasing load current, while the *c* phase actually increases with increasing load current. This is due to the phase angle of the induced voltage due to mutual inductance, with respect to the back-emf voltage in each phase, see (3.9).

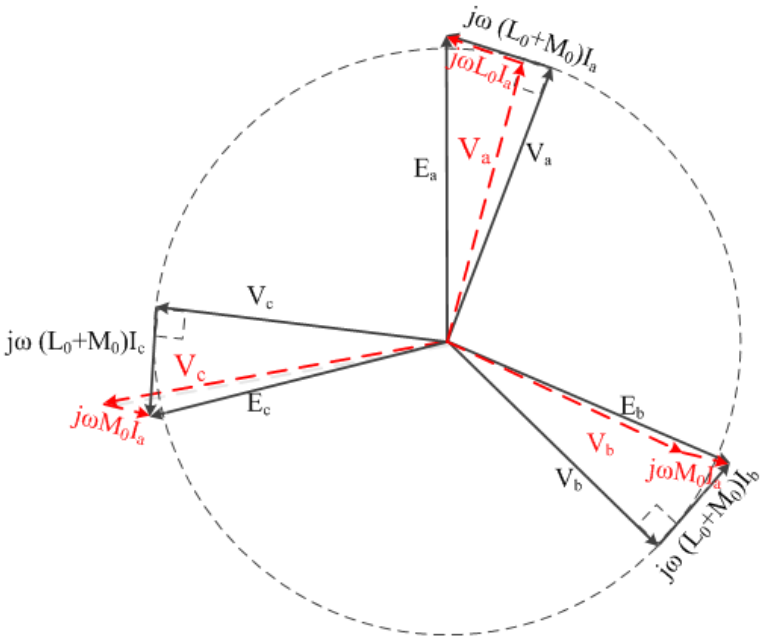

Figure 3.2 Phasor diagrams for balanced 3-phase (black lines) and single phase resistive loading (red lines).

3.3.1 End-Winding Leakage Inductance

The effect of the end-winding leakage inductances is not considered in the 2D FE analysis. These inductances can be estimated using the empirical formula given in [28]:

$$L_{end} = \frac{4m}{Q} q N^2 \mu_0 l_{end} \lambda_{end} \tag{3.10}$$

where m is the number of phases, Q the number of slots, q the number of slots per pole per phase, N the winding turns, μ_0 the permeability of vacuum, l_{end} the average length of the end winding and λ_{end} the end winding permeance factor.

3.4 Simulation and Experimental Results

3.4.1 Mutual Inductance

Fig. 3.3 compares the FE simulations with a linear stator steel (dashed lines) and a saturating stator (solid lines), and the measured (symbols) self and mutual inductance versus rotor position. The FE calculated self-inductance curves do not include the analytically calculated end-winding leakage inductance of approximately 0.67 mH. The inductance measurement method used was described earlier.

The average (saturating) mutual coupling is about one-third of the average self-inductance. The effect of skewing is considered by averaging the finite-element calculated inductance results over one slot width (10° mechanical).

While the agreement between the measured and calculated results is generally good, it may be initially surprising that the 2D FE calculated inductance curves with the saturating stator are slightly higher than the experimental results. This is also given that the FE calculated self-inductance curve does not include the 0.67 mH analytical calculated end-winding inductance.

To investigate this discrepancy, the FE calculated inductance curves with a linear (non-saturating) stator steel are also included. Given the high degree of saturation present in the stator of the machine as described in chapter 2, it was not unexpected to find that stator saturation causes a significant reduction (shift) of the entire self-inductance waveform and also reduces the minimum value of the mutual inductance. It is thus likely that inaccuracies in the modelling of the stator saturation, perhaps also related to 3D magnet fringing effects which will increase stator saturation, may be the cause of the experimental results being slightly lower than the calculated results. Table 3.2 compares the measured and the saturating FE calculated self and mutual inductances. It also includes the armature winding inductance which is the sum of self and mutual inductances and shows a 6% higher calculated value.

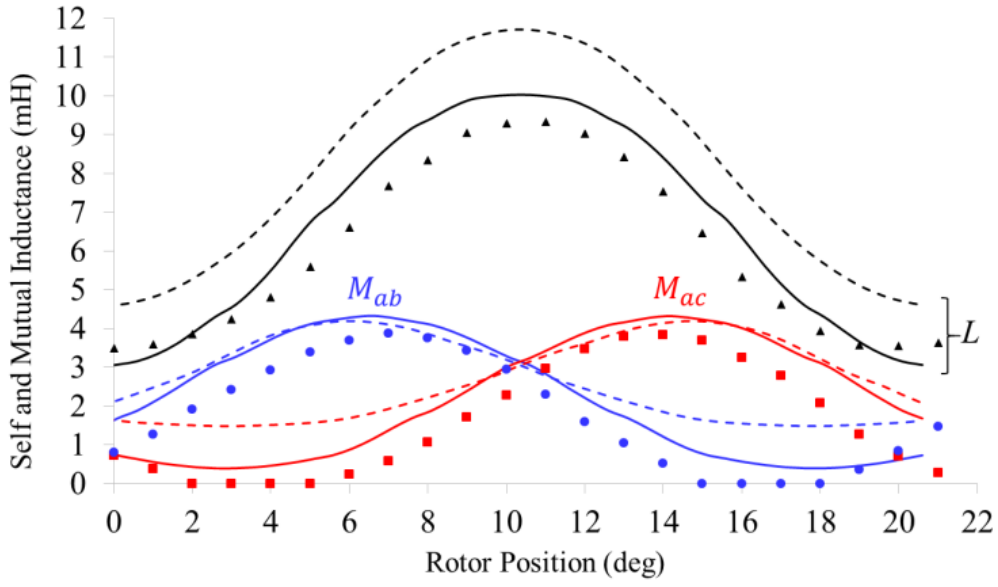

Figure 3.3 FE simulation with a linear stator (dashed lines) and a saturating stator (solid lines) and measured values (symbols) of the self and mutual inductances as a function of rotor position in mechanical degrees.

Table 3.2 Self and Mutual Inductance.

	FE	**Measured**
L_0	6.03mH	6.00mH
M_0	2.10mH	1.67mH
L_1	2.37mH	3.16mH
M_1	1.38mH	2.04mH
Armature Winding Inductance $L_0 + M_0$	8.13mH	7.67mH

3.4.2 Voltage Regulation

Fig. 3.4(a) compares the voltage regulation of the star-connected IPMG with a single-phase resistive load connected to phase *a* (shown in red). The measured, FE and analytically calculated results are shown as symbols, and as solid and dashed lines, respectively. The dashed vertical line indicates the rated single-phase load. As the three-phase machine is rated at 16 kW, the rated single-phase load is about 5.3 kW.

The FE results for phases *b* and *c* show higher (absolute) voltage regulation compared to the measured results. This is likely due to the higher value of the FE calculated average mutual inductance compared to the measured value. Given the FE and measured average self-inductances are similar, it would be expected that the FE and measured voltage regulation for phase *a* should match better, which was correct. At the rated load, the measured voltage regulation is about 4.4% which is only 0.4% more than the simulated result.

The slightly higher measured than simulated phase *a* voltage regulation could be associated with stator resistance changes due to temperature. To investigate this, the FE simulation was repeated for different values of stator resistance. Fig. 3.4(b) shows the voltage regulation with the measured value of stator resistance 0.27 Ω at 20°C, and also values of 0 Ω, 0.3 Ω (corresponding to a 30°C temperature rise) and 0.4 Ω (corresponding to a 120°C temperature rise). As expected from (3.9), the voltage regulation of the unloaded phases are unaffected by the stator resistance changes as there is no current in these phases. However, the voltage regulation for phase *a* at rated load varies from 1% to 5.5% over the stator resistance range considered. In particular, even a 30°C stator temperature rise corresponds to the difference between the measured and FE voltage regulation results. It is worth mentioning that although increasing the rotor temperature and consequently reducing the permanent magnet remanent flux

density drops the output voltage magnitude; it does not affect the voltage regulation as this is defined as the ratio of voltage drop to the open-circuit value.

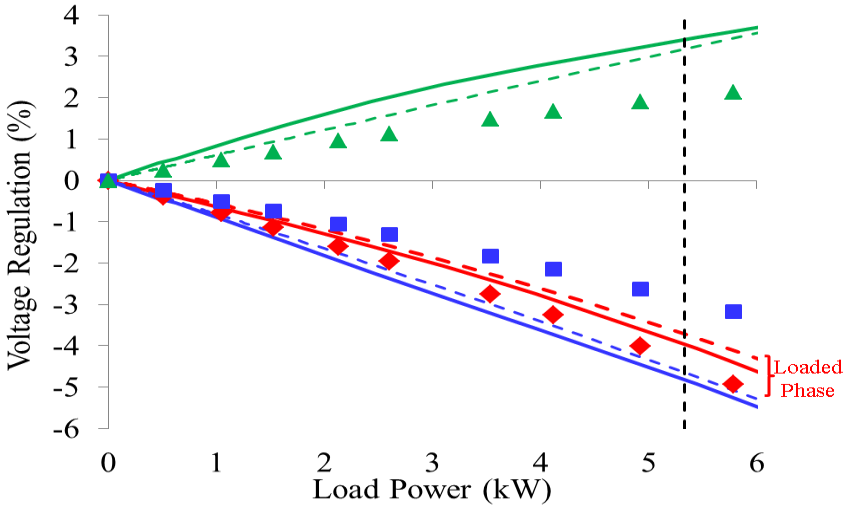

(a)

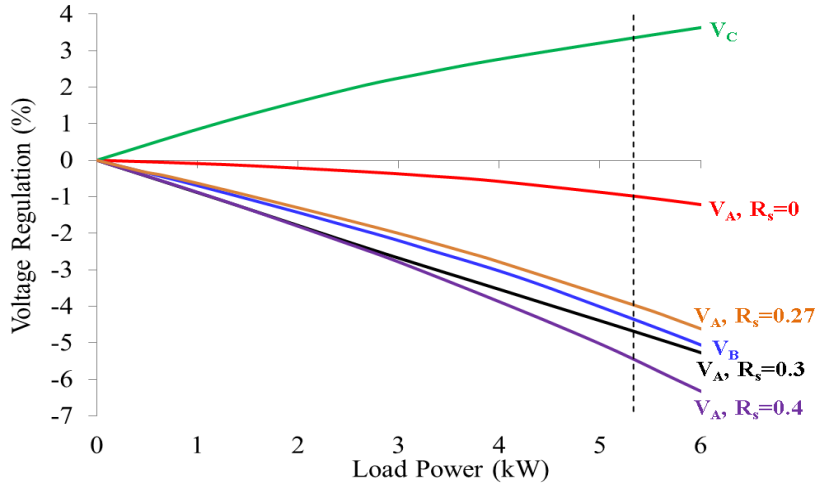

(b)

Figure 3.4 Single-phase load with star winding connection, (a) measured (symbols), FE simulated (solid lines), analytically calculated (dashed lines) voltage regulation, (b) effect of stator resistance on the voltage regulation using FE.

Fig. 3.5 compares the voltage regulation under single phase loading when the windings are connected in delta. The FE results shows 1% lower, comparable, and 2% higher voltage regulation for phases *a*, *b*, and *c*, respectively compared to the measured data. The analytical results are in acceptable agreement with the simulation and measured ones.

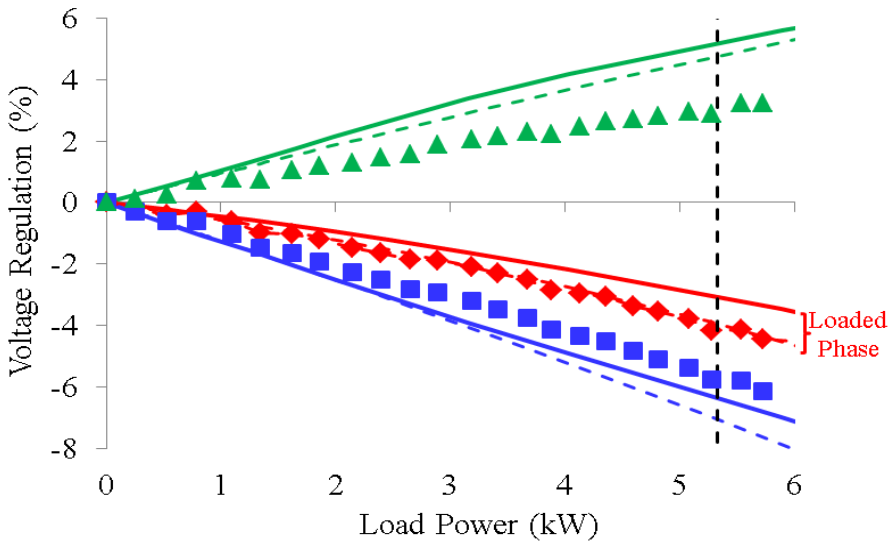

Figure 3.5 Voltage regulation under single-phase loading using delta winding connection. measured (symbols), FE simulated (solid lines), and analytically calculated (dashed lines).

Fig. 3.6 compares the effect of different winding configurations on the voltage regulation of the loaded phase and also 3-phase loading. To eliminate the effect of increased resistance due to temperature rise only the FE results are presented. The 3-phase loading had the highest calculated voltage regulation of 5.5% at the rated load. Single phase star and open-delta connections both had about 4% voltage regulation. The delta connection had the lowest voltage regulation of 3%.

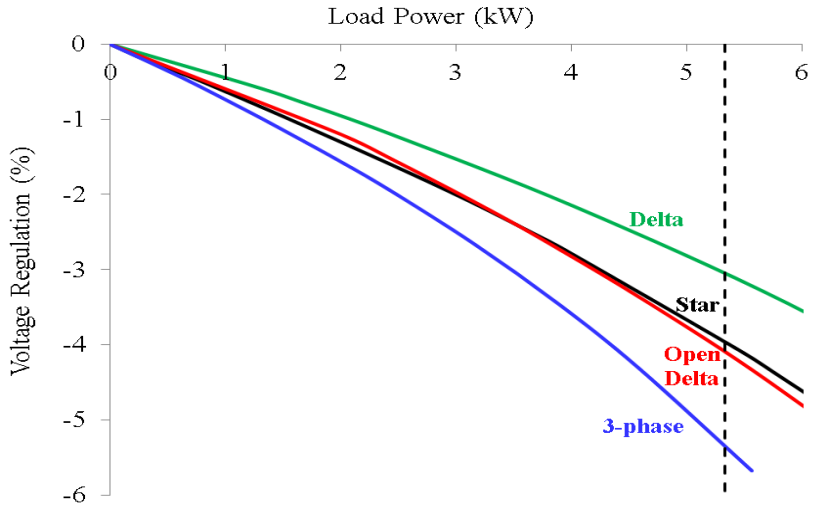

Figure 3.6 FE simulated voltage regulation versus load power for various winding configurations. The 3-ph results are plotted against output power per phase.

To explain the above results it is useful to consider the phase impedance of each winding connection. For the 1-ph star connection the equivalent circuit includes a 1pu voltage source and series impedance which will be defined as 1pu. For the 1-ph delta

connection, the impedance is effectively one phase in parallel with two series phases resulting in a total impedance of 2/3 pu and a 1.5 pu current capability. This results in improved voltage regulation at 1pu current.

For the open delta connection, to a rough approximation, the equivalent circuit includes a 2 pu voltage source and a 3 pu series impedance. If the winding turns are halved, the equivalent circuit would be a 1 pu voltage source and 3/4 pu series impedance with a 2 pu current capability. Thus the voltage regulation at 1 pu current should be comparable to the 1-ph delta however the FE results in Fig. 3.6 show it is more comparable to the star connection. This may be associated with the more complex mutual coupling effects from (3.7) which have been neglected in the very simplified analysis used above.

Finally for the case of the 3-ph star connection, the single-phase equivalent circuit includes a 1 pu voltage source and series impedance which from (3.8) is slightly larger than that for the 1-ph case in (3.9) and hence produces a slightly poorer voltage regulation.

3.4.3 THD

Fig. 3.7 compares the FE calculated with the measured voltage waveforms under open-circuit and rated loading conditions where for 1-ph loading, the resistive load is connected to phase *a* (blue lines).

For the 1-ph star loading (Fig. 3.7(c) and (d)), the loaded waveform shows a distinct asymmetry between the rising and falling edges. The phase *b* waveform has a pronounced flat top and a comparable magnitude to phase *a*, and phase *c* has a sharp peak with a higher magnitude than the other phases.

The delta waveforms (Fig. 3.7(e) and (f)) are more sinusoidal than the star waveforms under open-circuit conditions but particularly under loaded conditions. There is an excellent match between the predicted and measured results. The improved waveforms with delta can be explained by its lower source impedance and the circulating triplen currents which reduce the output voltage triplen harmonics.

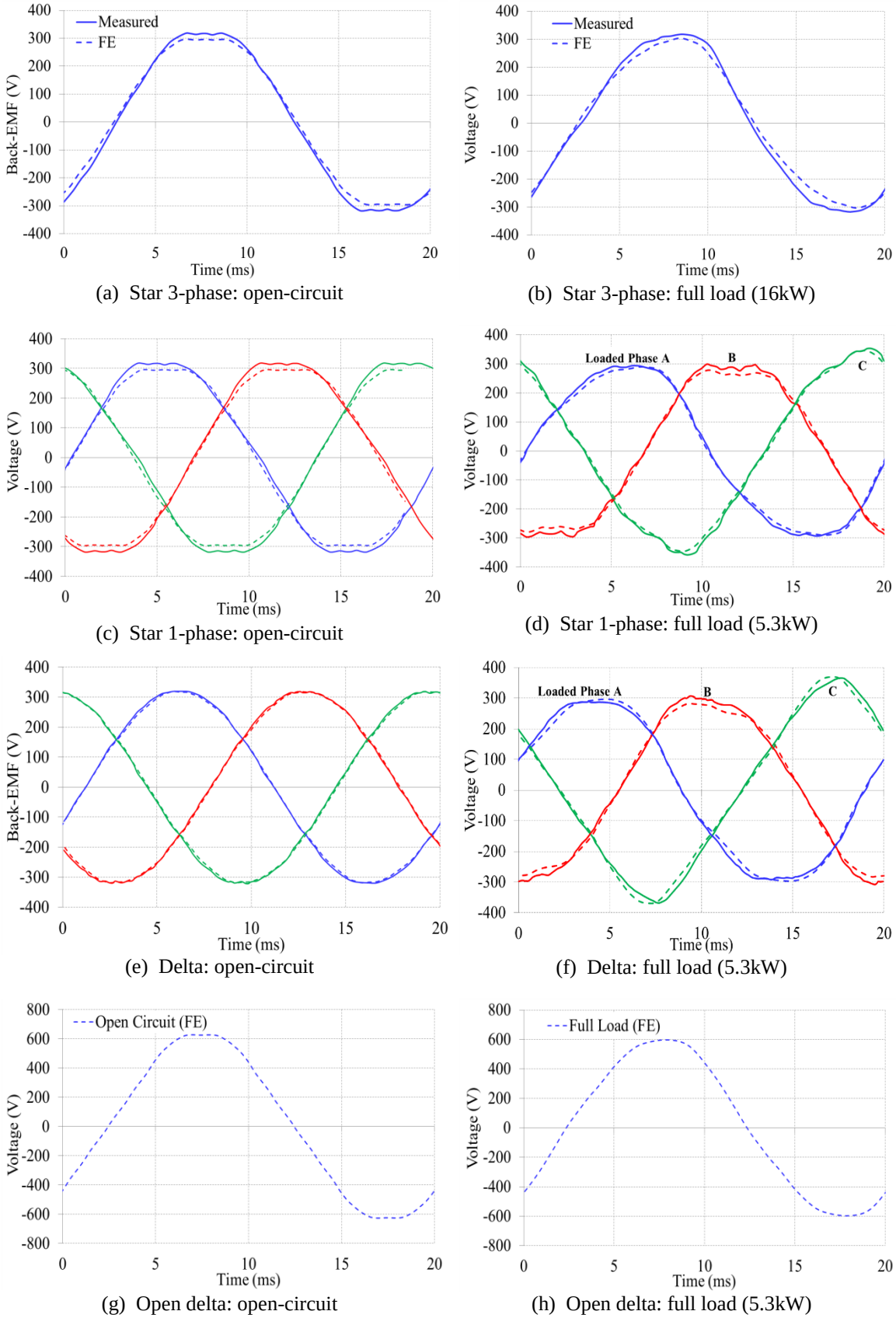

(a) Star 3-phase: open-circuit

(b) Star 3-phase: full load (16kW)

(c) Star 1-phase: open-circuit

(d) Star 1-phase: full load (5.3kW)

(e) Delta: open-circuit

(f) Delta: full load (5.3kW)

(g) Open delta: open-circuit

(h) Open delta: full load (5.3kW)

Figure 3.7 Measured (solid) and FE calculated (dashed) phase voltage waveforms. Note the output voltage for the open-delta configuration is twice that of the other configurations (no experimental results were available for this case).

The quality of the waveforms improves for the open-delta connection (Fig. 3.7(g) and (h)) and the waveforms are similar to the 3-phase loading condition. No measured waveforms are available for the open-delta connection.

Fig. 3.8 compares the measured and FE calculated THD versus load for the four different winding configurations. With the 3-ph star connected load, the no-load line voltage THD is 2.2% which reduces to 1.0% under full load condition, which is the lowest of all the winding configurations. Note as this is for the line voltage it does not include any triplen harmonics.

For single-phase loads, both the delta and star connections show a roughly linear increase in THD with load. The measured star THD results increase from about 4% at no-load to about 8% at full-load while for delta this increases from below 1.5% at no-load to about 5% at full load. The delta connection thus has about 3% lower THD than the star at all load points.

The open-delta connection has the lowest calculated THD for all of the single-phase connections for powers greater than 3 kW. It has a calculated no-load THD of 1%, a maximum THD of 4% and a THD at rated 2-ph output of 2.5%.

In general, the FE calculated THD was in good agreement with measured results especially for the 3-ph and delta connection. For 1-ph star, it over-estimated the THD by up to 1%.

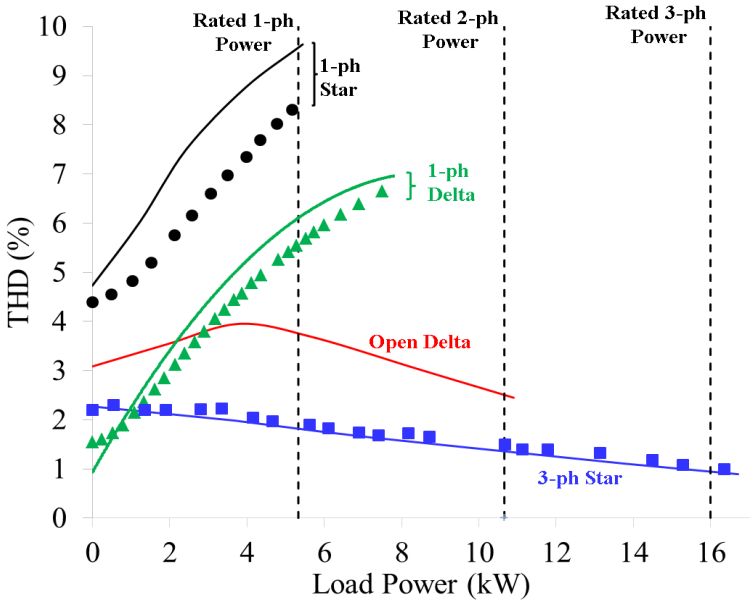

Figure 3.8 Measured (symbols) and FE calculation (lines) comparison of THD for 3-ph and 1-ph loading conditions for the four winding configurations. The 3-ph results are for line voltage THD.

3.4.4 Current, Loss and Efficiency

As was indicated earlier, the maximum output power of the machine is limited by its rated phase current, which is 24.3 A. Fig. 3.9(a) compares the current of the loaded phase versus output power for the four winding configurations.

The results match well with the simple analytical predictions which are for a power level of roughly 33%, 50% and 67% for the star, delta and open-delta connections respectively at rated current.

For the 1-ph delta connection, the 3rd harmonic circulating current results in a non-zero phase current at no-load. The FE calculating circulating current was slightly higher than the measured one (4.9 A versus 3.9 A). This is likely due to inaccuracies in the way that the skewing was modeled. The copper loss associated with the circulating current is indicated as the first point in the Fig. 3.9(b) and is relatively small.

Fig. 3.9 (b) depicts the FE calculated and measured copper loss comparison for the three-phase and single-phase loading at the rated speed. The iron loss is similar for all winding configurations and is approximately 450 W. It reduces slightly with increasing load.

The copper loss is proportional to the square of the output current and hence the output power. For the three-phase loading, the full-load 3-ph copper loss (about 600 W) is comparable to the iron loss which is normal for a well-designed machine.

For the 1-ph delta connection, the total copper losses are slightly higher than the star connection due to the losses in the parallel phases and the circulating current losses. The open-delta connection ideally has the same rated copper loss as the 3-ph star connection at 2/3rd of its output power (2-ph rated power). As copper loss is proportional to the square of output power, this means that at the 1-ph rated power, its copper loss will ideally be 25% of the 3-ph rated value. This is in comparison to the 1-ph star connection which ideally has 33% of the 3-ph rated copper loss at this power.

Overall, there is a good agreement between the measured and simulated results.

Fig. 3.9(c) depicts the efficiency of the IPMG. For the 3-phase case, the FE results indicate that the machine has an efficiency of 94% under the rated condition. The FE

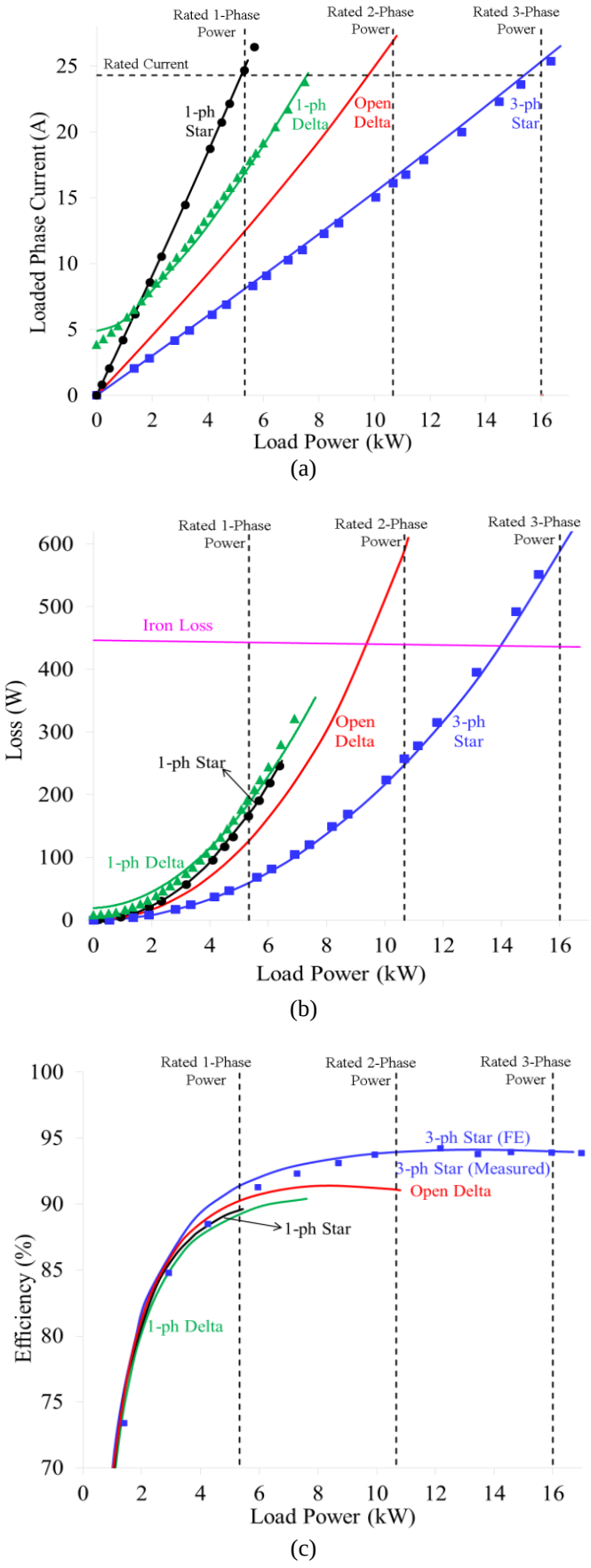

Figure 3.9 Measured (symbols) and FE calculation (lines) comparison of 1-ph and 3-ph loading conditions using various winding configurations. (a) loaded phase current, (b) copper loss, and (c) efficiency.

and measured results are in good agreement and the small difference between the results is likely due to neglecting mechanical losses in the simulation.

For the single-phase star connection at rated 1-ph output (5.3 kW), the machine has a calculated efficiency of about 89%. The delta connection had a 0.4% lower efficiency than the star connection under this condition. The open-delta connection has the efficiency of roughly mid-way between the 1-ph and 3-ph star connections.

If it is assumed for the 3-ph machine that the rated copper and iron losses are equal, then for rated 1-ph operation, the copper loss will be 1/3 of the copper loss of the 3-ph machine resulting in a total loss of 2/3 of the 3-ph machine. As the output power is only 1/3 of the 3-ph machine, the ratio of the losses to the output power is roughly twice. Hence the studied machine which has a rated 3-ph efficiency of 94% (about 6% loss) would have a 1-ph efficiency of roughly 88% (about 12% loss) which corresponds well to the predictions of efficiencies between 88% and 90% for the three connections. These efficiencies are slightly higher than that given by the simple approximation as the rated copper loss is slightly higher than the rated iron loss for the machine considered.

Experimental efficiency results for the three-phase operation were obtained using the torque measurement arrangement shown in Fig. 2.3. Torque measurements and hence efficiency results are not available for the 1-ph connections due to concerns about damage to the torque transducer caused by the high pulsating torque under this condition.

Table 3.3 summarizes the voltage regulation, THD, and efficiency of this machine under balanced 3-ph and 1-ph operation for the studied winding connections.

Table 3.3 Comparison of 3-ph and 1-ph Connection Types. Measured values with calculated values in brackets.

	Rated Power	Voltage Regulation	Rated THD	Efficiency
3-ph star	3-ph	5.0% (5.4%)	1.0% (1.0%)	94% (94%)
1-ph star	1-ph	4.4% (4.0%)	8.2% (9.6%)	(89.1%)
1-ph delta	1-ph	4.0% (3.2%)	5.6% (6.0%)	(88.7%)
open-delta				
1-ph rated	1-ph	(4.1%)	(3.8%)	(90.1%)
2-ph rated	2-ph	(11.8%)	(2.5%)	(91.1%)

Fig. 3.10 depicts the FE calculated instantaneous input torque at the rated output power under both three-phase and single-phase loading. The three-phase operation

produces a relatively smooth input torque which only has a small 6th harmonic variation and has an average input torque of 108 Nm. For single-phase loading, there is the expected large second-harmonic torque component. The average of the input torque is approximately one-third of the 3-phase loading case where this value was 8% and 14% higher for the delta and open delta connection, respectively.

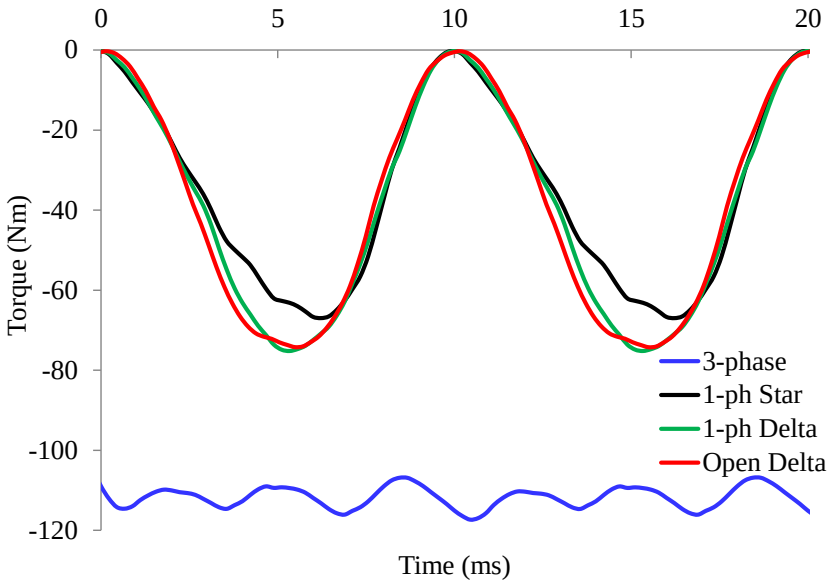

Figure 3.10 FE calculated input torque under 3-ph and 1-ph rated loading conditions.

3.5 Conclusion

This chapter examined the performance of a three-phase, four-pole, 16 kW interior permanent-magnet generator when running single-phase resistive loads. The 3-ph star-connected performance was compared with the performance of three alternative 1-ph connections: 1-ph star, 1-ph delta and a new "open delta" winding configurations. The voltage regulation, total harmonic distortion (THD) and efficiency were examined using analytical calculation, finite element simulation and, where available, experimental results and good agreement between these was generally shown. The key results are as follows:

For 1-ph operation with rated output current, the ratio of losses to output power is roughly twice that for 3-ph operation due to the fixed iron losses and reduced output power. Hence the studied machine which has a rated 3-ph efficiency of 94% has a rated 1-ph efficiency of roughly 88%.

A star-connected winding has the advantage of being able to drive both 3-ph 400 V loads and 1-ph 230 V loads simultaneously. For 1-ph loads the rated output is 33% of

the 3-ph machine. The voltage regulation is better than that with 3-ph operation due to the lack of mutual coupling but the THD is poorer.

A 1-ph delta connection has an output power capability of about 50% of the 3-ph machine due to the paralleled phases contributing to the load current. Compared to the star-connection, its lower source impedance improves the voltage regulation and the circulating currents reduce the output voltage triplen harmonics and result in a lower THD. The triplen circulating current was about 20% of rated current under no-load conditions.

The proposed 1-ph open-delta connection has an output power capability of about 67% of the 3-ph machine. At its maximum output power it offers good calculated performance with regards to THD (3%) and efficiency (91%), but has a poor voltage regulation (12%). In addition, its output voltage is twice the phase voltage and so may require rewinding of the 3-ph machine.

Based on its strong performance at 33% of rated output power and its capability to operate at 67% of rated output power (though with relatively poor voltage regulation), the proposed open-delta connection shows significant promise for driving single-phase loads.

While the machine studied is an IPM machine, the analytical model used is for a surface PM machine and the close correspondence between the FE and analytical results show that saliency has little influence on the performance. It is thus expected that similar conclusions to the above would be obtained for surface PM generators.

Chapter 4 :Motoring Performance of the IPM Machine with Open-Loop Inverter Drive

The performance of the cage-less IPM machine developed for the portable generator application is examined when run as a motor under open-loop volts-per-hertz control from an inverter. The analytical and experimental steady-state results show the machine can operate with high power-factor and efficiency. The dynamic results show robust operation in starting and the capability to maintain synchronism even with large step load transients. The motor performance is promising for applications requiring high efficiency, particularly where variable-speed operation is needed or where multiple motors can be run from the same inverter.

4.1 Introduction

Increased demand for high-efficiency motors and drives has led to the consideration of permanent-magnet (PM) machines to meet the higher efficiency standards [29]. PM machines are normally driven from an inverter drive. While such a drive can allow further improvement in efficiency by optimizing the motor speed, the inverter adds substantially to the system cost restricting its use in cost-sensitive applications. The use of an inverter can be avoided by adding an induction motor cage to the PM machine to produce a line-start PM machine [30].

Line-start PM machines start as an induction motor. During starting they have two torque components: the cage torque and opposing PM torque (braking torque). At low speeds, the current in the stator and rotor cage are high and the current frequency of the rotor is almost equal to the synchronous frequency. During the acceleration stage, a pulsating torque is injected into the average resultant torque. If the resultant torque is enough to overcome the braking torque, the rotor locks on to synchronous speed. At synchronous speed, the rotor has no eddy currents except those associated harmonic fields [30-33]. The use of line-start motors generally involves a trade-off between the starting and steady-state performance of the machine.

To reduce the system cost, it is possible to operate multiple motors from the same inverter if the loads have largely steady-state operation. This requires the motors to operate stably under open-loop operation without rotor position feedback.

The concept of operating PM machines under open-loop operation from inverters is not new. Generally such machines also include a cage winding to provide damping to the rotor however there has been some work on machines without rotor cages. For instance Mellor et al. [34] investigated the stability of a cage-less rare-earth interior PM motor with a variable-speed drive operating under open-loop control conditions. Possible operating issues with this type of drive are instability at high loads, low power-factor operation, and low efficiency at light loads.

Another consideration in the open-loop operation of PM machines is the possibility of large currents during transient operation producing the risk of demagnetization, especially at extreme temperatures [35]. This is less of a risk in interior PM machines compared to surface PM machines as the magnets are buried in the rotor and so are partially shielded from airgap flux density variations and thus see more uniform magnetic fields. The risk of demagnetization is affected by the magnet thickness, air-gap

length and the magnitude and phase of the stator currents [36]. As the stator current increases, demagnetization occurs first at particular points in the magnet (local demagnetization) before occurring over the bulk of the magnet (global). In [37-39], local irreversible demagnetization for various rotor types and PM shape has been studied.

This chapter considers the application of a spoke-type, cage-less IPM machine as a motor which is driven by an open-loop volts-per-hertz controlled inverter. The steady-state and transient performance characteristics of the machine are examined.

4.2 Analysis of Motoring Performance

Fig. 4.1 shows the equivalent circuit used to simulate the generator under steady-state operation. The inverter is represented by a voltage source *V*, and the motor by an induced voltage source *E*, resistance *R* and reactance *X*. A phasor diagram is also shown and from this the following *dq*-axis equations can be obtained:

$$V_d = I_d R - I_q X \ , \qquad V_q = E + I_d X + I_q R \tag{4.1}$$

$$V_d = \sqrt{I_d^2 + I_q^2} \quad and \quad I_q = \frac{P}{E} \quad V_d = \sqrt{I_d^2 + I_q^2} \quad and \quad I_q = \frac{P}{E} \tag{4.2}$$

$$PF = \cos\left[\tan^{-1}\left(I_q / I_d\right) - \tan^{-1}\left(V_q / V_d\right)\right] \tag{4.3}$$

Consider operation at rated speed, with the induced voltage *E* as the base voltage, thus *E* = 1 pu. For the 16 kW considered machine, the short-circuit current I_{SC}, is roughly five times the rated current. Using the rated current as the base current, thus the short-circuit current is about 5 pu. The stator resistance *R* is relatively small (0.032 pu). Neglecting the stator resistance, gives the reactance $X = E/I_{SC} = 0.2$ pu.

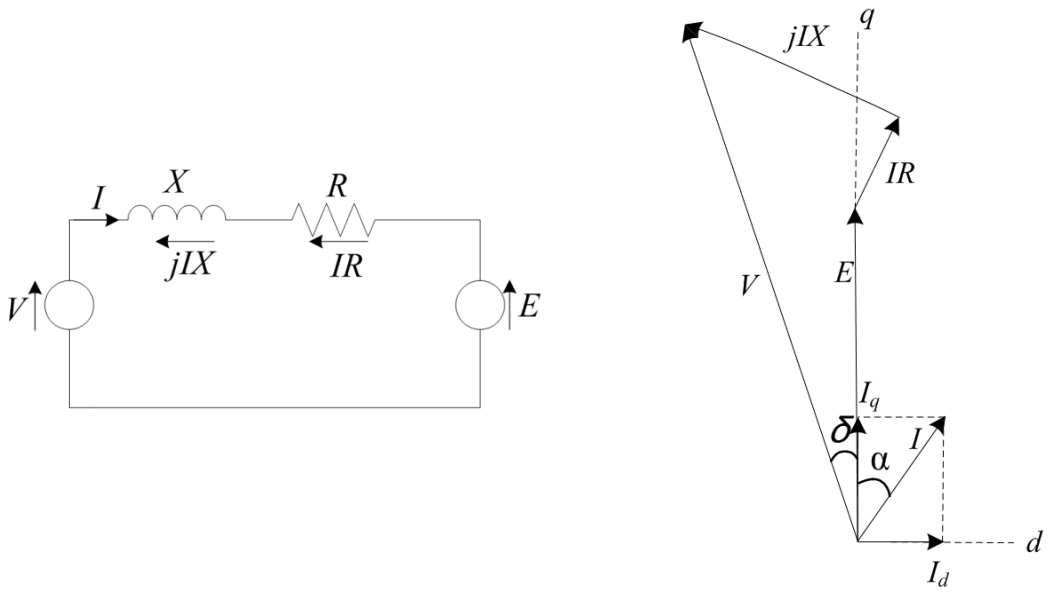

Figure 4.1 Equivalent circuit and example phasor diagram assuming a non-salient machine.

Figs. 4.2 and 4.3 show the calculated performance based on solving (4.1) to (4.3) with E = 1 pu, R = 0 pu and X = 0.2 pu. Fig. 4.2 shows the effect of varying the terminal voltage V by ±10% of its rated value on the stator current and power-factor for output powers of 0.1, 0.5 and 1 pu when the machine is operating at rated speed. These are similar to the classic "V" curves for synchronous machines where the induced voltage E is varied by the changing the field excitation and the terminal voltage is assumed constant while in this case the induced voltage is constant and the terminal voltage is being varied. Fig. 4.2 shows that with the terminal voltage less than 1 pu, the machine has a leading power-factor where the current is reduced by increasing the voltage. This effect is more pronounced for lower power. By increasing the terminal voltage, the machine starts to have a lagging power-factor where the stator current increases with higher rates for the lower power range. For the 1 pu loads, the change in the current with the voltage is not that noticeable (see also Fig. 4.3). The similar trend was repeated for the power-factor variation versus increasing the terminal voltage where the power has a drastic effect on the power factor for lighter loads.

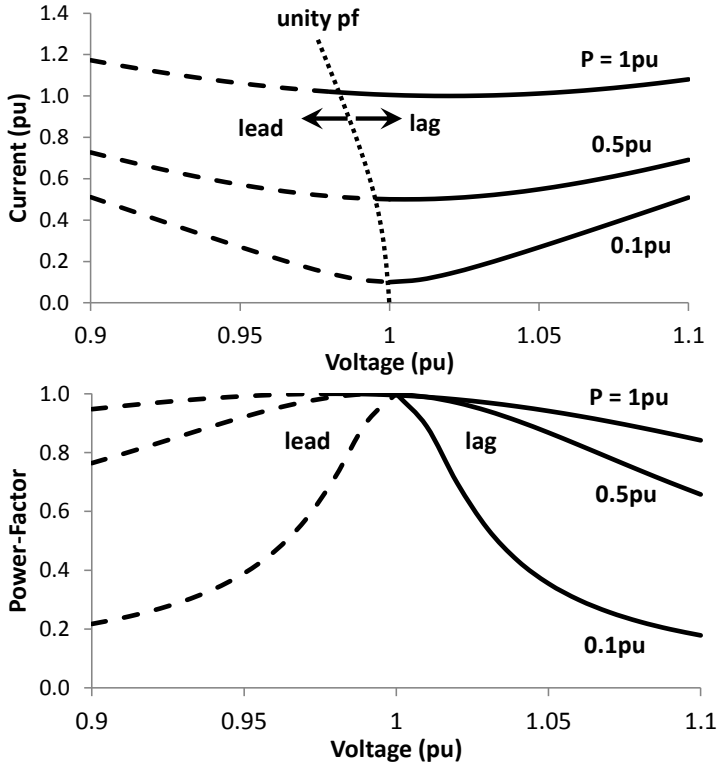

Figure 4.2 Calculated stator current and power-factor as a function of terminal voltage for output powers of 0.1, 0.5 and 1 pu at rated speed. Leading operation is shown with a dashed line. Stator resistance is neglected and X = 0.2 pu.

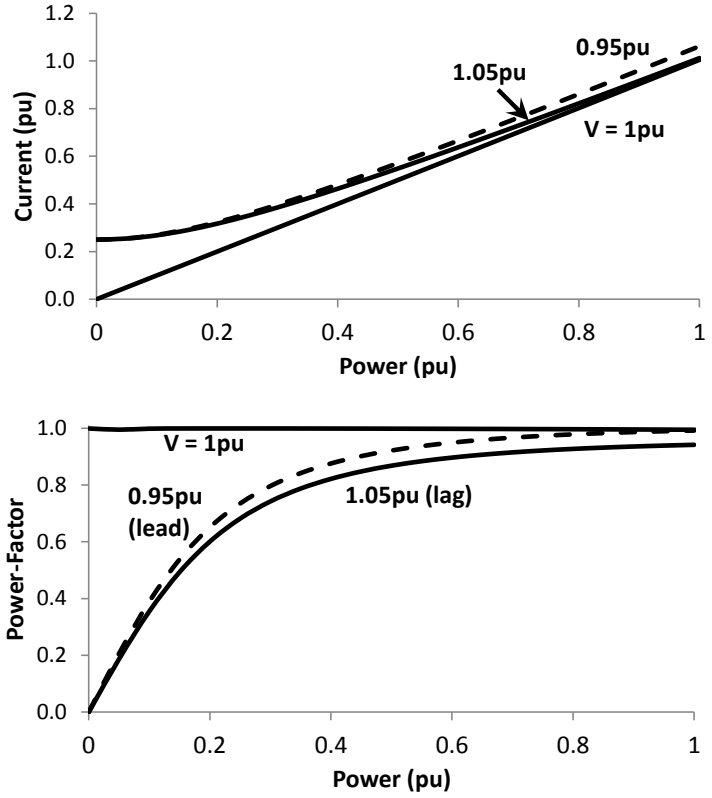

Figure 4.3 Calculated stator current and power-factor as a function of output power for terminal voltages of 0.95, 1 and 1.05 pu at rated speed. Leading operation is shown with a dashed line. Stator resistance is neglected and X = 0.2 pu.

4.3 Finite-Element Demagnetisation Analysis

Fig. 4.4 shows an example of a typical magnetic flux density versus magnetic field strength (BH) plot for a permanent magnet showing the definitions of load line and recoil line. It is noted that sintered NdFeB magnets were used in the fabrication of this machine. With zero magnetic field strength (H = 0), the magnet operates at its remanent flux density B_r. As the magnetic field strength increases in a negative direction, the magnet flux density reduces linearly until it reaches the knee point where the magnet flux density drops rapidly and demagnetization occurs. In the linear part of the curve, the operating point returns to the remanence point when the magnetic field strength is reduced to zero. However if the operating point is brought to below the knee point, say at point A, then if the magnetic field strength is reduced to zero, the operating point moves along the recoil line to a lower value of remanent flux density.

The permeance co-efficient is dependent on the design of the magnetic circuit in which the permanent magnet is part of. This permeance co-efficient determines the slope of the load line which passes through the origin. The operating point of the magnet is determined by the intersection of the load line and the magnet BH characteristic.

Minimizing the amount of permanent magnet used in a machine often results in a magnet operating point close to the knee point where the risk of demagnetization is higher.

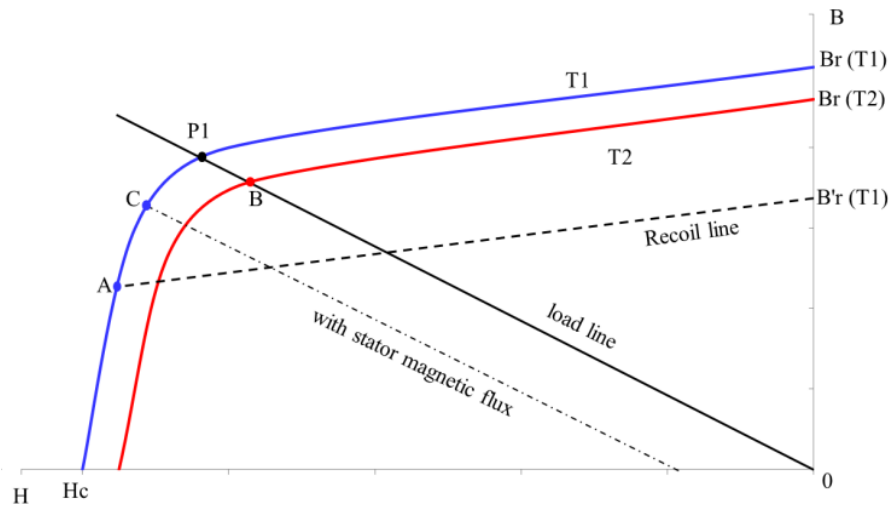

Figure 4.4 BH characteristic of permanent magnets.

Fig. 4.4 illustrates three causes of demagnetization. Firstly, a change in the magnetic circuit such as an increase in the air gap will reduce the permeance co-efficient and hence reduces the slope of the load line and can result in a new operating point below the

knee point. Secondly, a higher magnet operating temperature generally results in a lower magnet BH characteristic and thus lowers the magnet operating point. Thirdly, if the negative *d*-axis stator current is applied, it produces a magnetic field strength which opposes the magnet therefore, the load line shifts to the left and lowers the operating point.

In this machine the air gap length is constant and so the possibility of demagnetization due to stator currents and magnet temperature are studied.

4.3.1 Effect of Stator Current

Fig. 4.5 shows the magnetic flux density contour plots of the two magnets in one pole of the machine when various levels of negative *d*-axis current are applied to the machine assuming a magnet temperature of 50°C. The negative *d*-axis current is increased from zero in the open-circuit condition up to 400 A (peak). For reference, the rated (rms) current of the machine is about 35 A (peak) and the short-circuit current is about 140 A (peak) [40].

Under the open-circuit condition shown in Fig. 4.5(a), the minimum magnetic flux density was 1 T, with the bulk of the magnet being at the average value of 1.17 T. By applying the negative *d*-axis current, the minimum magnetic flux density reduced to 0.35 T, 0.07 T, and below 0 T for the 165 A, 270 A, and 400 A cases, respectively. The plots show that the corners of the magnet are most prone to local demagnetization.

Partial demagnetization reduces the magnet flux density and hence the back-emf voltage. This means the machine needs more current to produce the same amount of torque hence reducing both the torque capability and the efficiency. The reduced efficiency can result in higher magnet operating temperatures making the magnets more prone to further demagnetization.

Beside local demagnetization at the corners of magnets, in the case of sufficiently high currents, there is possibility that the bulk of the magnet can be demagnetized (global demagnetization).

To determine the local and global demagnetization of the magnets, the seven points within the magnet shown in Fig. 4.5(a) are considered.

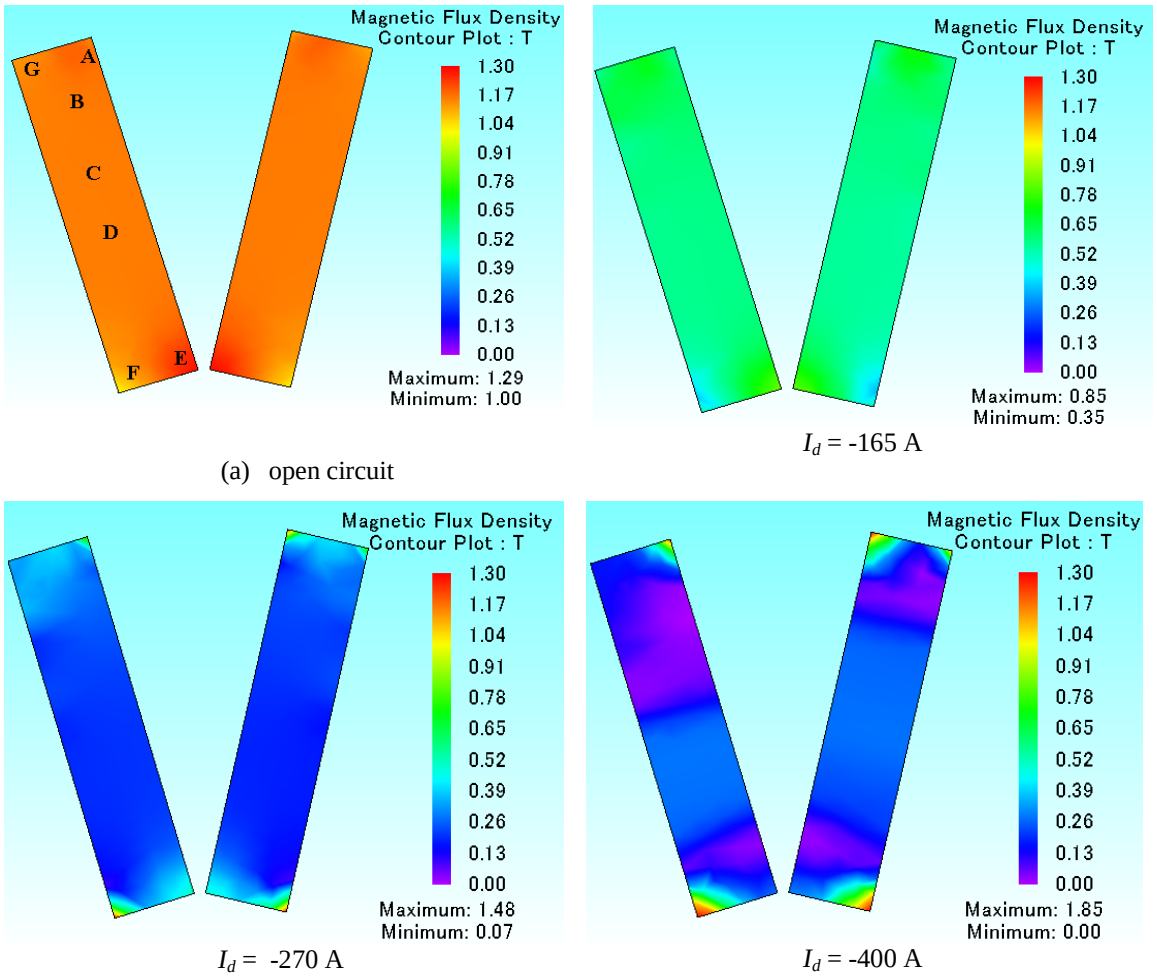

(a) open circuit

I_d = -165 A

I_d = -270 A

I_d = -400 A

Figure 4.5 Calculated magnetic flux density of the magnets at different negative *d*-axis stator currents at 50°C.

Fig. 4.6(a) shows the BH curve of these points with I_d = –400 A plotted for different rotor positions producing a cluster of operating points. The operating points show only a small variation with rotor position.

Point F in the inner corner of the magnet has the highest risk of local demagnetization as it has the lowest operating points. The magnet in this region is effectively completely demagnetized at this value of stator current. Point C which is nearly in the middle of the magnet corresponds to the bulk of the magnet. As its operating point is just below the knee of the curve it appears that global demagnetization has started to occur.

Fig. 4.6(b) shows this machine has high tolerance against the global demagnetization and can tolerate up to 350 A current in the negative *d*-axis. However, the current corresponding to the start of local demagnetization is lower. Fig. 6(c) shows that for the most sensitive corner (point F), the maximum allowable current is 160 A at 50°C. For the higher temperatures, it was shown that the BH points do not lie on the BH curve as

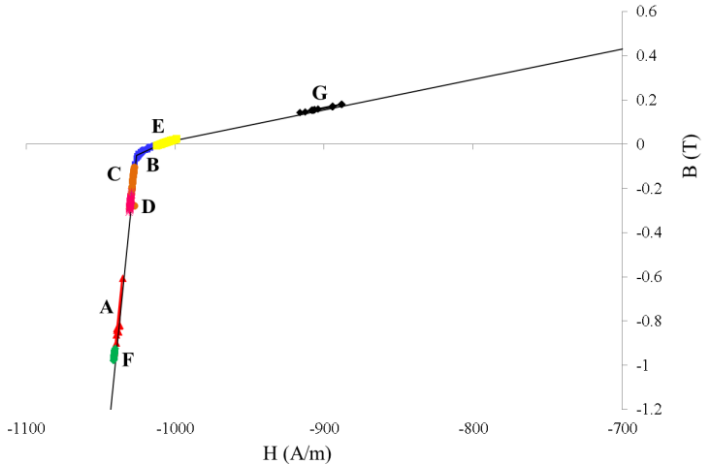

(a) Magnet BH curve showing locus of operating points of the points labeled in Fig. 4.5(a) as a function of rotor position at I_d = -400 A

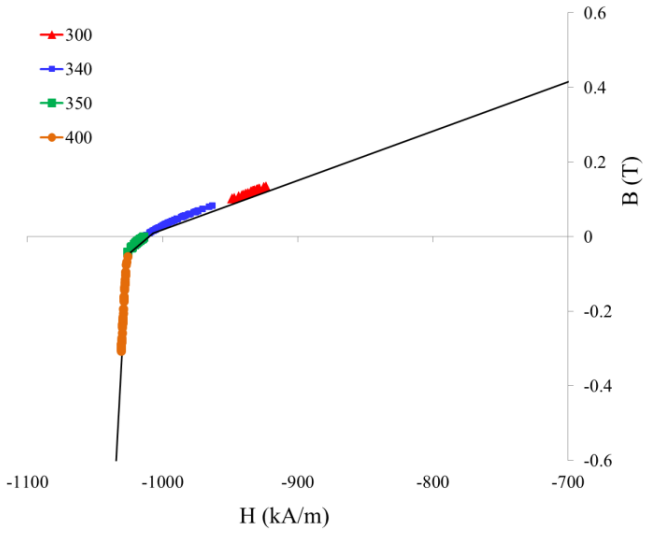

(b) Magnet BH curve showing operating point of point C for different rotor positions at four different values of negative *d*-axis current in amps.

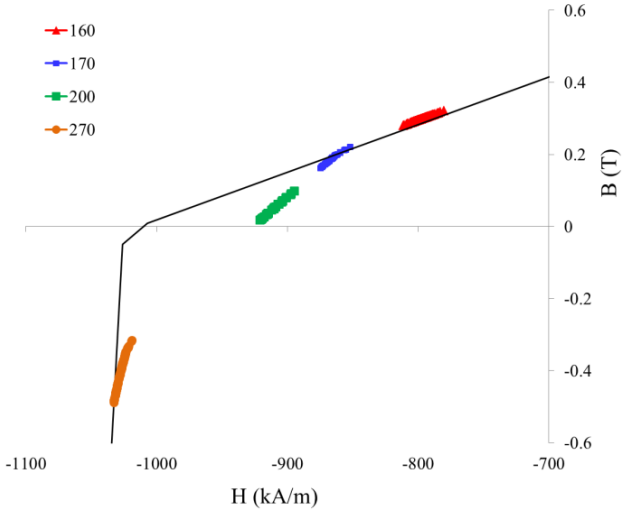

(c) similar to the figure above except it is for point F

Figure 4.6. Calculated variation in magnet operating point as a function of rotor position at 50°C for different locations in the magnet and for different currents.

the magnets start to demagnetize even before the knee points. The high demagnetization withstand capacity is likely due to the combination of the flux-concentrating spoke-type topology and the twin magnets in each rotor pole.

4.3.2 Effect of Magnet Temperature

Fig. 4.7 shows the locations of the magnet operating points on the magnet BH curve for points C and F at a temperature of 80°C. By comparing this figure with Fig. 4.6(b), it can be concluded that the global demagnetization point reduced from about 340 A to about 230 A. The threshold current for local demagnetization falls from about 160 A to about 120 A at the higher temperature.

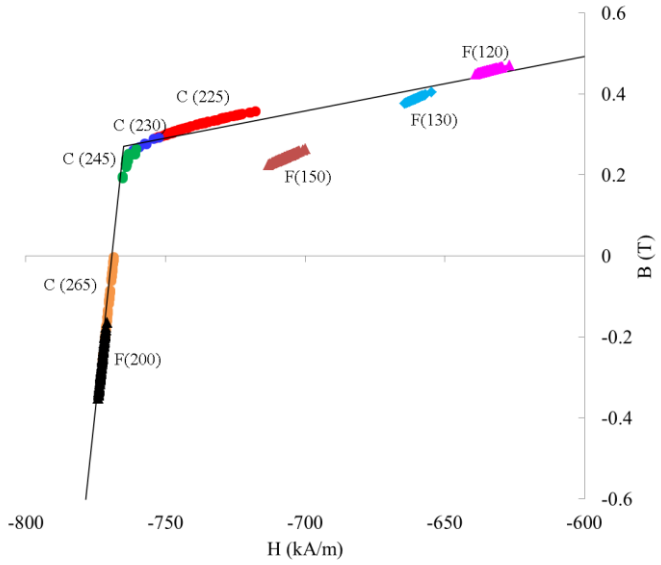

Figure 4.7 Calculated variation in operating points of points C and F at 80°C.

4.4 Experimental Test Arrangement and Results

4.4.1 Experimental Test Arrangement

Fig. 4.8 shows the test arrangement used to perform measurements on the IPM motor. Two identical four-pole 16 kW IPM machines are coupled together using a belt drive. The upper-left machine acts a motor and is connected to the open-loop variable-speed drive, while the lower-right machine acts as generator and is connected to a 3-ph variable resistance load. The motor torque is measured using a reaction torque arrangement on the motor stator. The torque arm and force transducer can be seen in the center of Fig. 4.8(a).

Starting tests were performed with the load machine acting as a generator with the 3-ph resistive load adjusted to produce the specified load at rated speed. As the PM generator's induced voltage is proportional to speed, thus its load current and hence its load torque is proportional to speed. It thus produces a load with a linear torque versus speed curve which corresponds to a square law power versus speed characteristic. Note that constant torque loads have a linear power versus speed characteristic while fan-type loads have a cubic power versus speed characteristic.

The inverter used to drive the motor is shown in the left side of Fig. 4.8(b). Hall-effect current probes are used to measure the current waveforms and a three-phase power analyzer (not shown) is used to measure the electrical input power.

(a) (b)

Figure 4.8. Test set-up. (a) dynamometer configuration, (b) inverter drive with current sensing and interface circuitry.

4.4.2 Steady-State Performance

Fig. 4.9 shows the measured performance of the motor at 1500 rpm with a constant inverter voltage set-point. The measurements include the stator current, input power-factor, input power and losses, and efficiency as a function of output power.

As the motor input power is increased from zero, the measured stator current initially falls and reaches a minimum value of about 9 A at about 4 kW before increasing nearly linearly with increasing load. At light loads, the measured input power-factor is low but increases rapidly to about 0.9 at approximately 8 kW before falling slowly.

The simplified equivalent circuit and equations described in section 4.1, including the effect of stator resistance, was used to predict the motor input current and power-factor as a function of output power. A difficulty encountered was that the power analyzer used was not able to give accurate voltage measurements of the pulse-width modulated inverter waveforms. The simulation results shown in Fig. 4.9(a) and (b) were thus obtained by selecting an inverter voltage which gave the best match to the measured

current and power-factor curves. The good correspondence between the analytical and measured results, particularly at higher power levels, gives confidence in the modelling approach. It is known that the inverter output voltage varies slightly with output current and this could be the reason for the discrepancy between the analytical and experimental results at low currents.

Fig. 4.9(c) compares the measured input electrical and output mechanical power and shows the power losses. Fig. 4.9(d) shows a comparison of the measured efficiency of the machine under both motoring and generating operation. The general shape of the efficiency curves are comparable though below rated output power (shown as vertical line at 16 kW), the machine is more efficient as a generator while above rated output power, the machine is more efficient as a motor. The maximum generating efficiency is about 94% while the maximum motoring efficiency is slightly lower at 93%.

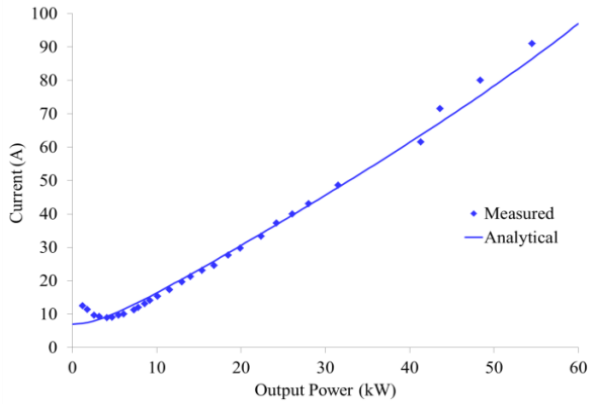

(a) stator current (A_{rms}): measured vs analytical

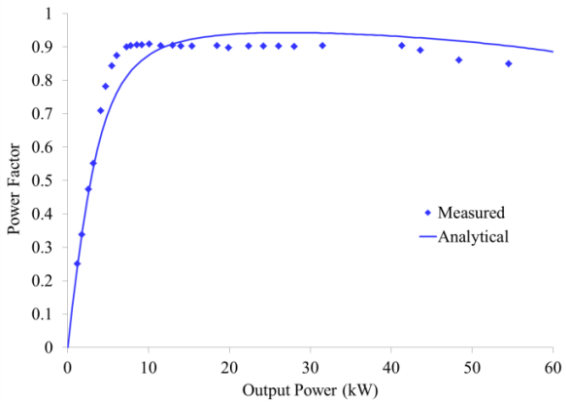

(b) input power factor: measured vs analytical

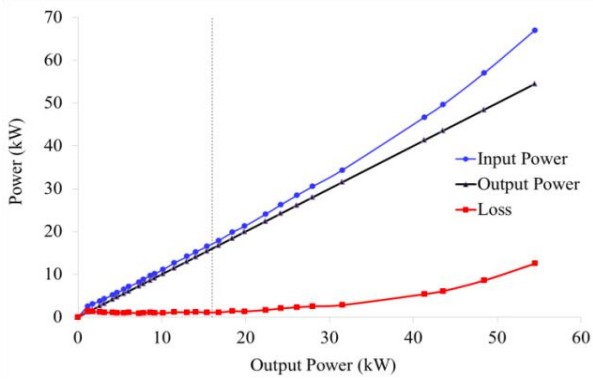

(c) electrical input power, mechanical output power and power loss

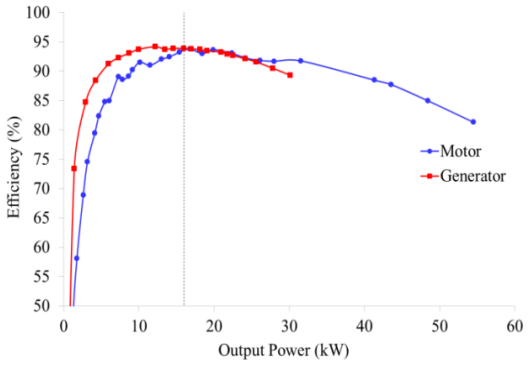

(d) efficiency comparison for motoring and generating operations.

Figure 4.9 Measured results comparison for IPM machine at 1500 rpm.

Fig. 4.9 also shows that the machine is capable of over 50 kW output power (more than three times its rated generator power) under motoring operation. While it is not possible to run at this output power continuously due to the high stator currents (around 80 A_{rms}), this does indicate the machine has a high transient overload capability which is particularly useful in open-loop operation.

4.4.3 Dynamic Performance

Fig. 4.10 shows an example of the measured current transient for the IPM motor as it accelerated from zero to rated speed (1500 rpm). The inverter was programmed to ramp the voltage and frequency from zero to rated voltage/frequency over a period of about 2 s. As described earlier the load torque varied linearly with speed and the load was set to rated power (16 kW) at rated speed. After a short period at rated speed, the machine was decelerated to standstill.

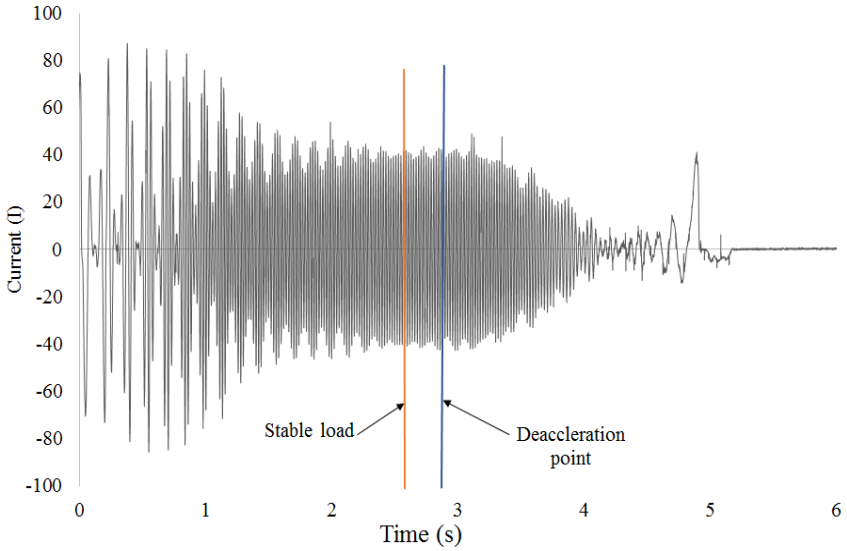

Figure 4.10. Measured starting performance. Motor input current transient when accelerating from zero to rated speed with a 16 kW load, a short time after reaching rated speed, the machine is brought to a standstill.

The machine was also tested starting loads of up to 35 kW (more than twice of rated generating power) with ramp times from 2 s to 9 s. Tests were also done with speed reversals with ramp times of 2 s with loads of up to 35 kW. The motor was found to operate stably and reliably.

Fig. 4.11 shows the transient stator voltage (blue or dark line) and stator current waveforms (brown or light line) when the machine is initially at no-load at rated speed, and a 30kW step load is applied to it. The first cycle of the approximately 5 Hz oscillatory current waveform is shown with a peak current of about 130 A (approximately 4 pu current). Note the significant fall in the stator voltage at the high output power.

The peak observed currents were about 140 A. No issues with demagnetization were observed during the testing. This matches the finite-element analysis results in section 4.3 which indicate with magnet temperatures of 50°C, small amounts of local

demagnetization does not begin until the *d*-axis current reaches about 160 A and global demagnetization does not occur until the current reaches 340 A.

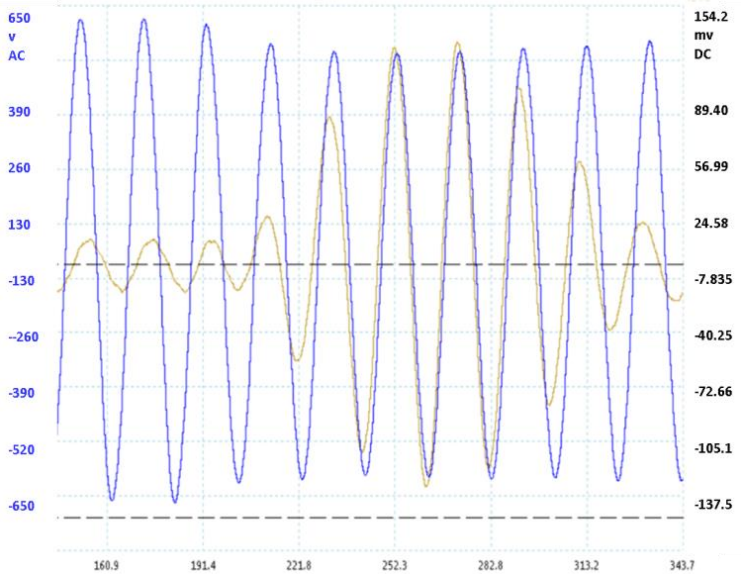

Figure 4.11 Measured transient load performance. Motor input current (brown) and voltage (blue) transient with a step load change from 0 to 30 kW at rated speed (1,500rpm). Scaling is 30ms/div, 130V/div, 32A/div.

4.5 Conclusions

This chapter has examined the steady-state and dynamic performance of a cage-less 16 kW, 1500 rpm interior permanent-magnet machine developed for a portable generator application when run as a motor under open-loop volts-per-hertz control from an inverter. This type of operation allows multiple machines to operate from a single inverter.

Analytical and experimental results show that the proposed machine can operate open-loop at high power-factor over a wide load range with a constant inverter voltage set-point.

The motor showed the ability to start with fast (2 s) volts-per-hertz acceleration ramps with a linear torque versus speed curve corresponding to rated load at rated speed. It also operated stably even with load steps of up to twice rated output power.

Detailed finite-element analysis was used to show that the combination of the flux-concentrating spoke-type topology and the twin magnets in each rotor pole provided a high demagnetization withstand capacity. No issues with demagnetization were observed experimentally even with peak currents during transient operation of up to four times rated current.

Based on the above results, the proposed cageless interior permanent-magnet machine shows promising performance for use in open-loop inverter drives.

Chapter 5 : Investigation of Emerging Magnetic Materials for Application in Axial-Flux Permanent-Magnet Machines

This chapter investigates the performance of three magnetic materials: silicon iron, soft magnetic composite and amorphous magnetic material, as the stator of an axial-flux permanent-magnet machine. Three stators, one of each material, are built and tested with the same rotor. The losses of each of the machines are separated using a combination of 3D finite-element analysis and experimental testing under open-circuit and loaded conditions.

Chapter 5

5.1 Introduction

Electrical machines with high rotational speeds have an extended range of applications including: electric vehicles, blowers, compressors, grinding machines, mixers, pumps, textile machines, drills, aerospace, flywheel energy storage etc. In recent decades, factors like the rising price of energy and standards introduced by organizations such as the International Electro-technical Commission (IEC) were the driving force for extensive research toward high efficiency machines. To achieve this goal both the machine materials and design should be considered.

A direct comparison of electrical machines using three different magnetic materials: silicon iron (SI) lamination, soft magnetic composite (SMC), and amorphous magnetic metal (AMM) is presented in this chapter. Two of these materials (SI and AMM) have laminated structures and the third (SMC) is a composite material. Note that both SI and AMM laminations limit the machine design to 2D magnetic structures with 2D flux paths to prevent excessive eddy current losses produced by flux passing perpendicularly through laminations.

An axial-flux permanent-magnet (AFPM) design is considered in this study primarily for two reasons: it can be manufactured using the three magnetic materials mentioned above, and this design allows studying an adjustable air gap without altering the stator or rotor dimensions. Note that an axial topology is most suitable for AMM designs as it can be more easily manufactured in mass production. In addition, the axial design can also achieve high torque density while offering lower noise and vibration compared to the traditional radial-flux permanent-magnet machine designs [41]. Therefore, the primary aim of this chapter is to provide a detailed comparative study on electrical machines to target high efficiency while operating at higher speeds than the conventional range.

Laminated silicon iron is the most common magnetic material used in electrical machines. SI is categorized as non-grain oriented (NGO) and grain oriented (GO). The NGO has similar magnetic properties in all directions whereas GO steel is processed in such a way that the optimal properties are developed in the rolling direction with up to 30% improvement of magnetic flux density. This material has been most effectively used in transformer cores (including current transformers). In addition, it is commonly

used in large generators and other devices where the design permits the directional magnetic characteristics to be used efficiently.

Soft magnetic composite material has emerged as an alternative magnetic material which can offer complex 3D shapes in electrical machine design which is not possible using a conventional laminated structure. The desired core shape using SMC can be constructed by compressing a mixture of iron powder and plastic binder under very high pressures. Because of the moulding process, there is the potential for complex core shapes and low cost high-volume manufacturing. SMC has lower eddy current loss compared to SI due to the high resistivity produced by the insulating binder. However, it has two distinctive drawbacks: low magnetic permeability and high hysteresis loss as a result of the residual stress introduced in the molding process [42, 43].

Research toward improving soft electromagnetic materials has led to consideration of amorphous magnetic metal for electrical machine applications. AMM has high magnetic permeability, and low eddy current and hysteresis losses which has the potential to substantially improve the machine efficiency specifically at high speeds. However, AMM laminations are very thin compared to conventional SI and have also high tensile strength and hardness. The process of stamping, cutting, shaping, and manufacturing of AMM machine is challenging. Thus AMM is presently limited in application mainly to transformers [3] or in electrical machines with a toroidal shape which do not require any cutting [4-6]. However with the development of improved AMM cutting technology [7-9], the application of AMM in the electric machine construction requiring slotting of the core is now feasible specifically for axial flux designs. Although the application of cut AMM in electrical machines is still rare, some designs have already been reported in [9] and [44].

In [44], conventional NGO-SI, SMC and AMM are used in the stator teeth of a radial flux machine. The proposed technique has serious limitations in commercial production, and also there is a significant gap between the analytical and measured results due to the use of a simplified model.

This chapter aims to provide full utilization of these materials as stator cores and presents a comprehensive investigation to compare their performances using identical stator and rotor topologies while operating under identical conditions. In addition, three prototype machines developed in this study aim to fill the research gap by offering a

baseline study for the application of AFPM machines using a 3D finite element design approach. The designs have been verified experimentally and separation of the losses is also given both under open-circuit and full load conditions up to 5000 rpm. Detailed loss breakdowns are provided in the chapter targets further efficiency improvement opportunities in all three designs to meet and even exceed the IEC energy efficiency standards.

5.2 Magnetic Characteristics of Materials

5.2.1 Stator Iron Cores

Before the construction of the AMM, SMC and GO-SI slotted axial-flux stator cores, the magnetic characteristics of the magnetic materials are obtained using the identical size uncut toroidal cores shown in Fig. 5.1(a). The main and auxiliary windings used during the core tests are also shown for the AMM core only.

To verify the magnetic properties and iron loss characteristics of the three stator cores with respect to their data sheets, the core loss tests were performed for a range of frequencies using the test setup illustrated in Fig. 5.1(b). A programmable AC power supply was used to excite the main winding at a given frequency and a search coil (auxiliary winding) is used to measure the induced voltage that is used to calculate the flux linkage.

Fig. 5.1(c) shows the comparison of the BH curves for the three cores at 50 Hz. The measured results indicate that AMM has the smallest hysteresis loop area and consequently the lowest iron loss while SMC had the largest area and iron loss. The SI lamination is a high quality GO (27RGH100) material used in current transformer applications, but due to availability of the laminated strips, it is chosen for prototyping. Therefore, its hysteresis loop area is much smaller than the conventional SI laminations commonly used in commercial rotating machines.

Fig. 5.1(d) shows the measured loss (symbols) of each core material at 1 T as a function of supply frequency up to 600 Hz which covers the high speed operating range via an inverter. The data sheet values (lines) of the losses of each core material are also given and show good agreement for the AMM and the SMC cores. However, the high frequency iron loss data was not available for the GO-SI material. To provide a reference, the manufacturer’s iron loss data for a common NGO-SI material, M19, is

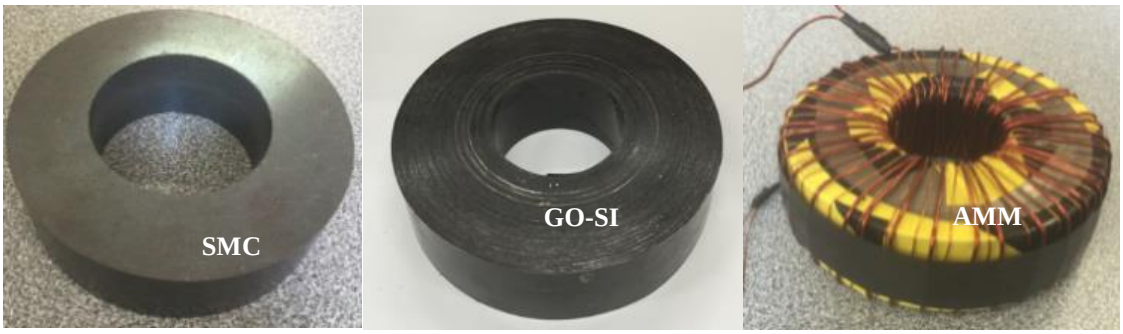

(a)

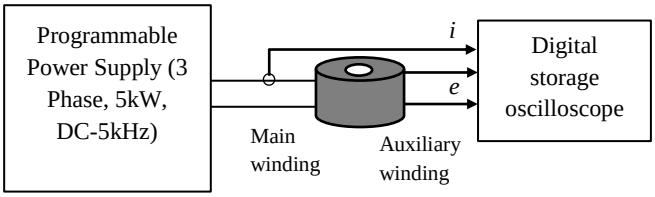

(b)

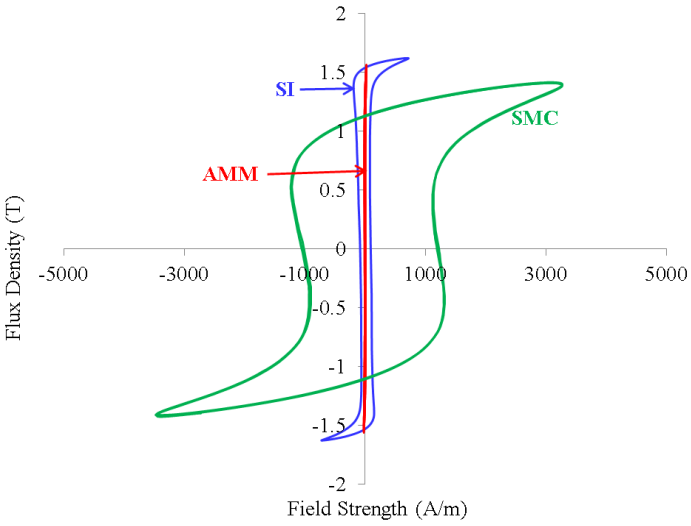

(c)

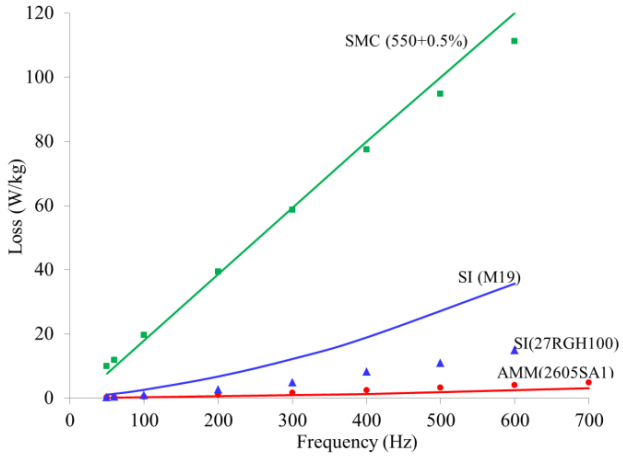

(d)

Figure 5.1 (a) Photos of three uncut cores from left to right: SMC, GO-SI, and AMM cores, (b) the block diagram of the iron loss measurement test setup, (c) measured B-H characteristics at 50Hz, and (d) iron loss characteristics at B = 1 T

also shown in the picture.

Note that both AMM and GO-SI cores have much lower losses than the SMC core, and there is a significant difference in the losses at higher frequencies. For example, at 600 Hz, the losses in GO-SI, NGO-SI and SMC are much greater than the loss of AMM (4, 9, and 28 times respectively). To obtain a more accurate simulation, the measured iron losses versus frequency results are utilized in the FE analysis.

5.2.2 Permanent Magnet Testing

The permanent magnets used in the rotor of all three machines are bonded NdFeB magnets with an arc-shape and are provided by Beijing OeMag International [45]. The open-slot stator design required the use of bonded rather than sintered magnets to avoid excessive magnet eddy-current losses. The data provided by the manufacturer indicated a value of remanent flux density (Br) between 0.70 and 0.74 T. The magnet's residual flux density was estimated by combining the results from a series of measurements on a stack of magnets using a Gauss/Tesla meter (F. W. Bell 5080) (Fig. 5.2 (a)) and FE simulation to verify the datasheet values.

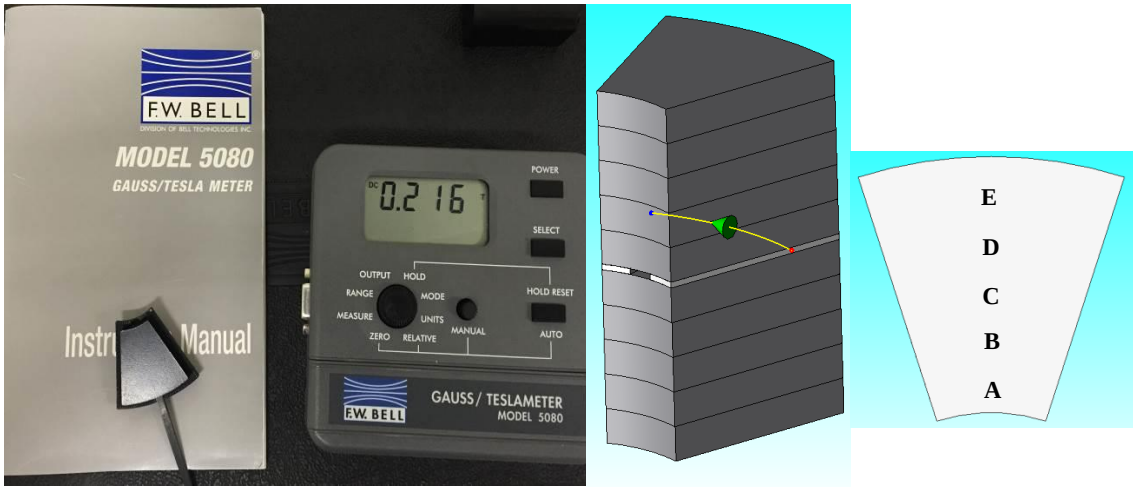

(a) (b) (c)

Figure 5.2 PM remanent flux density testing, (a) F.W. Bell flux meter, (b) PM test accompanying 10 identical size PMs, (c) measured points across the middle of magnets

The magnet test configuration shown in Fig. 5.2(b) was used to obtain the actual values of the magnet flux. It consists of an equal number of magnets placed on opposite sides of a non-magnetic spacer of thickness 1 mm. The spacer has a radial slot in it to guide the magnetic field probe (which is also 1 mm thick) for repeatable measurements. The tests were done with magnets away from any magnetic objects which would distort

Table 5.1 PM's and Measured Point's Dimensions.

PM's Inner Radius	22.5mm
PM's Outer Radius	55mm
PM's arc	35.5°
A Radius	25.55mm
B Radius	29.55mm
C Radius	38.75mm
D Radius	45.85mm
E Radius	51.95mm

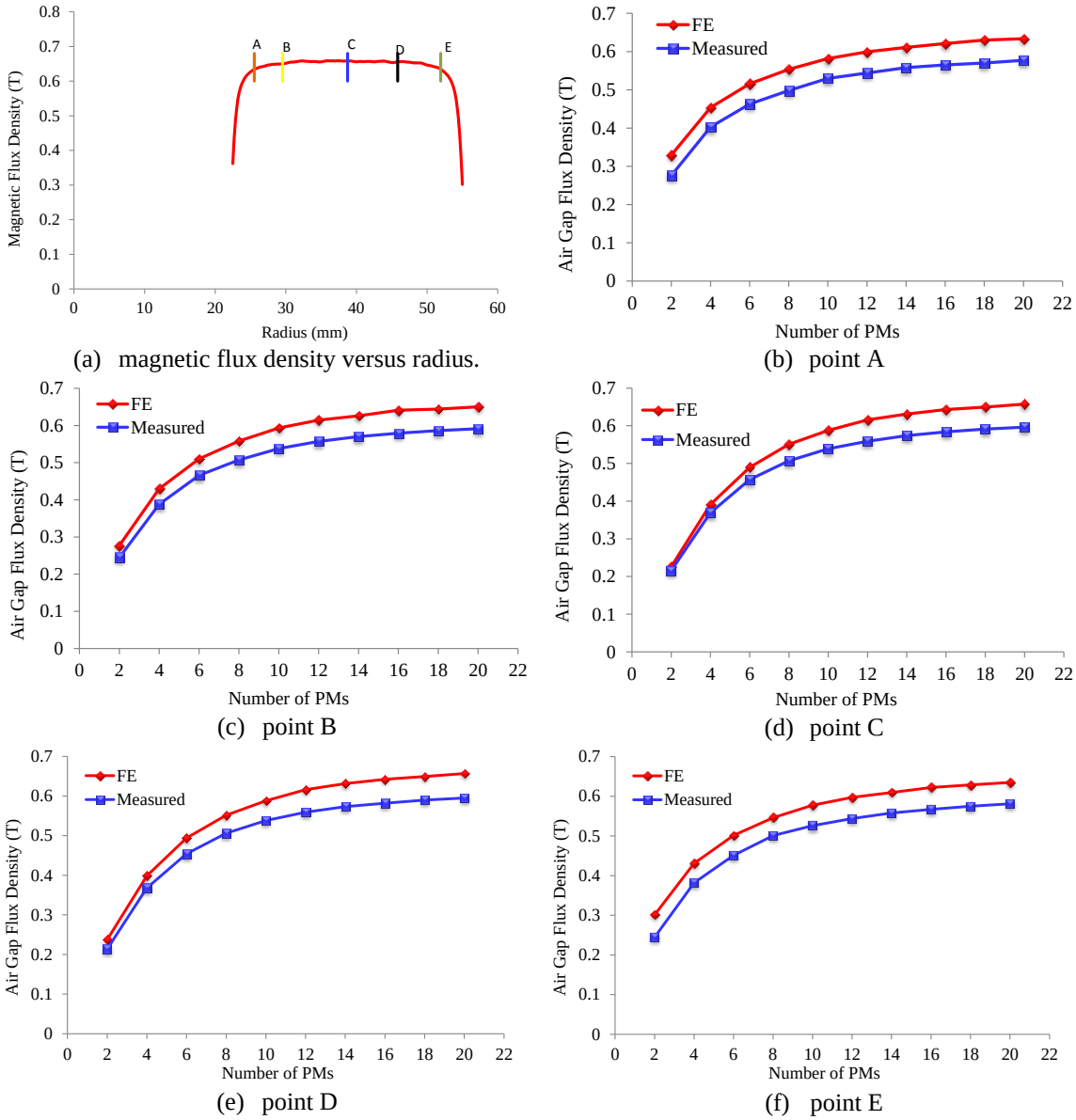

(a) magnetic flux density versus radius.

(b) point A

(c) point B

(d) point C

(e) point D

(f) point E

Figure 5.3 FE and test flux density comparison for 5 different points across the middle of PMs.

the field pattern. A test was conducted for 2 magnets (one on each side) and repeated with up to 20 magnets (ten on each side). A higher number of magnets provide a stronger magnetic field and hence more reliable results. Five points along a radial line through the middle of magnets are selected as the fringing/edge effects were the

smallest in the middle section (see Fig. 5.2(c)). A probe with a 1 mm thickness was used. The measured points are shown in Table 5.1. Based on the information provided in data sheet, the expected Br value is between 0.7 T and 0.74 T. The value of 0.71 T is selected for FE simulation and although C and D are the benchmark points, the results for all 5 points are also presented in Fig. 5.3 for further confirmation.

Based on the measured air gap flux density, the remanent flux density is calculated (Fig. 5.4) for the mentioned 5 points indicating instead of the expected 0.7 T$\leq B_r \leq$0.74 T, the real Br value is 0.65T (9% less than the minimum value).

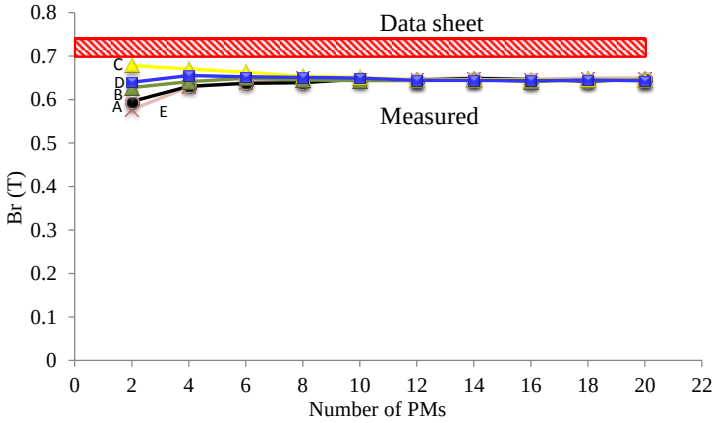

Figure 5.4 FE and measured Br comparison.

5.3 Finite Element Simulation

Due to the axial-flux topology of the studied machines the only option for analysis was 3D simulation. In this research the JMAG software [22] was used. To reduce the computation time it is possible to model a portion a machine using the symmetry and periodicity according to the number of slots/poles configuration. For the 12S10P axial-flux machine, the smallest model is the half model using the periodicity with full axial length (the symmetry condition cannot be used).

By using the JMAG-Designer it is possible to either create the geometry using the "geometry editor" or import it from other CAD softwares. In this work, the 3D model was first generated using the "geometry editor" and saved in the 'SAT' format.

After creating the model and selecting the analysis type, thee mesh size is determined. FEM uses a large number of elements to calculate the magnetic field variation so a smaller mesh size estimates the magnetic field more accurately. However, there is tradeoff between the precision and calculation time as larger number of

elements requires more memory and disk space and consequently larger computation time.

In the FEM it is possible to define the finer mesh only when it is necessary. The areas like the magnets and stator tooth that have large variation of magnetic flux needs finer mesh to achieve adequate precision. It is also similar with the conductor surfaces with significant circulating eddy current. The eddy current in the skin layer (conductor surface) reduces exponentially with depth into the conductor. The thickness of the skin layer is defined as

$$\delta = \frac{1}{\sqrt{\sigma \mu f \pi}} \tag{5.1}$$

where μ and σ are the permeability and electrical conductivity of the conductor and f is the operating frequency of the model.

The suggested auto generation mesh size was 8mm for all elements which was not appropriate as the simulation did not converge. For this machine the mesh was generated in each step and its size was defined manually for each elements.

The BH curves of the AMM, SI, and SMC as well as their iron loss characteristics obtained using the core tests (section 5.2) were imported to the JMAG material database. The same is correct for the PMs.

To set the direction of current in the 3D windings it is required that each winding has two parts which allows the “in flow face” current to be defined using the FEM coil condition. The FEM coil condition is used to link the stator windings to the FEM coils in a model. Fig. 5.5 shows an example of the external circuit when the studied machine works as a generator operating into a 3-phase resistive load. The star connection is linked to the windings of the model using the “in flow face” of the FEM coil condition.

The loss in the rotor yoke and PMs is calculated using the modeled circulating eddy currents and the material conductivity. The iron loss in the stator cores is calculated as a post processing step. To calculate the iron losses, the magnetic flux density variations in each element of the machine are calculated as a function of time. Then, the results are analyzed to determine the amplitudes of the harmonics of the magnetic flux density in each element under different frequencies. The iron loss model is used to predict the resultant iron loss in each element including the separated values for hysteresis loss and

eddy-current loss. The losses in the elements are then added to estimate the loss in the entire machine.

Fig. 5.6 illustrates a sample vector plot of magnetic flux density of the machine with the AMM core illustrating the machine topology and the axial flux path in the machine.

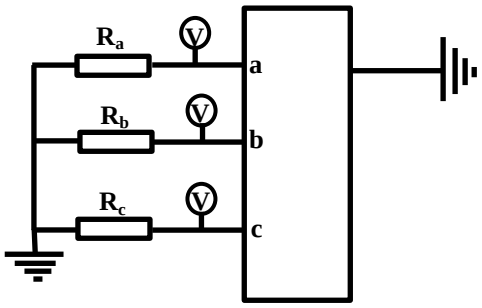

Star Connection

Figure 5.5 Circuit model used in the finite-element program for the generator with 3-phase resistive load.

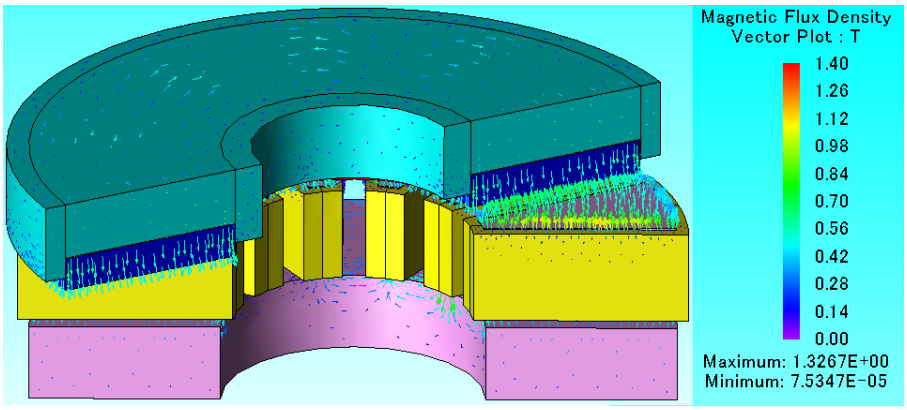

Figure 5.6 Calculated magnetic flux density with AMM axial flux machine.

5.4 Prototyped Machines and Test Set-up

To validate the FE simulation and to separate the machine losses for each core material, three machines were prototyped with the identical sizes. The same rotor was used for testing.

Each stator core in this study has been produced using either conventional machining (for SMC and GO-SI) or water jet cutting (for AMM) techniques. The process of making an AMM stator core starts with winding the unannealed and uncoated AMM ribbon to a flat shape. Then using a special jig, the AMM core is pushed outward to obtain a tapered shaped disc which allows sufficient clearance for abrasive waterjet cutting of the slots. After the cutting process, the tapered stator is pushed back to the flat shape to obtain the axial flux machine topology. Note that in

such a process the AMM core experiences significant level of stress which may result in increased iron loss. The SMC and SI stator cores had slots machined in the stator cores.

Different methods of creating stator slots results in different levels of stress in the materials that can affect the magnetic characteristics of the final slotted core. It can be concluded that the method of manufacturing the AMM core introduces additional core losses, which is primarily due to the applied stress to the core during cutting. This loss can be reduced by appropriate annealing process of the AMM core before the insertion of the windings. In addition, the cutting process in these prototypes can introduce a degree of asymmetry in the position of the slots.

Table 5.2 summarizes the specifications and dimensions of the studied identical-sized AMM, SMC and GO-SI machines. The axial flux machine topology has a stator core with three phase windings and a flat rotor with permanent magnets and a back iron [46].

The machine performance was tested using the custom built test setup shown in Fig. 5.7(a). The test setup consists of the machine under test (either with GO-SI, SMC or AMM core), a high-speed dynamometer setup including a precision in-line torque transducer, a gear box with 1:5 ratio, an induction motor as a prime mover driven by a variable speed drive and a three phase power analyzer. Fig. 5.7(b) and 5.7(c) show the GO-SI stator with windings and the common rotor used with the three stators.

Table 5.2 Specifications and Dimensions of the Machines

DIMENSIONS	
Outer/inner diameters	110 mm/ 45 mm
Axial length	30 mm
Air gap	0.5 mm
STATOR SPECIFICATIONS	
Number of slots	12
Slot depth	17 mm
Winding turns per phase	96
Winding type	Double-layer, concentrated
Measured phase resistance	0.21 Ω
ROTOR	
Number of poles	10
Permanent magnet	Bonded NdFeB
Magnet remnant flux density	0.65 T
Magnet thickness	6 mm
Rotor yoke	Steel 4140
CORE MATERIALS	
AMM	Metglas 2605SA1
Silicon iron (GO)	JFE 27RGH100D
SMC	Somaloy 550+ 0.5% Kenolube 800 MPa

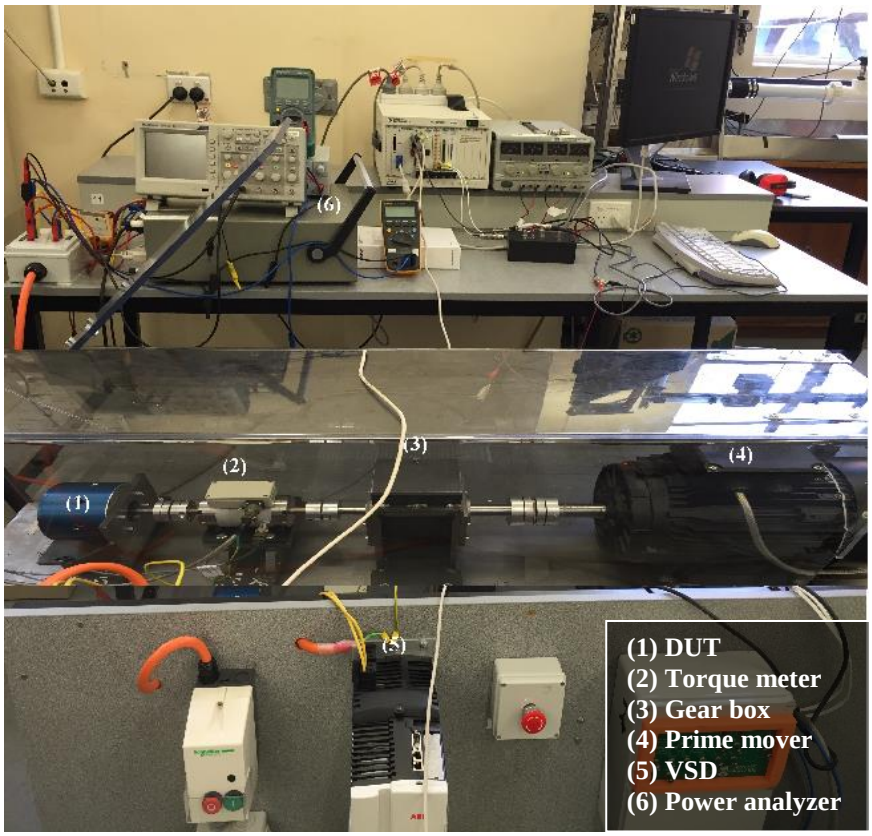

(a)

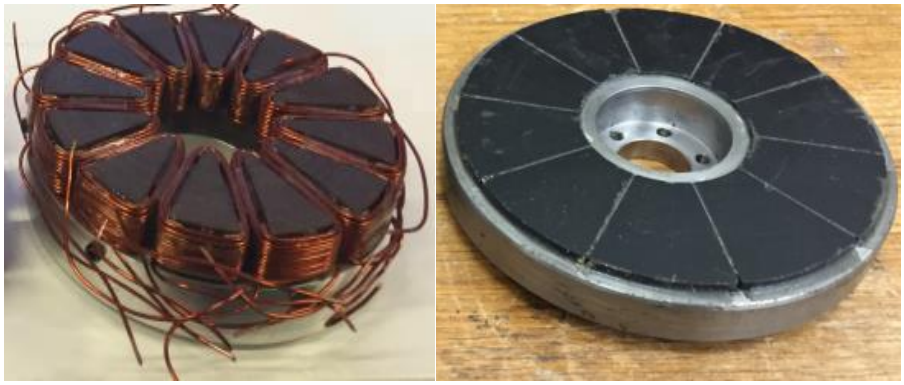

(b) (c)

Figure 5.7 (a) The custom built high speed motor test setup, (b) the GO-SI stator with windings, (c) the common rotor with the bonded permanent magnets and the back iron.

5.5 Torque Offset and Mechanical Loss Verification

The power equation of an electrical machine operating as a generator is formulated as:

$$P_{in} = P_{out} + P_{mech} + P_{SFe} + P_{RFe} + P_{PM} + P_{Cu} \quad (5.2)$$

where P_{in} is the input power; P_{out} output electrical power; P_{SFe} stator iron loss; P_{RFe} rotor iron loss; P_{PM} the magnet loss; P_{mech} mechanical loss and P_{cu} copper loss in the

stator winding. A loss separation in electrical machines is a useful approach to gain a better understanding of the potential loss reduction opportunities for efficiency improvement. Therefore, a wide range of simulation studies and tests have been carried out on the three machine configurations in order to separate the machine losses as formulated in (5.2).

5.5.1 Torque Meter Offset

Loss measurements under open-circuit conditions require measurements of small values of torque and are thus sensitive to torque meter offset errors. Thus a first step towards the loss separation involves the correct calibration of the inline torque transducer. In addition, it is important to run the machine and torque transducer for some time before taking measurements in order to warm up the bearings and thus produce more consistent bearing loss results.

The torque offset result is performed with the machine under test being disconnected from the torque transducer and so the only load on the torque transducer being its own bearings. Torque readings are taken from 0 to 5,000 rpm with both positive and negative speeds. The torque transducer used has a dual-torque range of 4.52/22.6 Nm so the torque measurements are small compared to its rating.

An open-circuit test is then performed and the measured results obtained. With an open-circuit test it is expected that the loss results will be symmetrical for positive and negative speeds.

Fig. 5.8 illustrates a sample offset test result obtained from one of the machine topologies. The torque meter offset value is subtracted from the measured open-circuit results to give the curve labeled “First Correction”. The results still has a residual zero offset which is removed by adding a constant value to produce a final torque versus speed curve which is symmetrical about the zero torque point.

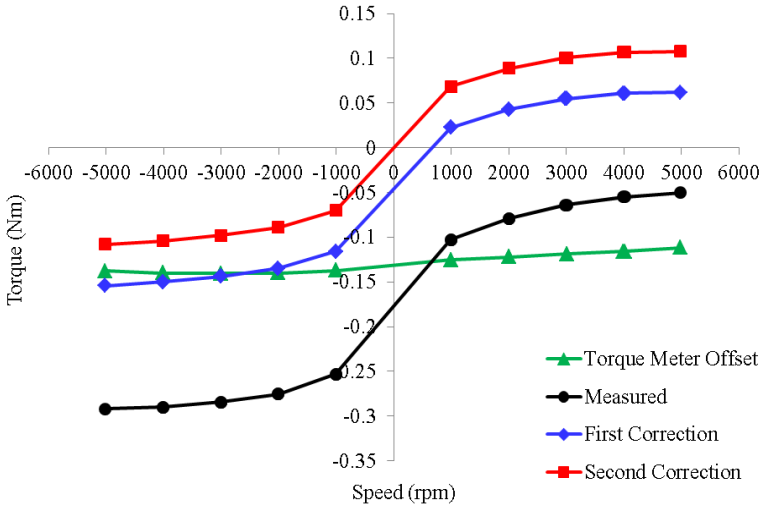

Figure 5.8 Torque meter offset correction test results when applied to the open-circuit measurements.

5.5.2 Mechanical Loss

Mechanical losses due to bearings can be significant in single-sided AFPM machines. This is due to the large magnetic attraction force between the PM rotor and the stator. This imposes considerable axial force on the bearings. It is thus inaccurate to estimate the mechanical loss using tests based on a rotor disc without PMs.

Reference [47] describes the idea of performing tests on an axial flux machine with the stator reversed so that the rotor sees a smooth surface (see Fig. 5.9(a)). This reduces the rotor losses to nearly zero and the stator losses are substantially reduced. In [47] it was thus assumed that the resultant measured loss was only mechanical loss.

However, this approach does not take into account the fact that stator iron losses still exist in this configuration and these losses can be significant for high loss cores. To eliminate the effect of stator core loss, the machine with an uncut stator has been modeled and the calculated core loss has been subtracted from the measured values which provides the most accurate estimation of mechanical loss.

Fig. 5.9(b) illustrates the FE simulation results of the iron loss contour plot using the SMC core at 5000 rpm which shows significant iron losses in the core. This process was conducted on the SMC and SI cores.

Fig. 5.10(a) compares the measured losses for the smooth stator test versus the FE electromagnetic loss predictions for the same case which do not include mechanical

loss. By subtracting the FE prediction from the measured values, the mechanical loss as a function of speed can be found.

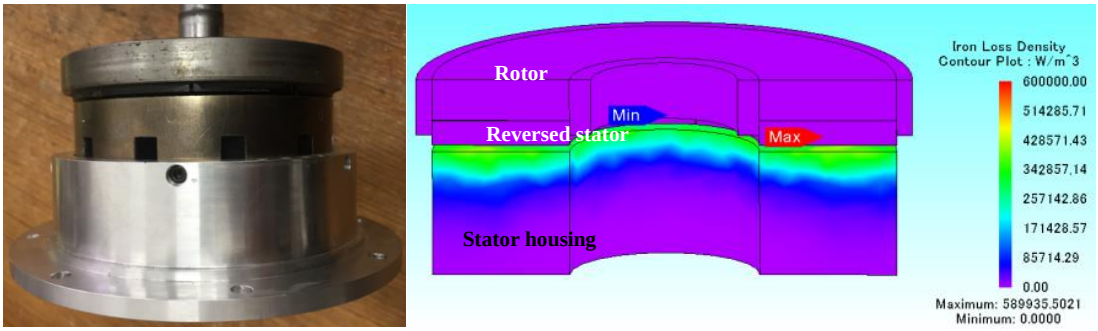

(a) (b)

Figure 5.9 (a) Rotor and the reversed stator test arrangement used to measure mechanical loss, (b) the FE model without stator slots at 5000rpm.

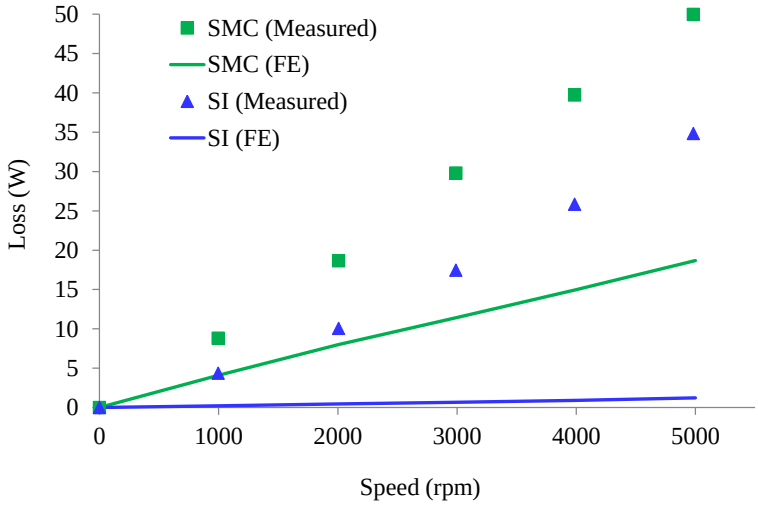

(a)

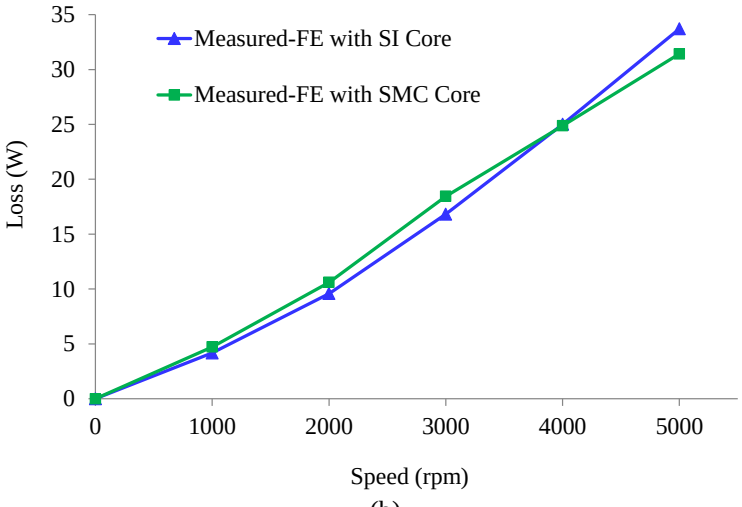

(b)

Figure 5.10 (a) Measured versus simulated test results of the reversed stator, (b) measured mechanical loss comparison of the SI and SMC machines.

Fig. 5.10(b) shows an excellent agreement for the mechanical losses between the SMC and SI machines which would be expected to be the same given the same rotor is used and the stators have similar geometry. It also confirms the high mechanical loss of this axial-flux machine.

5.6 Open-Circuit Test

5.6.1 Back-Emf

Using the test setup given in Fig. 5.7(a), the open-circuit test was performed by rotating each machine and monitoring their terminal voltages. For comparison purposes only one phase of each machine's back-emf waveforms is given in Fig. 5.11(a), and the results from the three machines are shifted by 120° to separate them. The machines have

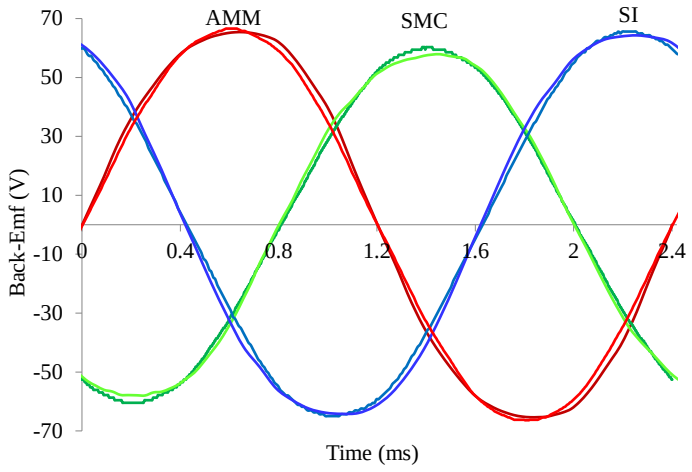

(a)

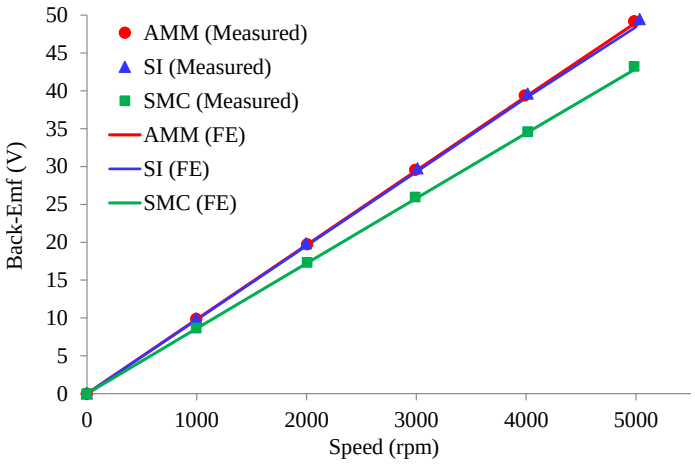

(b)

Figure 5.11 Open-circuit tests and FE results for three different machines (a) back-emf waveforms at 5000rpm with the darker lines being FE results and the lighter lines being the test results, (b) RMS values of back-emf voltage at various speeds.

a sinusoidal back-emf where the measured waveform shape and amplitude are in good agreement with the FE results.

Fig. 5.11(b) shows a comparison of the rms phase back-emf voltage versus speed. The results are similar for the AMM and GO-SI machines but are 12% less for the SMC machine, likely due to its lower magnetic permeability.

5.6.2 Open-Circuit Loss

Fig. 5.12(a) compares the measured and calculated open-circuit losses for the SMC, GO-SI, and AMM machines at speeds up to 5000 rpm. The calculated results did not include mechanical losses which resulted in a factor of two differences between them.

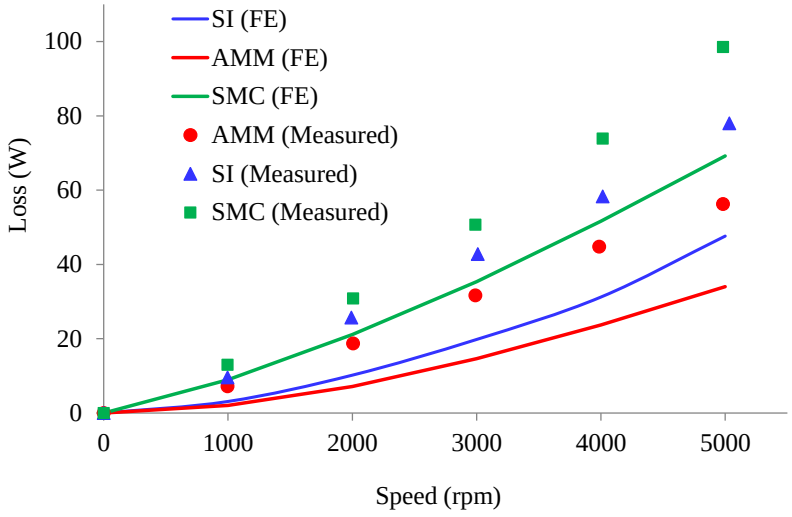

(a)

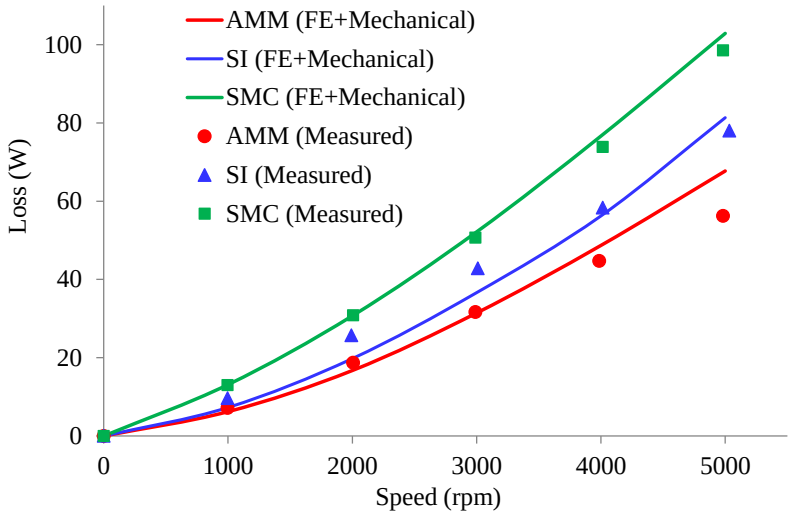

(b)

Figure 5.12 Open-circuit tests and FE results for three different machines (a) loss comparison without considering mechanical loss, (b) loss comparison with mechanical loss.

Fig. 5.12(b) compares the measured open-circuit loss results with the simulated results including the measured mechanical loss from Fig. 5.10(b). This provides a much better correspondence between the measured and simulated results, particularly for the SMC and AMM cores.

Consider again the simulated electromagnetic loss results in Fig. 5.12(a). Compared to the FE results for the AMM machine, the open-circuit loss of the SMC machine is about 4.4 times higher at 1000 rpm which reduces to about 2 times at 5000 rpm. The GO-SI to AMM loss ratio however, is almost constant where the GO-SI had almost 1.3 times the loss of the AMM machine. In addition, the ratios between the measured open-circuit losses of the SMC and SI machines with respect to the AMM machine is about 1.7 and 1.4 respectively.

Fig. 5.13 summarizes the calculated loss breakdown of each machine topology including the measured mechanical losses. The rotor back iron and PM losses are similar for all three machines.

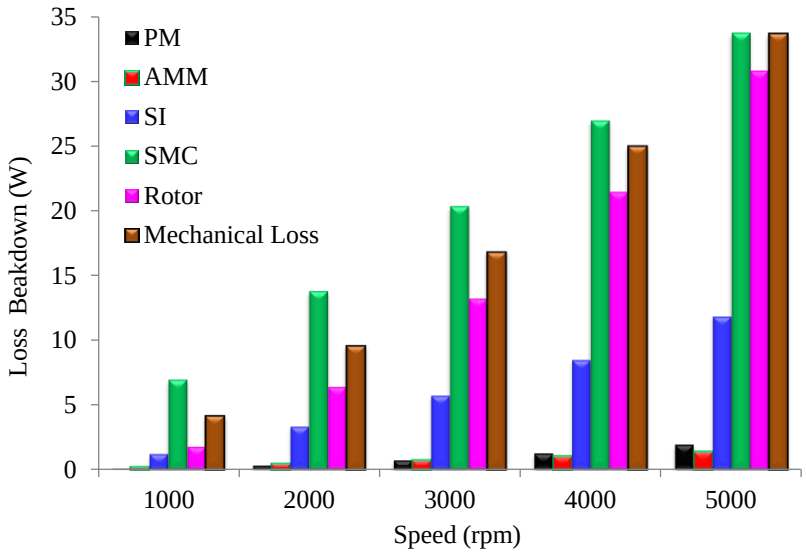

Figure 5.13 Calculated open-circuit loss breakdown for the three machines topologies including the measured mechanical loss.

It was observed that only 2.5% of the total loss in the AMM machine is related to the stator loss. This loss is 35 times higher in the SMC core than the AMM core at 1000 rpm, which is reduced to 26 times at 5000 rpm. This indicates that although SMC has considerable higher loss than AMM initially, its relative performance improves at higher operating frequencies due to its low eddy-current loss. For the GO-SI stator, this ratio increased from 7 to 8.5 showing considerable lower loss of the AMM core even when a high quality and low loss GO-SI is used as the core.

The PMs have on average 2% of the total loss at 5000 rpm speed range which is small. This is reasonable given that bonded magnets were used.

The rotor losses in Fig. 5.13 displayed an increasing trend from 28% to 45% of the total loss within the speed range shown. It is likely that this is due to the large slot openings in the stator cores (due to the open-slot design) which lead to large rotor flux variations, resulting in significant eddy-current losses in the solid rotor yoke. Note that this loss can be reduced significantly either by using the semi-closed slots on the stator and/or an improved rotor design with a different back iron material. These options will be explored in future work.

Mechanical loss is observed to be the most dominant loss both in the AMM and the GO-SI machines (67% of the total loss at 1000 rpm, 50% at 5000 rpm). These percentages were found to be slightly lower for the SMC machine.

5.7 Full-Load Test and Loss Breakdown

The three machines were tested as generators at full load (1500 W, 5000 rpm) using a 3-ph resistive load and the test set-up shown in Fig. 5.7(a). A three-phase power analyzer and torque meter were used to record the input torque, output electrical power, speed, voltage, current, and power factor for each load value. The offset torque correction procedure described in section 5.5 was used to correct the torque readings. In addition, the performance of the machines was also modeled under resistive loads. Fig. 5.14(a) illustrates the loss breakdown at 5000 rpm as a function of output power. Note that since the PM losses are similar for the three machines, only one characteristic curve is included in this figure.

At the rated load of 1500 W, the GO-SI machine has 7.4 times and the SMC machine has 20 times more stator core losses compared to the AMM machine. Note that the SMC and GO-SI core loss reduces slightly with increasing load. This is likely due to stator armature reaction flux reducing the total core flux under load.

The PM loss has been about 1% of the total loss in all three machine topologies.

The highest loss component is the copper loss (about 50% of the total measured loss at rated load). The copper loss values of AMM and SI are similar and are about 29% lower than for the SMC machine. This is due to the back-emf of the SMC machine

being 12% lower which leads to a higher current for the same output power and with the equal winding resistance, higher copper loss.

The rotor loss is the second highest loss component, about 25% (in all machine types) which is also nearly equal to the mechanical loss. It was observed that the rotor loss increases about 5 W with the load in each machine topology.

Fig. 5.14(b) summarizes the performance of the machines under open-circuit and full load conditions (shown with O and L). For all three machines the stator loss reduced under load (this was about 23% for AMM and GO-SI, and about 32% for SMC). In contrast, the rotor loss increased by 16% for AMM and 37% for GO-SI and SMC. The PM and mechanical loss are considered constant. It is interesting to note that the total iron loss for each machine does not change significantly between the open circuit and full load conditions.

After the detailed separation of the losses, the efficiency of each machine is calculated both using the measured and the simulated values by FE analysis (Fig. 5.14(c)). Under the rated load of 1500W, the maximum calculated efficiencies of the AMM, GO-SI, and SMC machines are found to be about 91%, 90% and 87%, respectively. In addition, it can be seen that the difference between the FE and the measured efficiency characteristics of the AMM machine is slightly larger than for the other machine topologies.

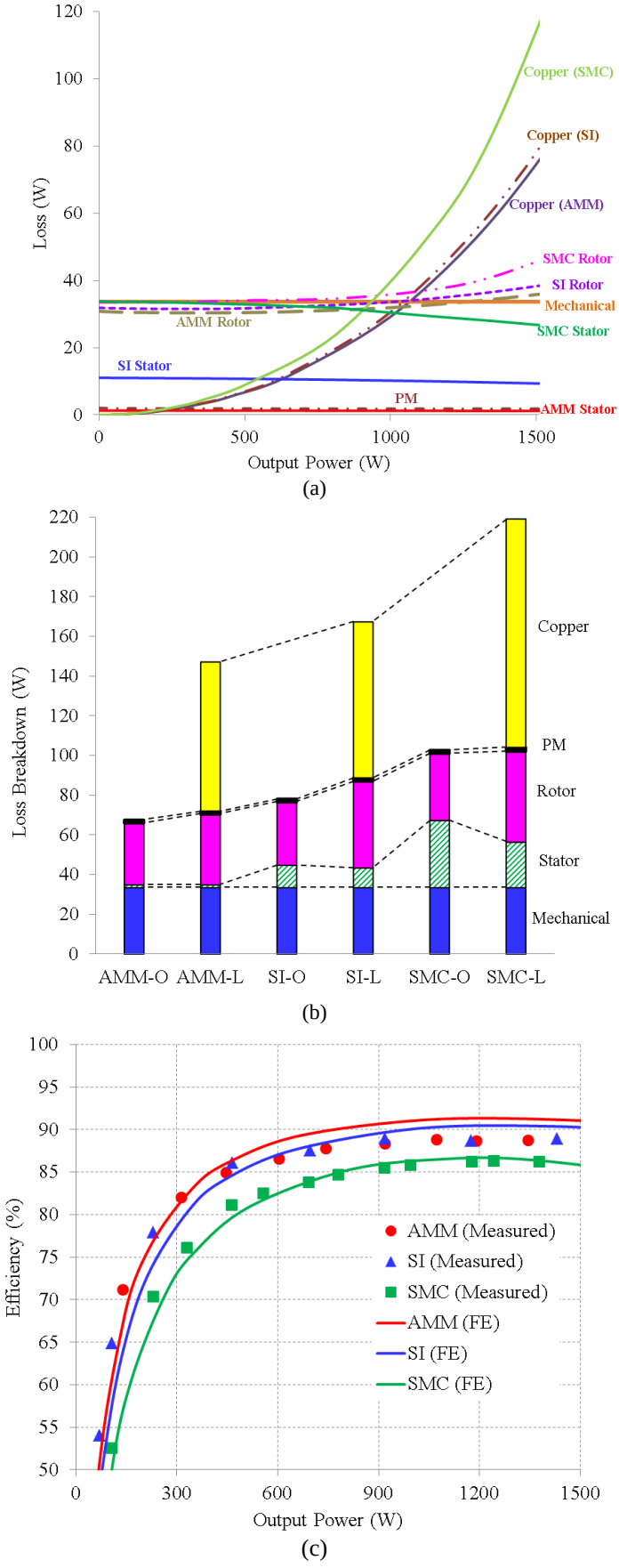

Figure 5.14 Performance comparison of the GO-SI, SMC, and AMM machines under resistive load at 5000 rpm: (a) calculated loss breakdown under loading condition, (b) calculated open circuit and full load loss breakdown, and (c) measured and FE efficiency comparison.

5.8 Conclusion

In this chapter, the performance of two emerging magnetic materials (SMC and AMM) is compared with an existing high quality grain-oriented silicon iron lamination material to understand their performance in high efficiency machines.

Although grain-oriented lamination material is not commonly used in electrical machines due to its higher cost and asymmetric magnetic properties, the GO-SI machine provides a useful benchmark for comparison.

Firstly, uncut identical-sized, ring-shaped cores of the three magnetic core materials were tested. The measured iron loss results corresponded well with the manufacturer's data sheet values and demonstrated the low AMM iron loss, specifically at higher frequencies.

Slots were then cut in the AMM, SMC and GO-SI cores and they were wound to produce three identical-sized stators with three phase windings. A single 10-pole rotor with bonded magnets was also built to be used with these three stators. The losses of each of the three machines were separated using a combination of 3D FE simulation modelling and experimental tests up to 5,000 rpm.

The mechanical losses of the cores were estimated using a combination of measurement and simulation of the PM rotor operating with a stator without slots.

The open-circuit test results indicated 12% lower back-emf voltages in the SMC machines compared to the AMM and GO-SI machines, which is likely due to its lower magnetic permeability. The measured back-emfs and open-circuit losses were found to be similar to the FE simulation results. The FE loss breakdown at 5,000 rpm indicated that the SMC and the GO-SI machines have 26 and 8.5 times more stator losses respectively compared with the AMM machine. The mechanical loss was the largest of the loss components and consisted of approximately half of the open circuit loss. This is likely due to the high axial loads of the single-sided design.

A substantial rotor loss was also observed due to the open stator slots of the stator cores resulting in large rotor flux variations and hence eddy-current losses in the solid rotor yoke. Means to reduce this will be considered in future studies.

The simulated generating efficiencies of the AMM, GO-SI, and SMC machines were found to about 91%, 90% and 87% respectively under the rated load of 1.5kW and showed a good correspondence with the measured results.

Further improvements in the efficiency of the AMM machine can be made by annealing the stator core after construction.

Furthermore, it can be concluded that the two emerging magnetic materials can offer practical designs to achieve high efficiency while operating at higher speeds than the conventional speed range. Such higher speed machines can offer promising options in a range of practical application where the system efficiency is critical.

Chapter 6 : Loss Analysis and Efficiency Improvement of a Tapered Axial-Flux PM Amorphous Magnetic Material Machine

Amorphous magnetic materials (AMM) have been used in low frequency power transformer applications for more than two decades but are not presently commercially utilized in high frequency rotating electrical machines due to the lack of a suitable handling method and an economical cutting technique. In this chapter a novel brushless synchronous permanent magnet electrical machine suitable for a range of high-efficiency, high-power density and high-speed machine applications is introduced. It consists of a 12-slot 10-pole tapered axial-flux permanent-magnet machine utilizing amorphous magnetic material in the stator core. Then novel loss separation techniques including mechanical loss and locked rotor tests are described. High rotor yoke loss was identified in the baseline design. Finally the rotor design was modified and a significant improvement in efficiency was demonstrated.

6.1 Introduction

Since rotating electrical machines consume a significant portion of the electricity generated, designing high efficiency machines is a primary interest to many researchers. This is also reinforced by the new energy efficiency standards. In addition, higher operating speeds are desirable in many applications primarily to address the specific application requirements (such as in routers, centrifugal pumps, air blowers and flywheels) and also to reduce physical size and weight of machine (mainly in portable systems). However, due to the limitations of the conventional laminations, special attention is given to utilizing emerging magnetic materials such as AMM in machine design [48].

AMM is promising for addressing the above research targets as it has high magnetic permeability and low eddy current and hysteresis losses. However, due to previous issues with cutting, AMM was limited to applications which require no cutting, such as transformers [3] or in toroidal electrical machines [4, 44]. In [44], AMM was utilized in a brushless permanent-magnet (PM) motor and compared with soft magnetic composite and conventional steel laminations without experimental validation. In [4], the performance of a toroidal slotless and round slotted AMM machines were compared. However, in the slotted version, only 75% efficiency at the rated power of 1kW was achieved. This is likely due to anisotropy of the core and mechanical stress in the fabrication process.

The development of improved AMM cutting technology [7, 8] has made feasible the application of AMM in slotted electric machines, specifically for axial-flux permanent magnet (PM) designs.

In [6], an axial-flux PM machine using AMM was reported in a single-stator double-rotor topology. In this paper, the stator pole pieces were constructed by winding AMM ribbon into a core. A thin slit was cut in the core to reduce the eddy-current losses. An efficiency of 85% at the rated power of 200 W was achieved. A continuing study, published in [5], demonstrated 90% efficiency by using similar stator poles with left-right asymmetric skewed magnets at the lower rated power of 150 W.

In [49], a 20 kW radial-flux PM AMM machine was reported with an efficiency of 95% however the manufacturing of such a radial flux topology is not presently viable for mass production.

The previous studies have not yet shown a practical topology to offer economical and reliable production of high-speed AMM machines at high efficiency.

The difficulty of accurately and economically cutting AMM to achieve the complex stator structures due to its extreme hardness led to considering a tapered design [8] which significantly reduced the manufacturing cost which is one of the major barriers preventing commercialization of AMM in rotating electrical machine applications.

Fig. 6.1 illustrates the proposed electric machine structure, where, the stator iron is shown with its laminations, the magnets have a gray fill, and the windings are highlighted with a diagonal line pattern. The arrows indicate the direction of the major components of the magnetic flux flow. It is important to note that unlike the conventional radial and axial machine topologies, the flux flow in this tapered-field design includes both radial and axial components.

Note that the tapered-field design is not suitable for conventional silicon-iron laminated structures due to the larger thickness of the silicon-iron material which limits the formation of a smooth stator structure.

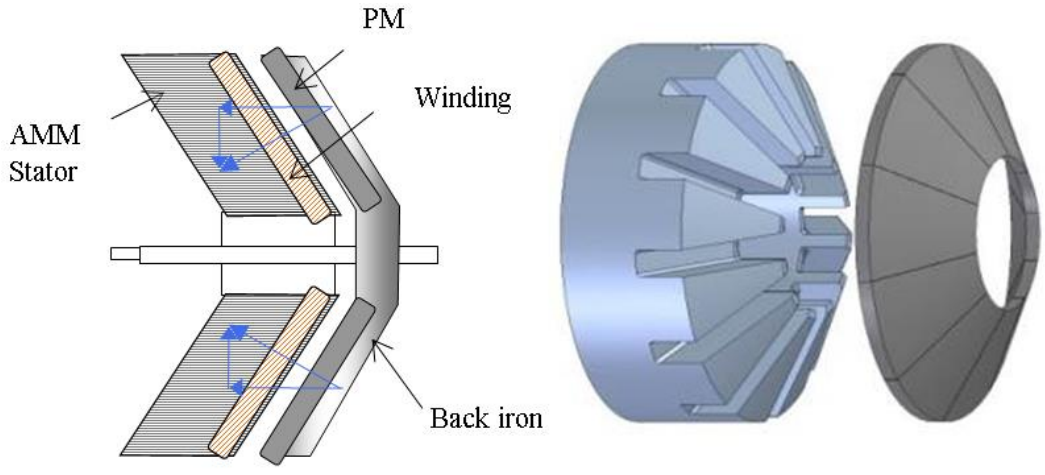

Figure 6.1 The novel AMM brushless permanent magnet motor, (a) The cross-sectional view, (b) 3D view of the stator core with open slots and the magnet structure.

The literature survey performed on angled electric motors [50-53] revealed that previous studies were primarily focused on improving the electromagnetic performance

and use silicon iron material, but without considering their manufacturing benefits for materials such as AMM.

For example, Demag's brake motor uses axial force in its braking mechanism, and axial force is integral to the Electrotechnical Institute's rotary-percussive mechanism [50] to provide both rotary and axial motion. In addition, NovaTorque's hybrid design [51] provides a motor with additional benefits over conventional axial-field motors, including higher torque, improved thermal performance and simpler windings. Note also that the use of the hybrid shape in NovaTorque's design changes the flux path from that of a conventional machine, leading to the removal of back iron. However, such a design increases the complexity of both manufacture (as it requires different-sized laminations stacked together), and construction (assembling the stator poles together). In these previous hybrid studies, an angled rotor is combined with an angled stator in order to maintain a uniform air gap. However, the switched reluctance machine by GE [52] with a single bearing combines an angled rotor with a conventional cylindrical stator to produce an uneven air gap to reduce the radial force and the effect of eccentricity on the rotor. This offers protection against the rotor and stator making contact.

A sandwich type dual-rotor flat axial-field AMM rotating machine has also been reported recently in [5, 6]. The topology described in these studies included two different AMM based stator pole piece structures which were obtained by wrapping (with a final slit to reduce eddy current loss) and by cutting (to obtain a pole piece made from various sized AMM laminations). The pre-formed windings and the AMM pole pieces are then encapsulated to form a complete stator sandwiched between two permanent magnet rotors. Although, the concept machines have demonstrated high-efficiency operation, the rigidity of the stator structure and the handling/manufacturing/assembly cost of the pole pieces have not been assessed and reported. In addition, the high speed operation and heat dissipation characteristics of the concept machines have not been investigated which are critical for commercial products.

In this chapter the machine shown in Fig. 6.1 will be introduced first. Then it will be studied using extensive simulation and practical measurements to address accurate identification of loss components. Then the possibility of further efficiency improvements of the machine is studied. Due to the tapered topology of the machine, a

novel process has been developed to measure the mechanical loss. In addition, for the first time the locked rotor test was introduced as a reliable method to separate the stator and rotor loss in a PM machine. This method can be used to quantify the iron loss components for all machine topologies. Three design variations including air-gap, PM shape, and rotor yoke design have been considered. The final design shows the successful improvement of efficiency by 3.5% where the simulated results have been confirmed empirically.

6.2 AMM Machine Topology and Test Set-Up

6.2.1 Production Methods of Tapered AMM Machine

The principal manufacturing steps of the new AMM machine stator topology are illustrated in Fig. 6.2 and explained as follows: the unannealed and uncoated AMM ribbon is wound to a tapered shape (Fig. 6.2(a)) as tightly as possible to achieve the maximum stacking factor; the core is annealed to improve the material properties after the stresses produced by the winding process of the core; the core is impregnated to insulate the surface of the tape wound AMM core; the cutting of the slots is performed using a custom built jig and abrasive waterjet technology (Fig. 6.2(b)); and finally the stator winding is inserted and a thin layer of resign is applied (Fig. 6.2(c)). Note that the mechanical stress introduced during this processing will result in an increased iron loss and can also affect the impregnation process which needs to be taken into account during the manufacturing process.

The cutting process used in this study produces cuts with smooth edges with no material degradation up to a maximum cutting thickness. Therefore, the thickness of the tape-wound AMM core and the available ribbon width are important to define the maximum size of a tapered-field stator structure which can be cut. Commercially sensitive studies indicate that cutting is economical below a certain thickness and with certain slot profiles. However, it is possible to develop larger diameter AMM machines for high output power, which can be obtained using a nested structure, or alternatively, the same motor structure can be duplicated on a common shaft (multiple rotors and/or stators).

Fig. 6.3 is the baseline rotor showing the bonded flat PM pieces used to create each rotor pole. The open-slot stator design required the use of bonded rather than sintered magnets to avoid excessive magnet eddy-current losses.

(a)

(b)

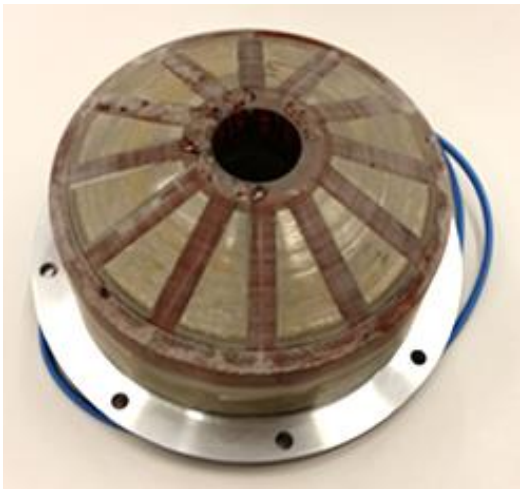

(c)

Figure 6.2 Principal manufacturing steps of the novel AMM machine, (a) tapered AMM stator core before cutting, (b) after the core is cut with abrasive waterjet technology, and (c) stator with windings.

Figure 6.3 Baseline rotor with the bonded PMs.

Table 6.1 summarises the major design specifications and dimensions of the studied machine.

Table 6.1 Specifications and Dimensions of the Baseline Machine.

DIMENSIONS	
Outer/inner diameters	110 mm/ 45 mm
Axial length	30 mm
Air gap	0.5 mm
STATOR SPECIFICATIONS	
Number of slots	12
Slot depth	17 mm
Winding turns per phase	96
Winding type	Double-layer, concentrated
Measured phase resistance	0.21 Ω
Material	Metglas 2605SA1 AMM
ROTOR	
Number of poles	10
Permanent magnet	Bonded NdFeB
Magnet remnant flux density	0.65 T
Magnet thickness	6 mm
Rotor yoke	Steel 4140

6.2.2 Test Set-Up

Fig. 6.4 shows the block diagram of the set-up which included a high-speed dynamometer system where the machine under test is operated as a generator. Both the mechanical input and electrical output quantities are measured simultaneously. The machine under test is driven by a variable-speed induction motor drive through a gear box. The instantaneous shaft speed and torque is measured using an in-line torque transducer which is linked to a data acquisition system. A PXI-based data acquisition system communicates with the power analyzer and records the electrical and mechanical measurements. The LabView-based user interface software displays the results and controls the speed of the drive.

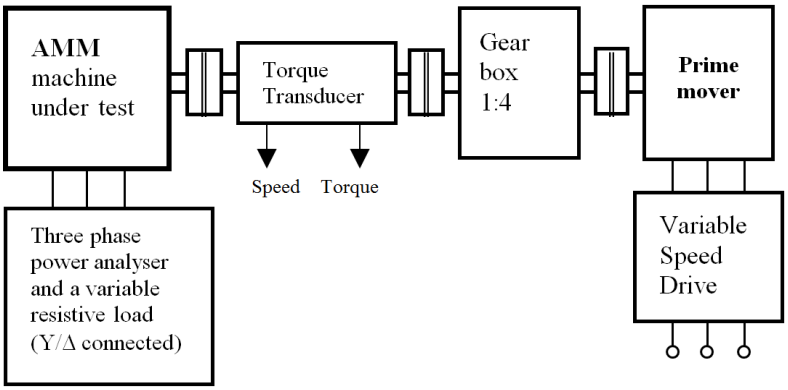

Figure 6.4 The block diagram of the test setup.

6.2.3 3D Finite Element Model

In this study, 3D-FE analysis is applied to model the machine using the JMAG software package [22]. The cross-section of the JMAG model showing the key sections of the tapered machine is given in Fig. 6.5, which includes the machine housing, rotor yoke, PM, air gap, copper stator windings and the AMM stator. This model was used to calculate the performance and loss separation under both rotating and also locked-rotor conditions.

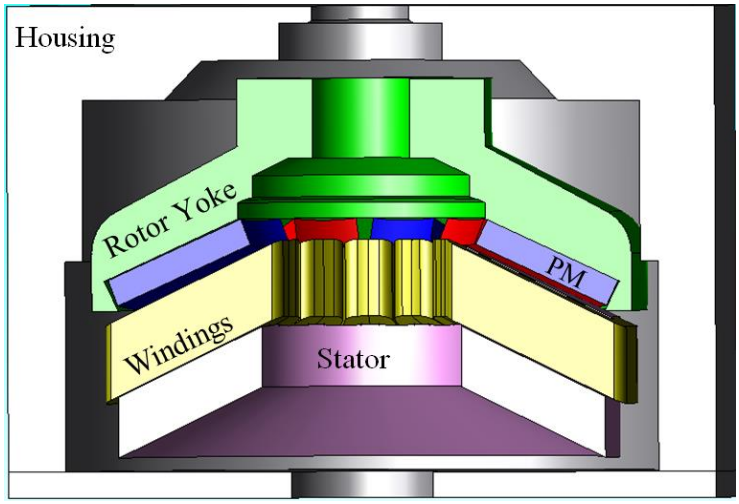

Figure 6.5 Cross-section of the baseline tapered AMM machine.

6.3 Mechanical Loss Analytical Estimation

The mechanical loss includes windage and bearing friction losses. The windage loss for a rotating disc can be given by [54]:

$$P_{Windage} = 0.5 c_f \rho_{air} \omega_M^3 (R_{RotOut}^5 - R_{shaft}^5) P_{Windage} \quad (6.1)$$

where ρ_{air} is the air density at one atmosphere and 20°C (1.2 kg/m^3), ω_M is the mechanical rotational speed in rad/s, R_{RotOut} is the outer radius of the rotor, R_{shaft} is the radius of the shaft, and c_f is the coefficient of drag for turbulent flow which can be calculated from:

$$c_f = \frac{3.87}{\sqrt{Re}} \quad (6.2)$$

where Re is the Reynolds number for a rotating disc and is given by

$$Re = \frac{\omega_M R_{RotOut}^2 \rho_{air}}{\eta_{air}} \tag{6.3}$$

where η_{air} is the dynamic viscosity of air at one atmosphere and 20°C (1.8×10^{-5} Pa.s). The bearing friction loss of a small machine can be estimated by

$$P_{Friction} = 0.03 k_{fb} (Rotor\ Mass + Shaft\ Mass) \frac{\omega_M}{\pi} \tag{6.4}$$

where k_{fb}=1 to 3m^2/s^2 for small bearings and the masses are given in kg. This equation only considers the radial force on the bearing due to the weight of the rotor and does not consider axial forces. It indicates that to a first approximation the bearing loss is proportional to radial force. The above equations show that windage power losses are proportional to the cube of speed while bearing losses are generally linearly proportional to speed.

This section describes tests using an uncut stator (see Fig. 6.6(a)) to estimate the mechanical loss. Since the stator slots are filled with epoxy in the cut stator, it would be expected to have a similar windage loss to the uncut stator. With the same principle as described in [48], by using the uncut stator the rotor loss is ideally reduced to zero as the rotor does not see any flux variation due to the slot openings and also the stator loss is substantially reduced. The stator loss has been estimated using a 3D-FE model with an uncut stator. By subtracting the uncut stator loss using FE from the measured loss, an accurate estimate of the mechanical loss can be obtained. The torque transducer offset was compensated using the process described in Section 5.5.

Fig. 6.6(b) shows that the uncut stator loss using FE is small as AMM has low iron loss characteristics and thus the estimated mechanical loss is similar to the measured input power with the uncut stator. It also emphasizes the linear relation of loss with speed due to the low windage losses which are estimated from (6.1) to only form 5% of the total loss at 7,000 rpm. It is interesting that the value of k_{fb} in (6.4) which corresponds to the measured results is a value of 3.6 which is not far from the typical range of 1 to 3. The slightly higher value is likely associated with the effect of axial loading on the bearings.

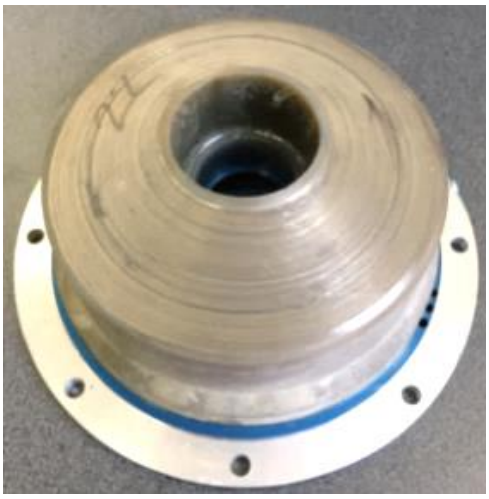

(a)

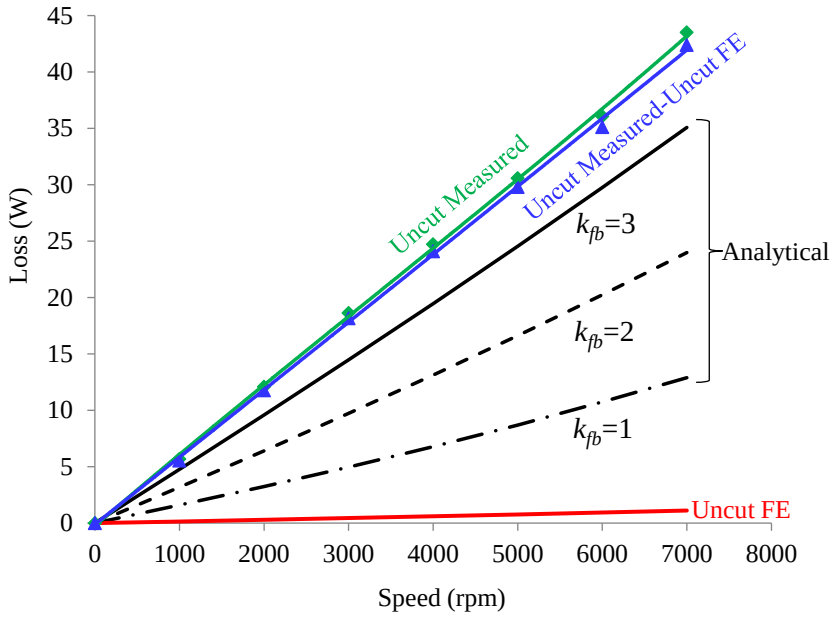

(b)

Figure 6.6 Mechanical loss, (a) Uncut AMM stator core, (b) Determining the mechanical loss versus speed using measurements and FE results with the uncut stator.

6.4 Open-Circuit Tests

Using the test setup given in Fig. 6.4, open-circuit measurements were performed by operating the machine as a generator and monitoring the terminal voltages (back emf), input torque and speed.

This section describes the process used to determine the actual airgap in the machine and the analysis of the open-circuit loss results.

6.4.1 Determining the Actual Airgap

A single flat magnet was used to create each pole of the baseline tapered rotor (Fig. 6.3). This results in a non-uniform air gap between the curved stator and the flat magnets. Fig. 6.7 shows that the minimum air gap length between the stator and magnets is at the centre of the poles while the maximum air gap is at the edge of the poles. There is also a non-uniform air gap between the flat magnets and the curved rotor yoke. Both air gaps are included in the 3D FE model.

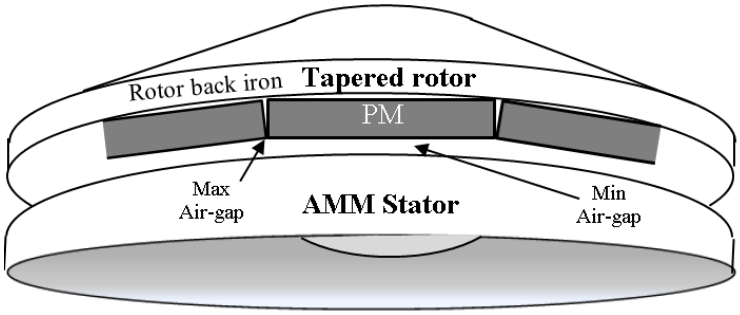

Figure 6.7 Non-uniform air gaps associated with the use of flat magnets with a tapered stator and rotor yoke.

Fig. 6.8 shows the air gaps between the magnet and the stator, the magnet and the rotor yoke, and the total airgap as the sum of the two. These are given as a function of radius from the inner to the outer diameter at three different angles with respect to the centreline of the magnets. The angles correspond to the middle of PMs (α=0°), edge (α=35.5°), and α=10°. It is concluded that the total air gap is not affected by angular position but increases with radius due to the difference between the taper angles of the stator and the rotor yoke.

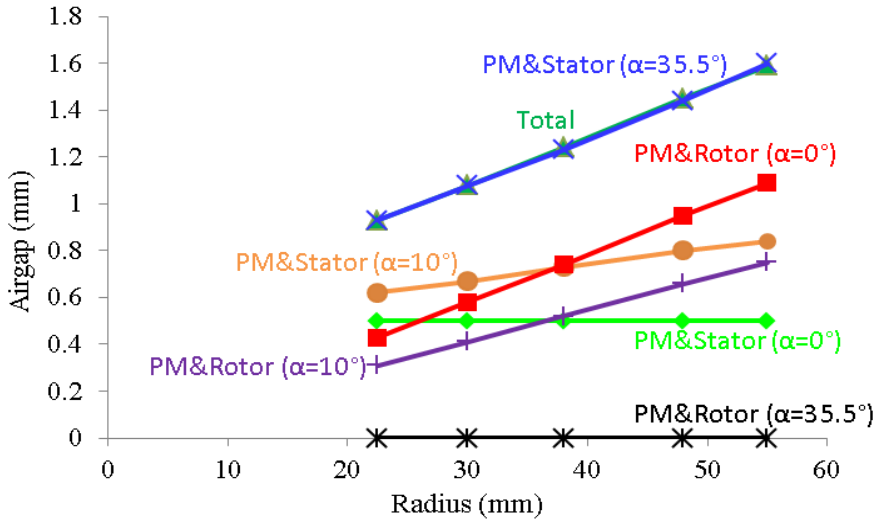

Figure 6.8 Air gap variations as a function of angle and radius.

The use of an air gap which varied with radial position was suggested in [55] to reduce the stator core loss. The air gap was increased at the inner radius to reduce stator saturation in this area. To compensate for the flux reduction, the permanent magnet thickness was increased. The results indicated an 8% reduction of the stator loss.

For the studied tapered machine, the rotor construction used resulted in an increased air-gap at the outer radius which reduces the rotor yoke flux density and rotor loss. The rotor loss has the highest value in the outer rotor ring and contains the largest portion of the iron loss. This issue will be explained more in Sections 6.6.2 and 6.6.3 when the rotor yoke loss and the effect of a uniform air-gap by using curved magnet are explained.

In the experimental test arrangement, the rotor axial position relative to the stator could be adjusting using a calibrated threaded screw. The “zero” air gap position was found by moving the rotor until it touched the stator. The screw was then used to shift the rotor axially 0.5mm to set the air gap. Effectively this sets the clearance between the rotor and stator as 0.5 mm. In practice the actual average air gap between the stator and the centre of the magnet poles will be generally larger than 0.5mm due to manufacturing irregularities.

The actual air gap was estimated by comparing the measured back-emf for three air gap lengths versus that predicted by the 3D FE model with the measured value of magnet remanent flux density. In Fig. 6.9(a) the blue diamonds show the measured values while the red squares show the FE calculated values. The figure shows a constant 0.5mm difference between the simulated and measured air gap values for the same back-emf voltage. That is the measured back-emf for a measured 0.5 mm air gap corresponds to the calculated back-emf for a 1 mm air gap. Thus it appears that the actual air gap is 0.5 mm greater than the measured value.

Fig. 6.9(b) shows a graph of back-emf versus speed for two air gap values comparing the measured and calculated results assuming a 0.5 mm difference between measured and actual air gaps. It shows a good correspondence.

The measured and simulated back-emf waveforms at 7,000 rpm are compared in Fig. 6.9(c) which also show the sinusoidal back-emf waveform shape is predicted accurately.

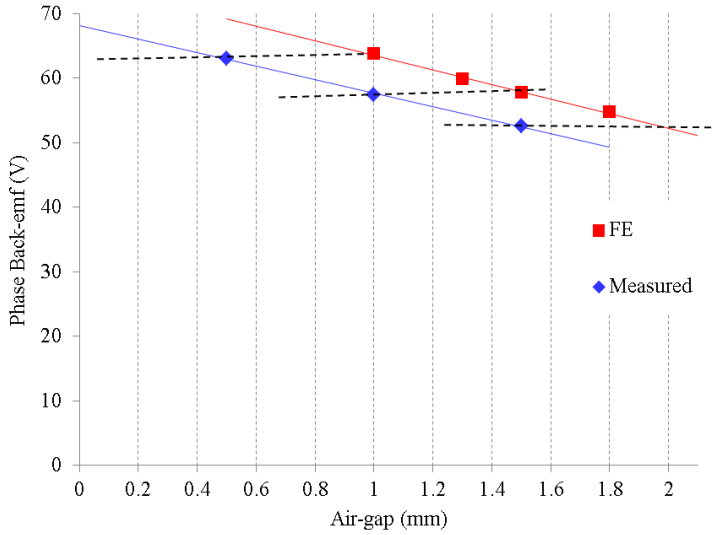

(a)

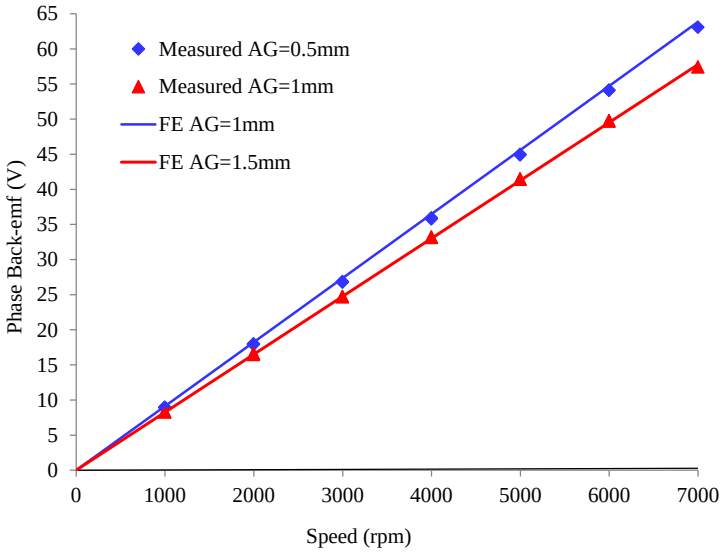

(b)

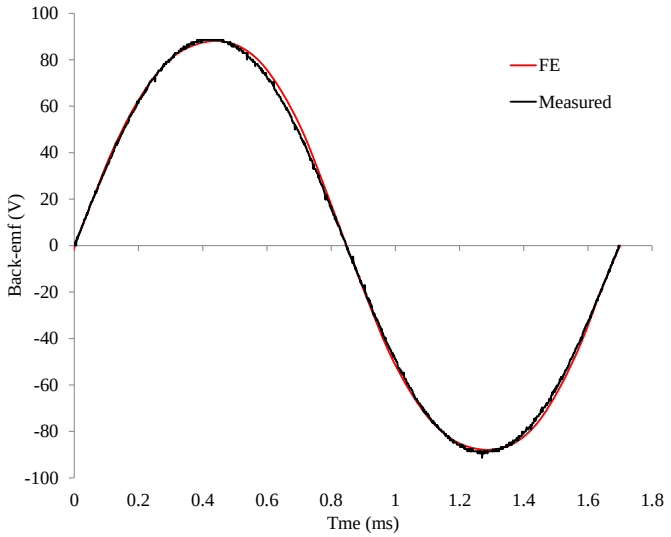

(c)

Figure 6.9 Air gap modeling and back-emf validation. Comparison of measured and calculated: (a) back-emf versus air gap at 7,000 rpm,(b) back-emf versus speed and, (c) back-emf waveforms at 7,000 rpm

6.4.2 Open-Circuit Loss Results

Fig. 6.10(a) shows the FE calculated open-circuit loss which does not include mechanical losses (red curve). Adding the measured mechanical losses obtained from the uncut stator test (see Fig. 6.6(a)) to the FE calculated curve gives a good correspondence to the measured open-circuit losses with the cut stator.

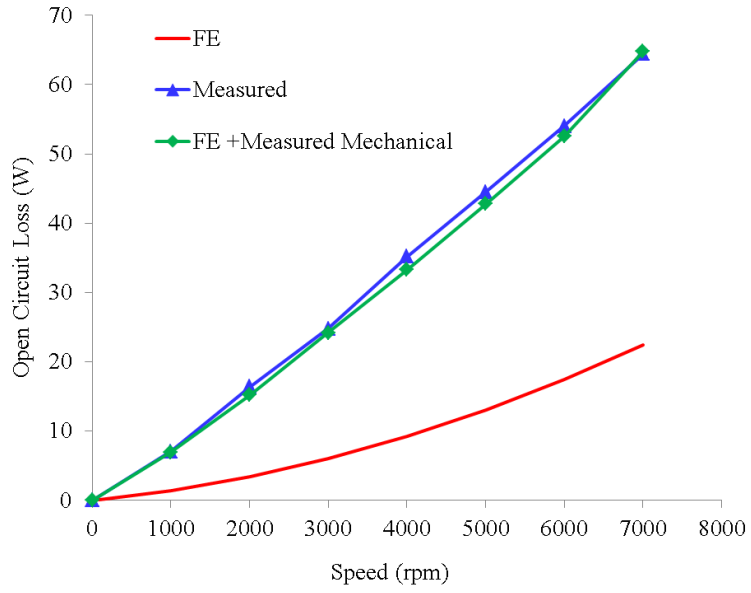

(a)

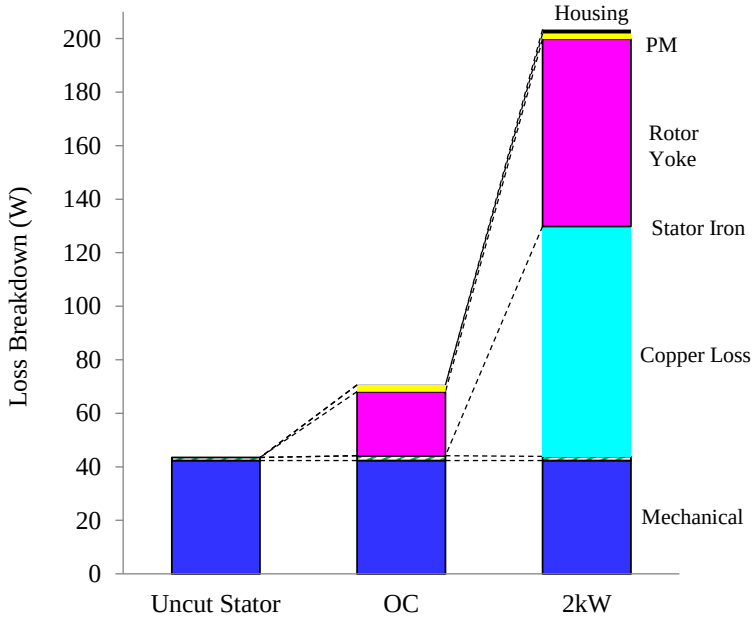

(b)

Figure 6.10 Loss analysis of baseline rotor: (a) open-circuit loss comparison as a function of speed,(b) calculated loss breakdowns at 7,000 rpm for uncut stator, open-circuit and full-load (2 kW) conditions.

The calculated loss breakdown at 7,000 rpm is presented in Fig. 6.10(b) for three cases: uncut stator, open-circuit and at full-load. With the uncut stator, the mechanical losses dominate. With the cut stator, under open-circuit conditions, the rotor losses are about half of the mechanical losses. The stator losses are relatively small due to the low loss characteristics of AMM. The full-load case is discussed in the following section.

6.5 Loading Tests

The loading test has been performed using the test set-up given in Fig. 6.4, where the machine is operated as a generator and loaded by a three-phase resistive/capacitive load.

Fig. 6.11(a) compares the measured and FE calculated efficiencies versus output power at 7,000 rpm. Without considering the impact of mechanical loss, the FE calculated efficiency is significantly higher than the measured results, particularly in the lower power range where the copper loss is low. Including the effect of mechanical loss brings the measured and simulated efficiencies to be much closer. At 2 kW output power, the measured efficiency was close to 90%.

The FE calculated loss breakdown at 2 kW was presented earlier in Fig. 6.10(b). The largest loss is the stator copper loss which accounts for 44% of the total loss. This is calculated using the stator winding resistance associated with the measured operating temperature of the winding.

The second largest loss is the rotor yoke losses which are about three times larger than in the open-circuit case. The open-circuit case has only rotor yoke losses associated with the magnets interacting with the stator slotting. It is significant in this machine due to the large stator slot openings associated with the open slot construction. The load case includes additional loss in the rotor yoke due to the stator MMF space harmonics created by the stator currents (armature reaction).

The total calculated losses associated with the stator iron, housing and PM were about 3%. The low PM loss compared to the rotor yoke losses is due to the use of bonded magnets whose resistivity is much higher than that of the rotor yoke.

Fig. 6.11(b) shows the measured efficiency versus output power at speeds from 3,000 rpm to 7,000 rpm. The maximum efficiency point for each speed is nearly 90% but the power at which this occurs, reduces with speed.

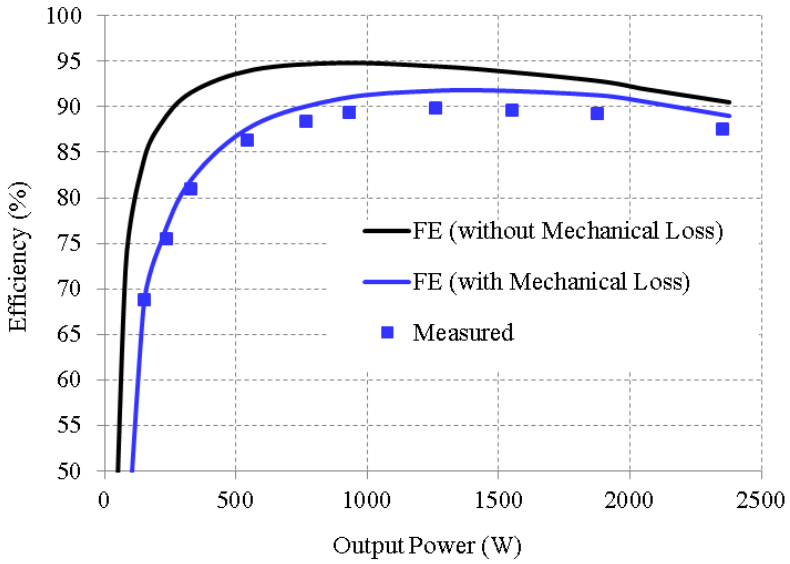

(a)

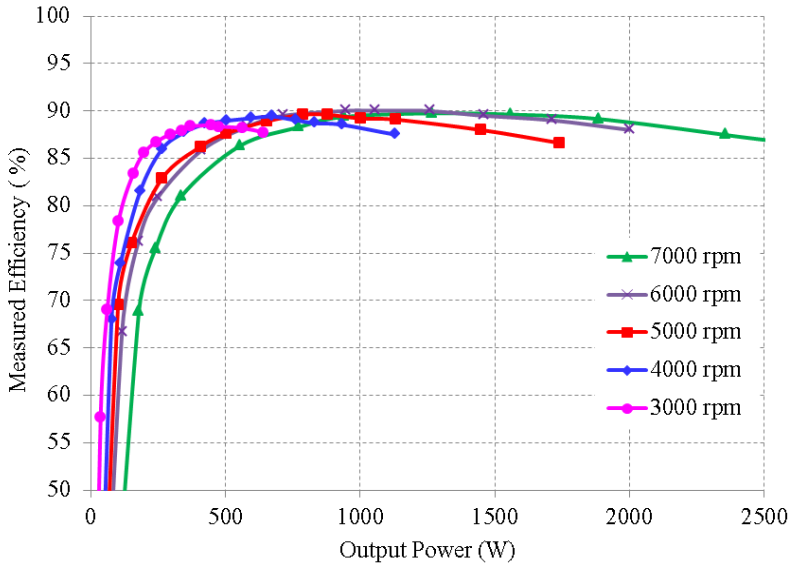

(b)

Figure 6.11 Efficiency versus output power: (a) measured and FE comparison at 7,000 rpm, (b) measured at speeds from 3,000 rpm to 7,000 rpm.

The latter observation can be explained as maximum efficiency generally occurs when for a given speed; the losses which vary with output power are roughly equal to the losses which do not vary with output power. For this machine, the most significant losses which vary with output power are the stator copper loss and the rotor yoke losses associated with armature reaction. Both of these are proportional to the square of

current. The most significant losses which do not vary with output power are the mechanical loss and the rotor yoke losses associated with stator slotting. As the losses which do not vary with output power, decrease with speed, thus the current and hence output power corresponding to maximum efficiency also reduces with speed.

6.6 Design Changes For Efficiency Improvement

The previous sections have examined accurate measurement and loss separation techniques for the tapered axial-field machine. This section examines three methods for improving its efficiency: increasing the air gap; reducing the air gap by using curved magnets; and modifying the rotor design.

6.6.1 Increasing the Air Gap

Increasing the air gap in the machine reduces the magnetic flux. This reduces the losses which do not vary with power, such as mechanical losses as it reduces the axial force, and rotor yoke losses associated with stator slotting due to the lower airgap flux density. However the reduced flux reduces the back-emf, and hence for the same output power, increases the stator current and hence copper losses. This increase in copper losses is only partly offset by the larger gap reducing the rotor losses associated with armature reaction.

Fig. 6.12 shows the effect of increasing the measured air gap in the machine from 0.5mm to 1mm. It was found that this reduces the measured back-emf and hence the magnetic flux in the machine by 10%.

The calculated open-circuit loss breakdown in Fig. 6.12(a) shows this reduces the mechanical losses by about 20% due to the lower axial force on the bearings which is proportional to the square of the flux density. The fact that the reduction in mechanical loss is the roughly the same as the reduction in axial force implies there may be a roughly linear variation between the two.

The rotor yoke losses reduce by 34% which is comparable to the reduction in the PM losses of 38%. These are more than just the square of the air gap flux density reduction expected from assuming them to be eddy-current related. This is likely related to the rotor losses due to stator slotting being strongly related to air gap length and not just air gap flux density.

Fig. 6.12(b) shows a comparison of the measured and calculated efficiency versus output power for the two air gap lengths at 7,000 rpm. Note the FE results include the extra 0.5 mm air gap that was found in Fig. 6.9 and hence what is stated as the 1mm FE results actually correspond to 1.5 mm.

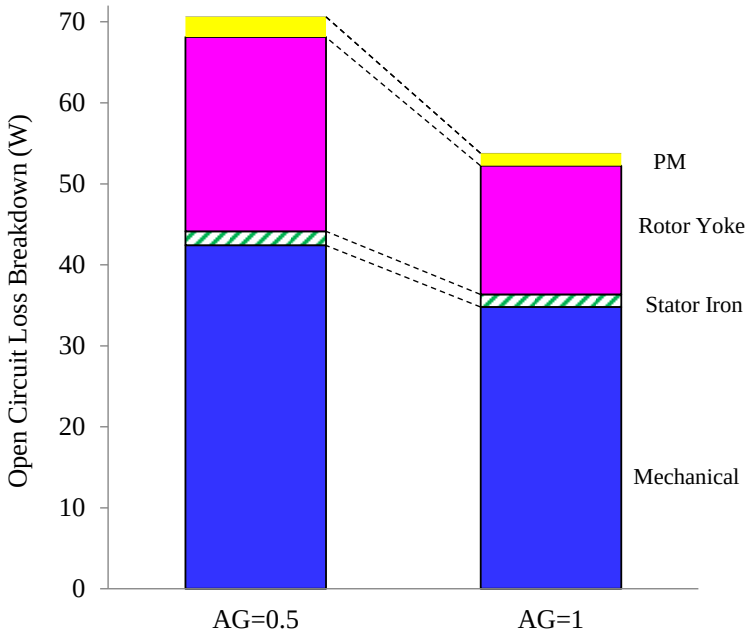

(a)

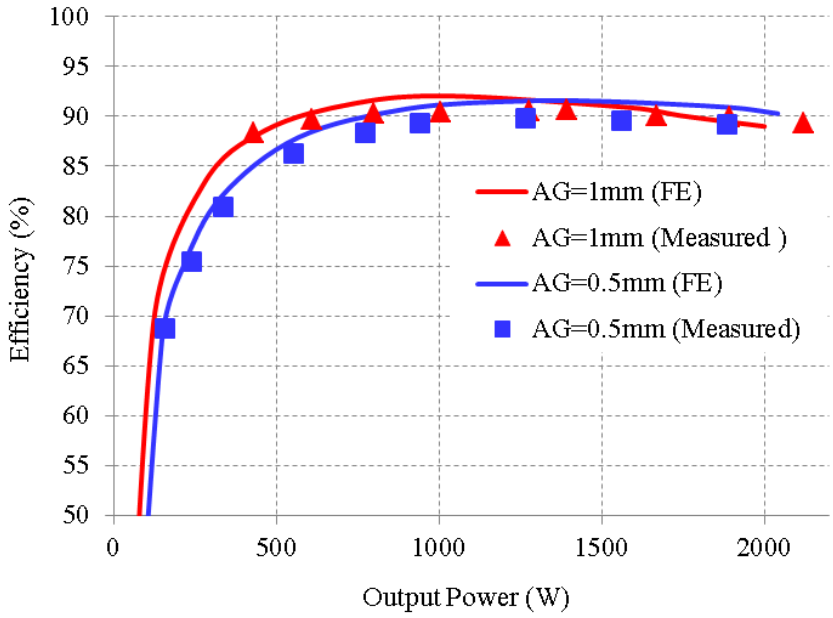

(b)

Figure 6.12 Performance comparison at air gaps of 0.5 mm and 1 mm: (a) Calculated open-circuit loss breakdown, (b) Measured and calculated efficiency versus power characteristics at 7,000 rpm.

Increasing the air gap reduces the losses which do not vary with output power and hence improves the efficiency at lower output powers. However the lower back-emf and

hence higher copper loss reduces the efficiency at higher output power. The cross-over point (equal efficiency) for the two air gap values occurs at about 1.3 kW for this machine. A full-load (2 kW) the efficiency with the larger gap length is about 2% lower.

The changes in the efficiency versus output power curve obtained by increasing the air gap (Fig. 6.12(b)) are similar to those found by reducing the speed (Fig. 6.11(b)). This is explained by the concept of losses which vary with output power and losses which do not and how both types of losses are affected by speed and air gap.

6.6.2 Effect of Using Curved Permanent Magnets

Figs. 6.3 and 6.8 showed that the tapered rotor was constructed using a flat PM segment for each magnet pole. This resulted in a non-uniform air gap both between the tapered stator and the flat magnets, but also between the flat magnets and tapered rotor yoke.

The effect of using curved magnets was considered. This results in a uniform air gap between the stator and magnet and an ideal zero air gap between the magnets and the rotor. The average air gap is thus much smaller. The key difficulty with curved magnets is the complexity of the tapered shape with regards to manufacturing which produces a considerable increase in cost.

For the 3D FE model, the same minimum air gap as the baseline rotor was assumed, that is 0.5 mm clearance plus 0.5mm extra gap giving a total of 1 mm.

The reduced average air gap produced a calculated increase in air gap flux density and hence back-emf of 15%. From Section 6.3 it was shown that the mechanical loss showed a roughly linear relationship with axial force and hence the estimated mechanical loss was obtained as roughly 30% larger than the baseline machine.

The calculated rotor yoke loss increased by a factor of 2.7 times with the curved magnets. This is much higher than simply the square of the air gap flux density increase which would have estimated a factor of 1.3 times. This is consistent with the observations in Section 6.4 that these losses are strongly related to air gap.

Fig. 6.13 examines the calculated effect of using curved versus flat magnets on the efficiency and losses versus output power at 7,000 rpm. Fig. 6.13(b) shows that using

curved magnets increases the losses which do not depend on output power but the higher back-emf reduces the stator current and hence those losses which do depend on output power. Note that the rotor losses contain both the stator slotting losses which ideally do not vary with output power and the armature reaction losses which do vary with output power.

Fig. 6.13(a) shows flat magnets have a higher calculated efficiency for output powers below about 1.7 kW and curved magnets have higher efficiency above this power.

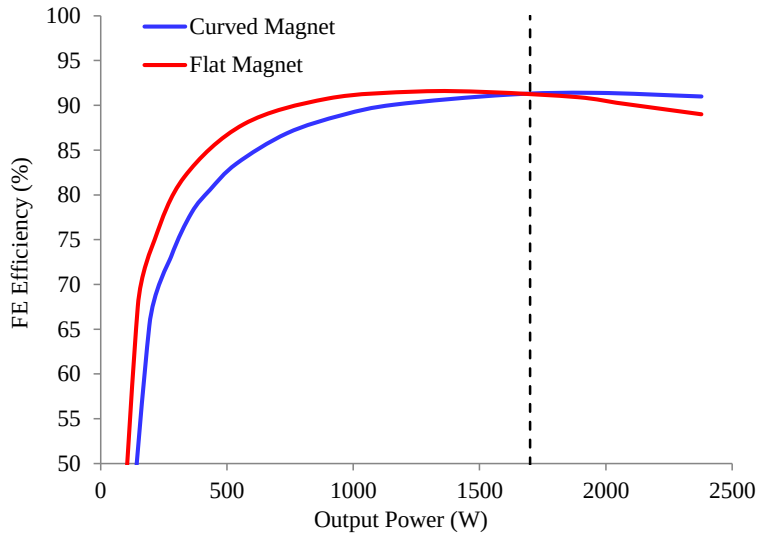

(a)

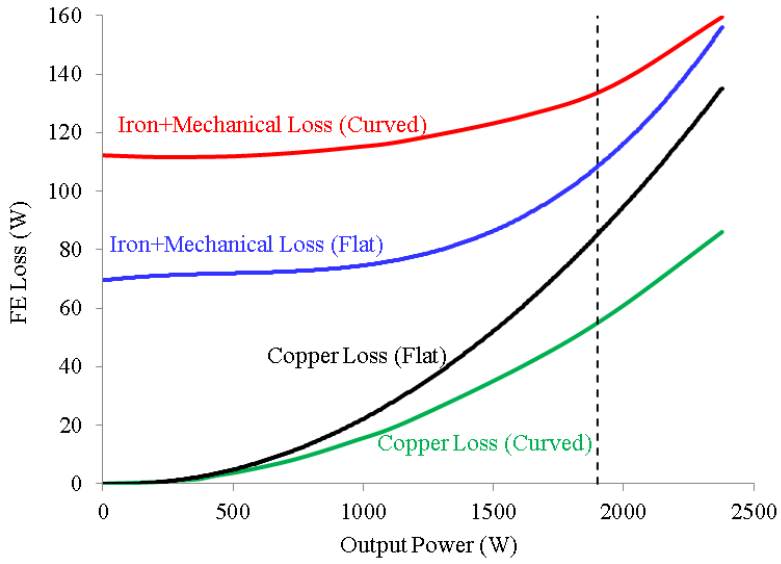

(b)

Figure 6.13 Calculated comparison of the machine performance utilising flat and curved magnets at 7,000 rpm, (a) efficiency, (b) losses.

6.6.3 Modifying the Rotor Yoke Design

Fig. 6.10(b) showed that the calculated rotor yoke losses formed about a quarter of the total full load losses and that roughly one third of the rotor yoke losses is due to stator slotting and two thirds due to stator armature reaction.

The losses due to stator slotting are associated with the large slot openings associated with the open-slot design. These could be reduced by using methods such as magnetic slot wedges.

The losses associated with armature reaction are due to stator winding air gap space harmonics moving asynchronously with the rotor, producing eddy-current losses. They are particularly high in fractional-slot machines [56]. These sub-harmonics have a long spatial wavelength and as a result their corresponding flux lines enter deep in to the rotor yoke.

Fig. 6.14(a) shows the calculated magnetic flux density contour plot of the baseline rotor at full load at 7,000 rpm. The baseline rotor has a relatively wide rotor yoke overhang on the outer diameter which is used to retain the magnets. It shows there are high values of peak flux density in this overhang which would result in high iron losses in this area. It also shows the variation in flux density across the magnet pole associated with stator slotting and armature reaction.

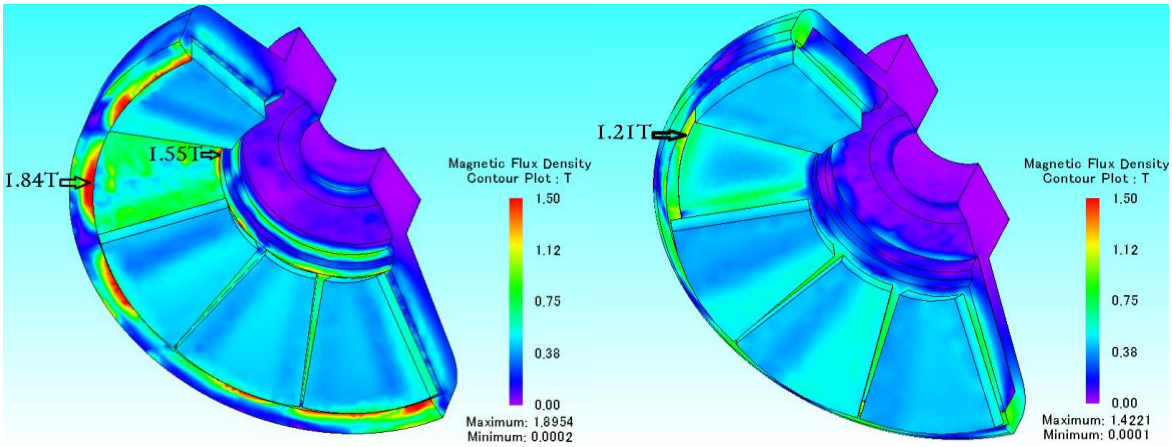

(a) (b)

Figure 6.14 FE calculated magnetic flux density of the rotor under full load at 7,000 rpm for a particular rotor position, (a) baseline rotor, (b) new rotor.

Figure 6.15 The modified rotor.

To reduce the rotor losses, the rotor design was modified by firstly changing the rotor back-iron to a material with a lower eddy-current loss and secondly reducing the thickness of the overhang of the rotor back-iron and reducing its proximity to the air gap. The new rotor design is shown in Fig. 6.14(b) and Fig. 6.15.

The FE results showed that the back-emf magnitude was comparable between the baseline and new rotor. The rotor losses reduced substantially due to the reduction in flux density in the outer edge of the rotor and the reduced losses in the rotor yoke.

The new rotor design was constructed and tested with the baseline stator. Fig. 6.17(a) compares the open-circuit losses of the machine using the baseline rotor (blue) and the new rotor (red). The FE results without mechanical loss (dashed lines) show the losses of the new rotor are dramatically reduced and are less than a quarter of that of the baseline rotor at 7,000 rpm.

The mechanical loss of the machine with the new rotor design was measured with the uncut stator using the approach shown for the baseline rotor in Fig. 6.6(a). An 8% increase in mechanical loss was found which is related to a corresponding increase in the calculated radial force.

The total estimated loss (solid lines) based on the sum of the FE calculated losses and measured mechanical losses were found to be in good agreement with the measured loss (symbols).

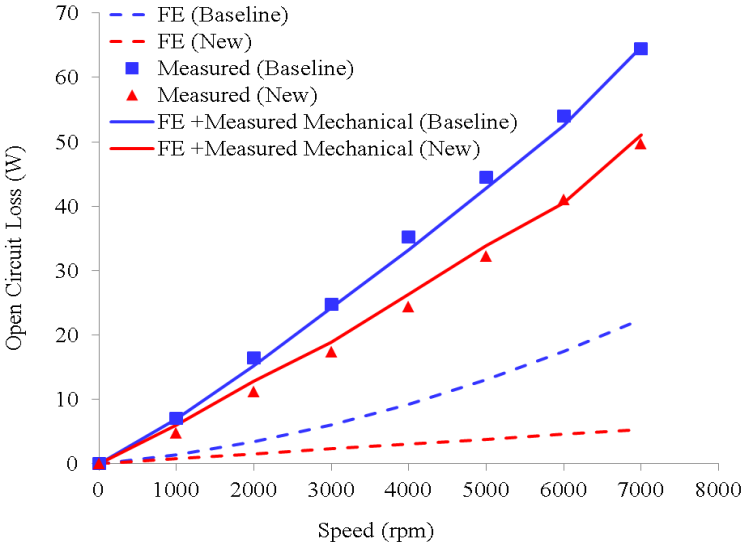

(a)

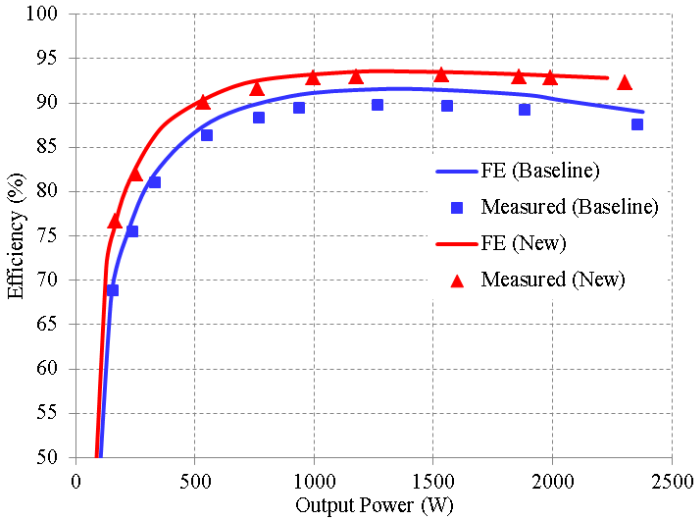

(b)

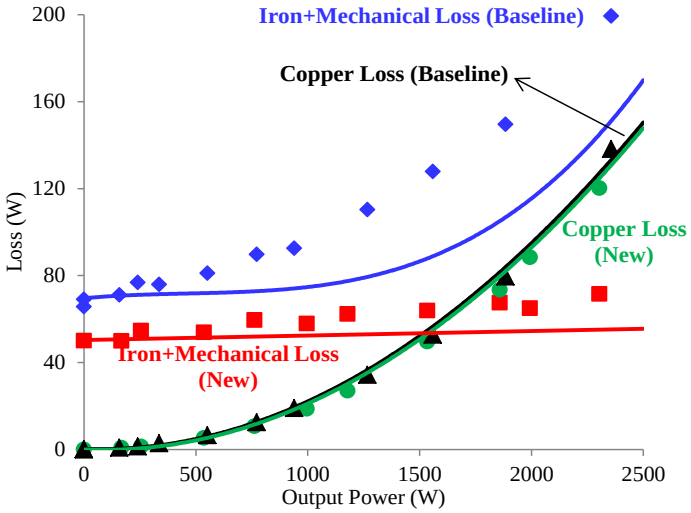

(c)

Figure 6.16 Comparison of the performance of the baseline and new rotor: (a) open-circuit losses, (b) efficiency characteristics, and (c) loss components.

Fig. 6.17(b) shows both the measured and the calculated efficiency versus output power using the baseline and the new rotor configurations. The results demonstrate a significant 3.5% measured efficiency improvement at 2 kW output.

Fig. 6.17(c) compares the measured and the FE results of the copper and non-copper loss components of the rotor configurations. As the back-emf is comparable, thus the copper loss is similar for the two rotors however the rotor losses are considerably lower.

6.7 Locked-Rotor Test

A challenge in experimentally comparing the rotor losses of the baseline and new rotors is the uncertainty about the mechanical losses during the rotating tests. This section proposes a novel means of validating the finite-element rotor loss model using locked-rotor tests which avoid the issue of mechanical losses. The key point here is rotor loss model validation as the locked-rotor rotor losses are generally not the same as those under rotating operation.

Though locked-rotor tests have been reported previously [57, 58], the novelty here is associated with applying it to separate the rotor loss components. The method used is as follows: simulations and experimental testing are done on the machine with a three-phase, high-frequency AC excitation under locked-rotor conditions. The input power is measured as a function of stator current. The non-copper losses (stator iron, rotor magnet and rotor yoke) are determined by subtracting the copper loss (I^2R) using the measured stator resistance taking into account the actual stator temperature found with a thermocouple.

In the testing, a California Instruments programmable power supply was used to produce the AC sinusoidal source voltage at about 583 Hz (corresponding to 7,000 rpm rotational speed).

Three locked-rotor cases are considered in the simulations and experiments which are the stator: without rotor, with baseline rotor and with new rotor. The case without the rotor gives the locked-rotor stator losses only. Taking the difference of this with the case with the rotor gives an estimate of the locked-rotor rotor losses. A good correlation between the measured and FE predictions for the locked-rotor rotor loss validates the

accuracy of the FE rotor loss model and hence its ability to predict the rotor losses under rotating operation.

Fig. 6.18(a) compares the FE and measured non-copper loss for the three cases as a function of stator current. The good correspondence between the measured and calculated stator losses without a rotor (black curve) validates the calculated low stator losses due to the use of AMM.

The baseline rotor (blue curve) shows a substantial calculated locked-rotor rotor loss while the new rotor has a much lower locked-rotor rotor loss. The good correspondence between the experimental and calculated locked-rotor results gives confidence in the FE rotor loss model.

Fig. 6.18(b) shows a comparison of the calculated loss breakdowns for the baseline and new rotor for three cases: locked rotor at rated current, open circuit and full load at rated current. The rotating tests include the measured mechanical loss which adds an uncertainty factor. Based on the uncut stator test, the mechanical loss is slightly higher (8%) with the new rotor. In the open-circuit tests, the high proportion of mechanical losses make it harder to accurately validate the reduction in rotor losses.

With a similar back-emf and the same stator, the two machines have similar full-load copper loss. For the machine considered, the rotor losses under full-load conditions appear to be roughly the sum of the rotor losses due to armature reaction which is found in the locked-rotor condition, and the rotor losses due to stator slotting which is found in the open-circuit condition.

This has shown the locked-rotor test with and without rotor is a useful means to check the accuracy of the FE rotor loss model without sensitivity to mechanical losses.

6.8 Conclusions

This chapter described a tapered-field topology for AMM machines which is suitable for waterjet cutting. It has a rigid structure suitable for high speed operation and offers the potential for high output torque for a given outer diameter.

The main benefit of the proposed tapered machine design is to allow convenient manufacturing with AMM to seek to utilize its potential for low stator iron loss.

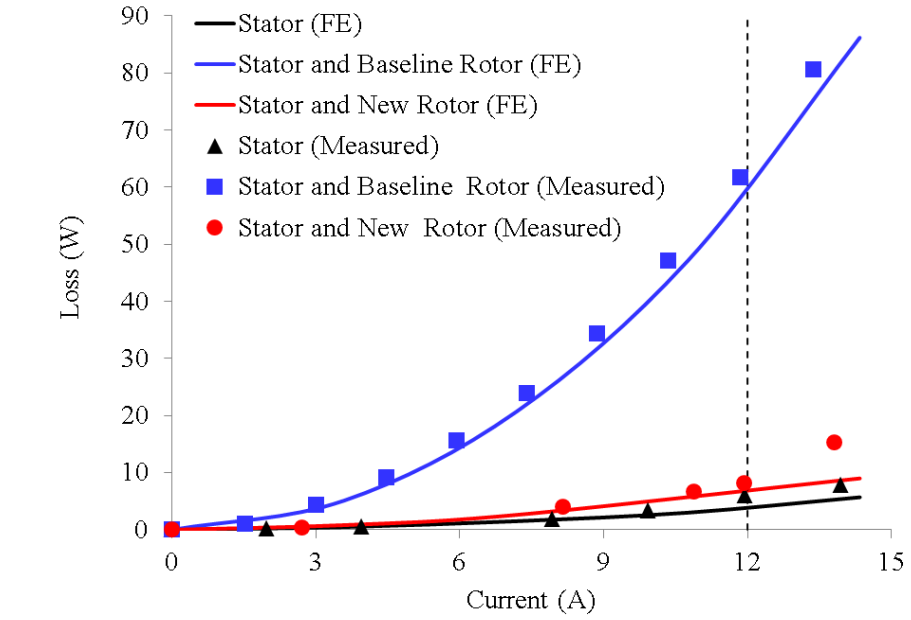

(a)

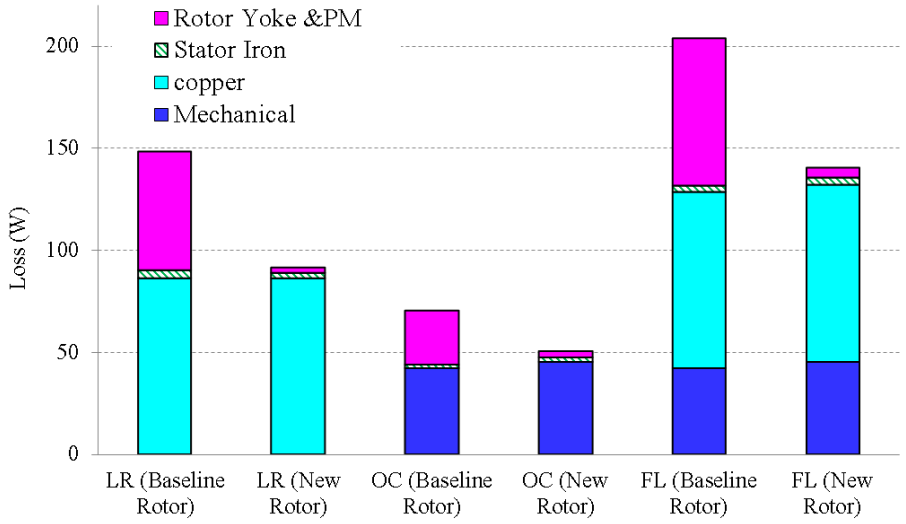

(b)

Figure 6.17 Loss analysis of the baseline and new rotors at 7,000 rpm: (a) locked-rotor FE and test results and (b) calculated locked-rotor (LR), open-circuit (OC), and full load (FL) test results.

Otherwise its performance in terms of quantities such as efficiency and torque/unit mass is expected to be comparable to an axial-field machine with similar airgap area and magnet volume. The tapered design does allow a larger airgap area for the same outer diameter but also has a longer axial length.

A demonstration machine with a 25° tapered open-slot stator core was analysed with 3D finite element software. It was constructed to validate the proposed manufacturing approach and to obtain the electrical characteristics. The prototype machine used standard 30mm width AMM ribbon and was cut using a precision

waterjet cutting technology. This prototype also allowed investigating the accuracy of cutting and the major loss components in the machine.

A novel method was described to estimate the mechanical loss of the tapered machines using rotating tests with an uncut stator combined with FE modelling to subtract the stator iron loss. For the machine considered, the mechanical loss appeared to be largely due to bearing loss. From tests with different air gaps, the bearing loss appeared to be roughly proportional to the axial force.

Open-circuit FE and test results showed that the major loss component in this condition in the machine was mechanical loss (67%) followed by rotor yoke losses (27%).

Three design optimizations were considered: increasing the air gap, using curved instead of flat magnets, and modifying the rotor yoke design. Increasing the air gap improved the efficiency at light loads but reduced it at full-load. The impact of using curved magnets was similar to that of reducing the total air gap.

The most important result was associated with modifying the rotor yoke by using a material with lower eddy-current loss and reducing the rotor edge overhangs. Together, these improved the measured efficiency to 93.5% from 90%.

Finally, a novel locked-rotor test method was used to validate the FE stator and rotor loss modelling, while not being sensitive to mechanical losses. The locked-rotor test without the rotor confirmed the low stator iron losses which would be expected from its amorphous magnetic material (AMM) construction. The locked-rotor tests with the baseline and optimized rotors validated the FE predictions of a substantial reduction of rotor losses. Thus the locked-rotor test was shown to be a useful tool in verifying the loss breakdown of synchronous machines.

In future work, further optimisation of the machine to reduce stator copper and mechanical losses could be performed.

Chapter 7 : Conclusion and Future Work

This research covers two separate permanent-magnet machines: an interior radial-flux machine used in as AC portable generator and an axial-flux machine utilising amorphous magnetic material as the stator core. The key results and major contributions resulting from these research works as well as the suggestions for the future works are presented in this chapter.

7.1 Spoke-Type IPM Generators

PM generators (PMG) are a promising substitute for portable wound-field synchronous generators due to their potential for higher efficiency, reduced size and weight, no requirement for field excitation, higher reliability and lower maintenance. For portable generators it is essential that machine meets the requirements of ±5% voltage regulation, sinusoidal output voltage waveforms, high efficiency and good transient performance. However, voltage regulation is a concern with PMGs due to their lack of excitation control. From a cost perspective it is useful that a PM portable generator does not need any power electronics control or output power processing. In addition, the three-phase voltages should be well balanced especially when driving induction machines to minimize negative sequence currents and hence preventing overheating of such machines. Therefore a portable PMG that fulfills the mentioned requirements is desirable. The principal aim of this work was to analyse the performance of a novel 16 kW, four-pole spoke-type IPM generator developed by the industry partner for this application.

7.1.1 Summary

7.1.1.1 3-Phase Loading

The performance of a novel 16 kW, four-pole spoke-type IPM generator (IPMG) under balanced resistive-inductive load was analyzed using an equivalent circuit and the phasor diagram. The time-stepping transient 2D finite-element simulation was used to model the machine. All the simulation and analytical results were validated using the test results of the prototyped machine developed by the industrial partner.

The inductance results indicated the stator has a high level of saturation even under open-circuit conditions which improves the voltage regulation. The calculated flux-linkage showed additional cross-saturation at the rated output condition which was expected from the high degree of saturation in the machine. The machine did not show much saliency at higher values of current and so the reluctance torque for this machine is small.

The calculated results considering the effect of stator resistance and saturation indicated saturation reduces the effect of the stator current on the flux-linkage and hence output voltage. This implies that designing a PM machine which has low saliency with a

significant degree of stator saturation improves its voltage regulation (though this may increase the iron losses). It was also concluded that voltage regulation for light loads is more sensitive to resistance than saturation, while the effect of saturation is more pronounced at higher loads.

The FE calculated and measured THD of the line and phase voltages showed a large triplen harmonic component in the phase voltage which increased with load. In the line voltage, the triplen harmonics were not present and the amplitude of most of the other odd harmonics and hence the THD reduced with load, resulting in the excellent THD of about 1% in the rated condition. Saturation was found to have little effect on the efficiency versus output power characteristics.

A comparison of the test results of a baseline wound-field synchronous generator with the studied IPMG with the same diesel prime mover showed the IPM generator has a higher measured rated efficiency (94%) compared to the wound-field unit (88%). This resulted in a 8.6% reduction in the measured prime mover fuel consumption. The IPM generator also showed improved transient output voltage response.

7.1.1.2 Single-Phase Loading Behavior

As it is a common practice for 3-phase portable generators to energize single-phase (1-ph) loads, in the next stage of the research the performance of the studied IPM generator when driving 1-phase loads without the use of any power electronics was considered.

An analytical procedure was developed for single-phase operation and to analytically calculate the voltages of the three phases under unbalanced conditions it was necessary to find the self and mutual inductances.

The effects of three different 1-ph winding configurations: the standard star-connection, delta connection and also a proposed new connection called open-delta connection with higher output power were considered. The results for these connections can be generalized for all permanent-magnet machines as the studied machine was a case study and can be used as a guideline for application of 3-ph generators for 1-ph applications. The effect of different winding configurations on the voltage regulation of the loaded phase was compared with the 3-phase condition.

The results indicated that 3-phase loading had the highest calculated voltage regulation of 5.5% followed by single phase star and open-delta connections (both had about 4% voltage regulation). The delta connection had the lowest voltage regulation of 3%.

The THD results indicated that the 3-ph star connected load had the lowest THD of all the winding configurations and for 1-phase loads, the delta connection showed about 3% lower THD than the star connection at all load points. The open-delta connection has the lowest calculated THD for all of the single-phase connections for output powers greater than 3 kW.

The FE calculated and measured losses as well as efficiency comparison for the three-phase and single-phase loading at the rated speed were presented. For the 3-phase case, the FE results indicated the machine has an efficiency of 94% under the rated condition. For the single-phase star connection at rated 1-ph output (5.3 kW), the machine had a calculated efficiency of about 89%. The delta connection had a 0.4% lower efficiency than the star connection due to the extra copper loss. The open-delta connection has an efficiency roughly mid-way between the 1-ph and 3-ph star connections.

The FE calculated instantaneous input torque waveforms at rated output power under both three-phase and single-phase loading were also presented. The three-phase operation produces a relatively smooth input torque which only has a small 6^{th} harmonic. For single-phase loading, there is the expected large second-harmonic torque component. The average of the input torque is approximately one-third of the 3-phase loading case where this value was 8% and 14% higher for the delta and open delta connection, respectively.

7.1.1.3 Performance as a Motor

The performance of the studied cage-less IPM machine developed for a portable generator application was examined when run as a motor under open-loop volts-per-hertz control from an inverter by using analytical and measured results.

The possibility of demagnetization due to stator currents and magnet temperature were studied using FE analysis. The local and global demagnetization possibilities were carefully examined and the results indicated this machine has high tolerance against

global demagnetization and can tolerate up to 350 A current in the negative *d*-axis at 50°C. However, the current corresponding to the start of local demagnetization was about 160 A at the same temperature. The high demagnetization withstand capacity is due to the combination of the flux-concentrating spoke-type topology and the twin magnets in each rotor pole. The effect of temperature on the demagnetization indicated the limit of 245°C and 120°C for global and local demagnetization, respectively.

The simplified equivalent circuit and equations were used to predict the motor input current and power-factor as a function of output power. The results indicated that below the rated output power, the machine is more efficient as a generator while above rated output power; the machine is more efficient as a motor. The maximum generating efficiency was about 94% while the maximum motoring efficiency was slightly lower at 93%.

The machine was capable of running with more than three times of its rated generator power under motoring operation. While it is not possible to run at this output power continuously due to the high stator currents (around 80 Arms), this indicates the machine has a high transient overload capability which is particularly useful in open-loop operation. The machine was also tested starting with loads more than twice of the rated generating power at rated speed. The motor was found to operate stably and reliably.

7.1.2 Original Contributions

This research included examining the performance of a 3-phase 4-pole stand-alone portable interior permanent-magnet AC generator under 3-phase and 1-phase loads. The performance of the same machine when run as a motor under open-loop volts-per-hertz control from an inverter was also studied. The original contributions include the following.

1. Effect of design parameters including saliency, stator resistance, and also saturation on the voltage regulation, THD, and efficiency.
2. Comparing the efficiency, fuel consumption, and transient response of the studied IPMG with a similar size wound-field generator with the same diesel prime mover.
3. Analyzing the performance of the three-phase IPMG under single-phase operation by proposing an analytical procedure and comparing voltage regulation, THD, and

efficiency results.

4. Proposing a new connection method called open-delta for single-phase operation and also considering a delta connection (which has not used commonly for single-phase operation) and comparing the results with 1-ph and 3-phase star connections. The results for these connections can be generalized for all permanent-magnet machines for the application of 3-ph generators for 1-ph operations.
5. Studying the steady-state and dynamic performance of the machine when run as a motor under open-loop operation as well as its overload capability.
6. Detailed finite-element analysis for demagnetization withstands capacity of the machine as a motor.

7.1.3 Future Work

The research areas that can be addressed in future studies are:

1. Parallel operation: it is often preferable to have two or more smaller generating sets operating in parallel rather than a single larger unit as smaller units are easier to transport. It also allows one of the units to be stopped at light loads which can significantly improve the fuel efficiency. Parallel operation enables easier maintenance, system expansion and improved reliability based on the ability to have a level of spinning reserve or redundancy. The parallel performance of the proposed permanent-magnet generator needs to be studied.
2. Loads with low power factor: the standards for general power supplies and the requirements for grid connection state that AC generators must be able to work at a minimum power factor of 0.9. Due to the fact that until now, there has not been any commercially available PMG suitable for the replacement of wound rotor alternators, the performance of the machine with low power factor loads needs further study.

7.2 Axial-Flux PM Amorphous Magnetic Material Machine

This research work has focused on the loss analysis of two single-sided axial-flux permanent-magnet machines using flat and tapered topologies. The capability of Amorphous Magnetic Material (AMM) ribbons for the application in permanent-magnet machines for high speed and industrial scale manufacturing was considered. The AMM cutting technique was developed by the industrial partner. This study provided detailed and precise measurement steps for successful loss analysis of the axial-flux permanent-magnet machines.

7.2.1 Summary

7.2.1.1 Materials Testing, Test Set-Up and Simulation

To provide a detailed loss analysis, it is essential that the magnetic properties of the materials are confirmed and the test set-up has been calibrated. As a result, the magnetic properties and iron loss characteristics of the three stator cores: grain-oriented silicon iron (GO-SI), soft magnetic composite (SMC), and AMM, were measured using non-slotted ring core samples for a wide range of operating frequencies. This confirmed the low iron loss characteristic of the AMM as well as the manufacturer's data. The bonded NdFeB magnets were also subjected to testing where the residual flux density was estimated using a combination of measurements and FE simulation. The torque meter was calibrated and the results indicated the necessity for correction of two types of offset errors.

3D finite-element analysis was used to predict performance accurately where different models where developed for the flat and tapered machines using the JMAG software.

7.2.1.2 Loss Analysis

A combined method including measurement and simulation was developed to accurately estimate the mechanical loss of the axial-flux permanent-magnet machines. It includes measuring the power loss when the stator is installed reversed to the rotor so to provide the rotor with an unslotted stator surface and subtracting the stator iron loss predicted by FE analysis from the measured values. The accuracy of the method was

confirmed using the tests on the SMC and SI cores. For the considered machine, the mechanical loss was largely due to bearing loss.

The open-circuit test result indicated the mechanical loss consisted of approximately half of the loss while and the FE loss breakdown showed substantial rotor loss due to the open stator slots. The low PM loss compared to the rotor yoke losses is due to the use of bonded magnets. The simulated generating efficiencies of the AMM, GO-SI, and SMC machines were found to about 91%, 90% and 87% respectively under the rated load of 1.5 kW at 5000 rpm and showed a good correspondence with the measured results.

7.2.1.3 The Advantage of Changing the Design from a Flat to a Tapered Machine Topology

The process of making an AMM stator core in the flat machine included winding the unannealed and uncoated AMM ribbon to a flat disc. Then using a special jig, the AMM core was pushed outward to obtain a tapered shaped disc which allows sufficient clearance for abrasive waterjet cutting of the slots. After the cutting process, the tapered stator is pushed back to the flat shape to obtain the original axial flux machine topology. In such a process the AMM core experiences a significant level of stress which may result in increased iron loss. In addition, to allow pushing back, the AMM ribbons cannot be wound too tightly which causes a low iron stacking factor. Also in the push back step, the slots may become asymmetric. Therefore, the flat AMM machine is not a good option for mass production.

In the next step a tapered-field topology for AMM machines which is suitable for waterjet cutting was introduced. It has a rigid structure suitable for high speed operation and offers the potential for high output torque for a given outer diameter. The main benefit of the proposed tapered machine design is to allow convenient manufacturing with AMM to utilize its potential for low stator iron loss at high frequencies. In addition, the tapered design allows a larger airgap area and torque density for the same outer diameter but also has a longer axial length. The demonstrated machine with a 25° tapered open-slot stator core was analysed with 3D finite element software.

7.2.1.4 Analysis of the Tapered Machine

Using a similar approach to the flat machine, the mechanical loss of the tapered machine was obtained. However, due to the tapered shape of the machine, installing the stator backward to the rotor was not possible so, an uncut tapered stator was used instead.

Using single flat magnets to create the poles of the tapered rotor resulted in a non-uniform air gap between the flat magnets and curved stator well as between the magnets and the curved rotor yoke. The actual air gap was estimated by comparing the measured and simulated back-emf values for three air gap lengths which indicated that the actual airgap was 0.5 mm greater than the measured values.

Similar to the flat machine, the full load test showed that the largest loss was the stator copper loss and the second largest loss was the rotor yoke losses which were about three times larger than in the open-circuit case. The rotor yoke loss in the open-circuit condition is due to the stator slotting and in the loaded condition there is an additional loss due to the MMF space harmonics caused by armature reaction. The total losses associated with the stator iron, housing and PM were about 3%. At 2 kW output power the measured efficiency was close to 90%.

7.2.1.5 Design Modifications

In the next step, three methods for improving the machine efficiency were considered: increasing the air gap, using curved magnets; and modifying the rotor design.

By increasing the air gap in the machine the rotor yoke loss, mechanical loss, and PM loss reduced. However the reduced flux reduces the back-emf, and hence for the same output power increases the stator current and hence copper losses. Therefore, efficiency improved at the lighter loads but reduced at higher loads with the cross-over point for the two air gap values occurring at about 1.3 kW for this machine. Using curved magnets reduced the average air gap and increased the air gap flux density hence both the back-emf and the rotor yoke loss. As the mechanical loss varied roughly linearly with axial force, it was roughly 30% larger than the baseline machine. The curved magnets provide higher efficiency for larger loads with the cross-over point at 1.7 kW power.

The most important design option was modifying the rotor design. The simulation

results showed that the baseline rotor yoke has a high peak flux density in the outer edge which resulted in high iron losses in this area. To reduce the rotor losses, the rotor design was modified by firstly changing the rotor back-iron to a material with a lower eddy-current loss and secondly reducing the thickness of the overhang of the rotor back-iron and reducing its proximity to the air gap. The final design showed the rotor losses reduced substantially while the mechanical loss of the machine with the new rotor design was increased by 8%. Both the measured and the calculated efficiency versus output power using the baseline and the new rotor configurations demonstrated a significant 3.5% measured efficiency improvement at 2 kW output.

7.2.1.6 Locked Rotor Test

Finally, a novel means of validating the finite-element loss analysis model was proposed using locked-rotor (stationary) tests which avoids the issue of mechanical losses. The method included the simulations and experimental testing on the machine with a three-phase, high-frequency AC excitation under locked-rotor conditions. Three locked-rotor cases are considered in the simulations and experiments including using the stator: without rotor, with baseline rotor and with new rotor. The case without the rotor gives the locked-rotor stator losses only. Taking the difference of this with the case with the rotor gives an estimate of the locked-rotor rotor losses. A good correlation between the measured and FE predictions validated the accuracy of the FE rotor loss model and hence its ability to predict the rotor losses under rotating operation.

7.2.2 Original Contributions

The major research contributions developed on the 12-slots 10-pole amorphous magnetic material machines with both flat and tapered topologies can be summarized as followings:

1. Developing a method to accurately estimate the mechanical loss using a combination of the measurement and FE simulation.
2. Detailed loss breakdown under no load and full load conditions.
3. Design modification and successfully achieving efficiency improvement to 93.5% from 90%.
4. Introducing a novel locked-rotor test method to confirm the loss analysis and accuracy of FE results by removing the uncertainty associated with mechanical losses. This method can be used in verifying the loss breakdown of any

synchronous machines.

7.2.3 Future Work

This research work concentrated on the loss analysis and efficiency improvement of the flat and tapered axial-flux permanent-magnet machines with special attention to the use of AMM. The research areas that can be addressed in the future studies are:

1. Rotor yoke design optimization to have lower weight to reduce the mechanical loss.
2. Thermal modelling of the machine to ensure acceptable temperature rises during long operation of the machine.

References

[1] International Energy Agency, “Key World Energy Statistics”, 2017. Available: https://www.iea.org/. [Accessed: 29-Sep-2017].

[2] "Australian Standard AS 2790 – 1989, Electricity Generating Sets – Transportable (up to 25kW)," 1989.

[3] R. Hasegawa, "Present status of amorphous soft magnetic alloys," *Journal of Magnetism and Magnetic Materials,* vol. 215, pp. 240-245, 2000.

[4] R. Kolano, K. Krykowski, A. Kolano-Burian, M. Polak, J. Szynowski, and P. Zackiewicz, "Amorphous soft magnetic materials for the stator of a novel high-speed PMBLDC motor," *IEEE transactions on magnetics,* vol. 49, pp. 1367-1371, 2013.

[5] Z. Wang, R. Masaki, S. Morinaga, Y. Enomoto, H. Itabashi, M. Ito, *et al.*, "Development of an axial gap motor with amorphous metal cores," *IEEE Transactions on Industry Applications,* vol. 47, pp. 1293-1299, 2011.

[6] Z. Wang, Y. Enomoto, M. Ito, R. Masaki, S. Morinaga, H. Itabashi, *et al.*, "Development of a permanent magnet motor utilizing amorphous wound cores," *IEEE Transactions on Magnetics,* vol. 46, pp. 570-573, 2010.

[7] G. S. Liew, N. Ertugrul, W. L. Soong, and J. Gayler, "Investigation of axial field permanent magnet motor utilising amorphous magnetic material," *Australian Journal of Electrical and Electronics Engineering,* vol. 3, pp. 111-120, 2007.

[8] J. A. Gayler, S. R. Kloeden, N. Ertugrul, and R. Hasegawa, "Method of constructing core with tapered pole pieces and low-loss electrical rotating machine with said core," ed: Google Patents, 2014.

[9] N. Ertugrul, R. Hasegawa, W. L. Soong, J. Gayler, S. Kloeden, and S. Kahourzade, "A novel tapered rotating electrical machine topology utilizing cut amorphous magnetic material," *IEEE Transactions on Magnetics,* vol. 51, pp. 1-6, 2015.

[10] K. Binns and A. Kurdali, "Permanent-magnet ac generators," in *Proceedings of the Institution of Electrical Engineers*, 1979, pp. 690-696.

[11] R. M. Saunders and R. H. Weakley, "Design of permanent-magnet alternators," *Transactions of the American Institute of Electrical Engineers,* vol. 70, pp. 1578-1581, 1951.

[12] D. Hanrahan and D. Toffolo, "Permanent Magnet Generators Part I-Theory," *Transactions of the American Institute of Electrical Engineers. Part III: Power Apparatus and Systems,* vol. 76, pp. 1098-1103, 1957.

[13] M. Rahman, A. Osheiba, T. Radwan, and E. Abdin, "Modelling and controller design of an isolated diesel engine permanent magnet synchronous generator," *IEEE transactions on energy conversion,* vol. 11, pp. 324-330, 1996.

[14] R. Niwas and B. Singh, "Solid-state controller for three-phase permanent magnet synchronous generator-based diesel generator set feeding single-phase loads," *IET Power Electronics,* vol. 8, pp. 1844-1852, 2015.

[15] B. Chalmers, "Performance of interior-type permanent-magnet alternator," *IEE Proceedings-Electric Power Applications,* vol. 141, pp. 186-190, 1994.

[16] K. Kurihara, T. Kubota, K. Saito, N. Kikuchi, and H. Iwamoto, "High-efficiency interior permanent-magnet synchronous generators with minimal voltage regulation for nano and pico hydro generation," in *Electrical Machines and Systems (ICEMS), 2012 15th International Conference on*, 2012, pp. 1-4.

[17] T. Chan, L. Lai, and L.-T. Yan, "Performance of a three-phase AC generator with inset NdFeB permanent-magnet rotor," *IEEE transactions on energy conversion,* vol. 19, pp. 88-94, 2004.

[18] T. Chan, L.-T. Yan, and L. L. Lai, "Permanent-magnet synchronous generator with inset rotor for autonomous power-system applications," *IEE Proceedings-Generation, Transmission and Distribution,* vol. 151, pp. 597-603, 2004.

[19] W. Wu, E. Spooner, and B. Chalmers, "Design of slotless TORUS generators with reduced voltage regulation," *IEE Proceedings-Electric Power Applications,* vol. 142, pp. 337-343, 1995.

[20] A. Darabi and C. Tindall, "Damper cages in genset alternators: FE simulation and measurement," *IEEE Transactions on Energy Conversion,* vol. 19, pp. 73-80, 2004.

[21] K. Kurihara, "Effects of damper bars on steady-state and transient performance of interior permanent-magnet synchronous generators," *IEEE Transactions on Industry Applications,* vol. 49, pp. 42-49, 2013.

[22] JMAG finite-element software. Available: https://www.jmag-international.com/. [Accessed: 29-Sep-2017].

[23] C.-Z. Liaw, W. L. Soong, B. A. Welchko, and N. Ertugrul, "Uncontrolled generation in interior permanent-magnet machines," *IEEE Transactions on Industry Applications,* vol. 41, pp. 945-954, 2005.

[24] P. E. Lillington, "Permanent magnet electrical machine," ed: Google Patents, 2016.

[25] S. Kahourzade, W. L. Soong, and P. Lillington, "Unbalanced loading behavior of the isolated interior permanent-magnet generator," in *Energy Conversion Congress and Exposition (ECCE), 2015 IEEE,* 2015, pp. 1826-1833.

[26] S. Kahourzade, W. L. Soong, and P. Lillington, "Single-Phase Loading Behavior of the Isolated 3ph Spoke Interior Permanent-Magnet Generator," *IEEE Transactions on Industry Applications,* 2016.

[27] R. Dutta, M. Rahman, and L. Chong, "Winding inductances of an interior permanent magnet (IPM) machine with fractional slot concentrated winding," *IEEE Transactions on Magnetics,* vol. 48, pp. 4842-4849, 2012.

[28] J. Pyrhonen, T. Jokinen, and V. Hrabovcova, *Design of rotating electrical machines*: John Wiley & Sons, 2009.

[29] A. T. De Almeida, F. J. Ferreira, and J. A. Fong, "Standards for efficiency of electric motors," *IEEE Industry Applications Magazine,* vol. 17, pp. 12-19, 2011.

[30] C. Jedryczka, R. M. Wojciechowski, and A. Demenko, "Influence of squirrel cage geometry on the synchronisation of the line start permanent magnet synchronous motor," *IET Science, Measurement & Technology,* vol. 9, pp. 197-203, 2014.

[31] N. M. Azari and M. Mirsalim, "Analytic modelling of a line-start permanent-magnet motor with slotted solid rotor," *IET Electric Power Applications,* vol. 8, pp. 278-285, 2014.

[32] E. Sarani and S. Vaez-Zadeh, "Line start permanent magnet motors with double-barrier configuration for magnet conservation and performance improvement," *IET Electric Power Applications,* vol. 11, pp. 1656-1663, 2017.

[33] A. Takahashi, S. Kikuchi, H. Mikami, K. Ide, and A. Binder, "Reluctance torque utility for line-starting permanent magnet motors," *IEEE Transactions on Energy Conversion,* vol. 28, pp. 805-814, 2013.

[34] P. Mellor, M. Al-Taee, and K. Binns, "Open loop stability characteristics of synchronous drive incorporating high field permanent magnet motor," in *IEE Proceedings B-Electric Power Applications,* 1991, pp. 175-184.

[35] Z. Abdelnour, H. Mildrum, and K. Strnat, "Properties of various sintered rare earth-cobalt permanent magnets between-60° and+ 200° C," *IEEE Transactions on Magnetics*, vol. 16, pp. 994-996, 1980.

[36] K.-D. Lee, W.-H. Kim, C.-S. Jin, and J. Lee, "Local demagnetisation analysis of a permanent magnet motor," *IET Electric Power Applications*, vol. 9, pp. 280-286, 2015.

[37] D. G. Dorrell, M.-F. Hsieh, and A. M. Knight, "Alternative rotor designs for high performance brushless permanent magnet machines for hybrid electric vehicles," *IEEE Transactions on Magnetics*, vol. 48, pp. 835-838, 2012.

[38] K.-C. Kim, S.-B. Lim, D.-H. Koo, and J. Lee, "The shape design of permanent magnet for permanent magnet synchronous motor considering partial demagnetization," *IEEE Transactions on magnetics*, vol. 42, pp. 3485-3487, 2006.

[39] K.-C. Kim, K. Kim, H. J. Kim, and J. Lee, "Demagnetization analysis of permanent magnets according to rotor types of interior permanent magnet synchronous motor," *IEEE Transactions on Magnetics*, vol. 45, pp. 2799-2802, 2009.

[40] W. L. Soong, S. Kahourzade, C.-Z. Liaw, and P. Lillington, "Interior PM generator for portable AC generator sets," *IEEE Transactions on Industry Applications*, vol. 52, pp. 1340-1349, 2016.

[41] S. Kahourzade, A. Mahmoudi, H. W. Ping, and M. N. Uddin, "A comprehensive review of axial-flux permanent-magnet machines," *Canadian Journal of Electrical and Computer Engineering*, vol. 37, pp. 19-33, 2014.

[42] Y. Guo, J. Zhu, H. Lu, Z. Lin, and Y. Li, "Core loss calculation for soft magnetic composite electrical machines," *IEEE Transactions on Magnetics*, vol. 48, pp. 3112-3115, 2012.

[43] C. Liu, J. Zhu, Y. Wang, Y. Guo, and G. Lei, "Comparison of claw-pole machines with different rotor structures," *IEEE Transactions on Magnetics*, vol. 51, pp. 1-4, 2015.

[44] Y. Enomoto, M. Ito, H. Koharagi, R. Masaki, S. Ohiwa, C. Ishihara, *et al.*, "Evaluation of experimental permanent-magnet brushless motor utilizing new magnetic material for stator core teeth," *IEEE transactions on magnetics*, vol. 41, pp. 4304-4308, 2005.

[45] Beijing OeMag International. Available: http://www.oemag.com/. [Accessed: 29-Sep-2017].

[46] G. S. Liew, W. L. Soong, N. Ertugrul, and J. Gayler, "Analysis and performance investigation of an axial-field PM motor utilising cut amorphous magnetic material," in *Universities Power Engineering Conference (AUPEC), 2010 20th Australasian*, 2010, pp. 1-6.

[47] L. Alberti, E. Fornasiero, N. Bianchi, and S. Bolognani, "Rotor losses measurements in an axial flux permanent magnet machine," *IEEE Transactions on Energy Conversion*, vol. 26, pp. 639-645, 2011.

[48] N. E. S. Kahourzade, and W. L. Soong, "Investigation of Emerging Magnetic Materials for Application in Axial-Flux PM Machines," *IEEE Energy Conversion Congress and Exposition (ECCE), Milwaukee, USA*, September 2016.

[49] T. Fan, Q. Li, and X. Wen, "Development of a high power density motor made of amorphous alloy cores," *IEEE Transactions on Industrial Electronics*, vol. 61, pp. 4510-4518, 2014.

[50] O. Veselovskii, A. Yarunov, S. Shvets, and S. Sternina, "The action of an asynchronous conical motor used as a rotary-percussive mechanism," *Soviet Mining*, vol. 4, pp. 197-199, 1968.
[51] J. P. Petro and K. G. Wasson, "Rotor-stator structure for electrodynamic machines," ed: Google Patents, 2007.
[52] E. A. Fisher and E. Richter, "Conical rotor for switched reluctance machine," ed: Google Patents, 1993.
[53] A. G. Flogvall, "Motor arrangement comprising at least three co-planar conical motors," ed: Google Patents, 1986.
[54] J. F. Gieras and M. Wing, *Permanent magnet motor technology*: Marcel Dekker New York, NY, USA, 2002.
[55] H. Vansompel, P. Sergeant, L. Dupré, and A. Van den Bossche, "Axial-flux PM machines with variable air gap," *IEEE Transactions on Industrial Electronics*, vol. 61, pp. 730-737, 2014.
[56] E. Fornasiero, N. Bianchi, and S. Bolognani, "Slot harmonic impact on rotor losses in fractional-slot permanent-magnet machines," *IEEE Transactions on industrial electronics*, vol. 59, pp. 2557-2564, 2012.
[57] T. Sakaue and K. Akatsu, "Stator iron loss measurement method in permanent magnet synchronous motor to remove the mechanical loss effect," in *Electrical Machines and Systems (ICEMS), 2014 17th International Conference on*, 2014, pp. 3131-3135.
[58] K. Yamazaki, T. Fukuoka, K. Akatsu, N. Nakao, and A. Ruderman, "Investigation of locked rotor test for estimation of magnet PWM carrier eddy current loss in synchronous machines," *IEEE Transactions on Magnetics*, vol. 48, pp. 3327-3330, 2012.